# The Central 300 pc of the Galaxy Probed by Infrared Spectra of H$_3^+$ and CO. I. Predominance of Warm and Diffuse Gas and High H$_2$ Ionization Rate

Takeshi Oka[1], T. R. Geballe[2], Miwa Goto[3], Tomonori Usuda[4], Benjamin, J. McCall[5,6], and Nick Indriolo[4]

[1] Department of Astronomy and Astrophysics and Department of Chemistry, The Enrico Fermi Institute, University of Chicago, Chicago, IL 60637, USA
t-oka@uchicago.edu
[2] Gemini Observatory, Hilo, HI 96720, USA
[3] Universitäts-Sternwarte München, D-81679, Munich, Germany
[4] National Astronomical Observatory of Japan, Tokyo, Japan
[5] Department of Chemistry, Department of Physics, and Department of Astronomy, University of Illinois, Urbana, IL 61801, USA

## Abstract

The molecular gas in the central molecular zone (CMZ) of the Galaxy has been studied using infrared absorption spectra of H$_3^+$ lines at 3.5–4.0 $\mu$m and CO lines near 2.34 $\mu$m. In addition to the previously reported spectra of these lines toward eight stars located within 30 pc of Sgr A$^*$, there are now spectra toward ∼30 bright stars located from 140 pc west to 120 pc east of Sgr A$^*$. The spectra show the presence of warm ($T \sim 200$ K) and diffuse ($n < 100$ cm$^{-3}$) gas with $N(\mathrm{H}_3^+) \sim 3 \times 10^{15}$ cm$^{-2}$ on the majority of sight lines. Instead of our previous analysis, in which only electrons from photoionization of carbon atoms were considered, we have developed a simple model calculation in which the cosmic-ray ionization of H$_2$ and H is also taken into account. We conclude the following: (1) Warm and diffuse gas dominates the volume of the CMZ. The volume filling factor of dense gas must be much less than 0.1, and the CMZ is not as opaque as previously considered. The X-ray-emitting ultrahot $10^8$ K plasma, which some thought to dominate the CMZ, does not exist over extended regions. (2) The cosmic-ray ionization rate is $\zeta \sim 2 \times 10^{-14}$ s$^{-1}$, higher than in Galactic dense clouds and diffuse clouds by factors of ∼1000 and ∼100, respectively. If the equipartition law stands, this suggests a pervading magnetic field on the order of ∼100 $\mu$G.

*Key words:* astrochemistry – cosmic rays – Galaxy: center – infrared: stars – ISM: lines and bands – ISM: molecules

## 1. Introduction

The Galactic center (GC) is rich in extraordinary objects such as the central supermassive black hole, Sgr A$^*$, three massive star clusters (the Central, the Quintuplet, and the Arches), gigantic nonthermal radio filaments, giant molecular clouds, giant H II regions (such as Sgr A, B, C, D, E), and others. As viewed from Earth, the GC is a strong emitter of radio, far-infrared, infrared, X-rays, and $\gamma$-rays, as was noted by the early broadband observations in those wavelength regions (Reber 1944; Piddington & Minnett 1951, in the radio continuum; Hildebrand et al. 1978, in the submillimeter; Hoffmann & Frederick 1969, in the far-infrared; Becklin & Neugebauer 1968, 1969; Low et al. 1969, in the mid- and near-infrared; Bowyer et al. 1965; Kellogg et al. 1971, in X-rays; and Clark et al. 1968, in $\gamma$-rays). Both line emission and line absorption also are prevalent in the GC, with pioneering detections made by Rougoor & Oort (1960) of the 21 cm H I line emission, Bolton et al. (1964b) and others that same year of OH absorption, Cheung et al. (1968) and Penzias et al. (1971) of NH$_3$ and CO emission, respectively, Aitken et al. (1974) of atomic fine-structure line emission, and Gatley et al. (1984) of H$_2$ line emission.

### 1.1. The Central Molecular Zone (CMZ): Previous Observations

The central region of the GC, with a radius of ∼150 pc (we use a GC distance of 8 kpc) and a thickness of a few tens of parsecs, was designated the CMZ by Morris & Serabyn (1996) because of its high concentration of molecules. This region,

which constitutes a mere ∼$10^{-5}$ of the volume of the Galaxy, was estimated by them to contain ∼10% of all Galactic molecules. The high abundance of many molecular species in the CMZ has allowed the study of the physics, chemistry, and morphology of molecular gas in the CMZ extensively by radio spectroscopy, particularly via the centimeter absorption spectrum of OH (e.g., Robinson & McGee 1970; Cohen & Few 1976; Boyce & Cohen 1994) and H$_2$CO (e.g., Scoville et al. 1972; Whiteoak & Gardener 1979; Cohen & Few 1981; Zylka et al. 1992; Ao et al. 2013; Ginsburg et al. 2016). The inversion lines of NH$_3$ (e.g., Güsten et al. 1981; Morris et al. 1983; Hüttemeister et al. 1993; Nagayama et al. 2007; Mills & Morris 2013; Krieger et al. 2017) are unique in that their frequencies are nearly independent of rotational quantum numbers $J$ and $K$; in addition, $J = K$ levels are metastable, thus allowing observations of very high rotational levels (see Appendix C). Millimeter-wave line emission from HCN (e.g., Fukui et al. 1977; Jackson et al. 1996; Lee 1996), CS (e.g., Bally et al. 1988; Tsuboi et al. 1999; Lang et al. 2002), and SiO (e.g., Hüttemeister et al. 1998; Riquelme et al. 2010) molecules with large dipole moments (2.985, 1.958, and 3.098 D, respectively) have fast spontaneous emission and thus high critical densities and have been useful for observing dense regions ($n > 10^4$ cm$^{-3}$).

Millimeter emission lines of $^{12}$C$^{16}$O and its isotopic species $^{13}$C$^{16}$O and $^{12}$C$^{18}$O (e.g., Bania 1977; Liszt & Burton 1978; Heiligman 1987; Bally et al. 1988; Sofue 1995; Oka et al. 1998b; Sawada et al. 2001; Martin et al. 2004) have provided by far the most detailed and extensive information on the molecular content of the CMZ. The high abundance of CO, second only to H$_2$, makes CO a general probe of molecular regions having a wide range of temperatures, number densities,

and column densities. At shorter wavelengths, far- to mid-infrared rotational emission spectral lines of $H_2$ have provided information on warm molecular gas (Rodríguez-Fernández et al. 2001) in the CMZ. The near-infrared vibrational emission spectrum of this molecule gives information on UV excitation there (Pak et al. 1996).

In addition to the above molecules, which contain at most two heavy ($M > 10$ u) atoms, many molecules and molecular ions with more than two heavy atoms have been detected in the GC (Requena-Torres et al. 2006, 2008), and some have been used for mapping of the CMZ (e.g., Jones et al. 2012, 2013). The highest mass molecule detected in the CMZ was $HC_5N$ (Avery et al. 1976; Armijos-Abendaño et al. 2015), until $HC_7N$ was observed more than 40 yr later (Zeng et al. 2018).

### 1.2. Filling Factor of Dense Molecular Gas in the CMZ

The majority of the radio and millimeter molecular line emission observed in the CMZ has been interpreted as arising in dense ($n \geqslant 3 \times 10^3 \, \mathrm{cm}^{-3}$) gas (e.g., Mills et al. 2018). The ubiquity of this emission has led to a high estimated volume filling factor, $f \geqslant 0.1$, for such dense molecular gas in the CMZ (Morris & Serabyn 1996). For an average value $n = 10^4 \, \mathrm{cm}^{-3}$, the lower limit of that filling factor corresponds to an average $H_2$ column density of $N(H_2) \sim 5 \times 10^{23} \, \mathrm{cm}^{-2}$ over the radial distance of 150 pc and an average visual extinction of $A_V \geqslant 500$ in the CMZ's dense gas using the standard ratio of dust to gas (Bohlin et al. 1978; Predehl & Schmitt 1995). Such high average column density and associated extinction appear to conflict with values derived from observations of the thermal emission from dust at submillimeter and millimeter wavelengths by Bally et al. (2010). From their data (see, e.g., their Table 3) we estimate that average values of $N(H_2)$ and $A_V$ in the CMZ are roughly 30 times less.

The estimate also appears to conflict with measurements of visual extinction toward many objects located within 40 pc of the very center, derived from infrared observations, which is well known to be $\sim 30$ mag (e.g., Cotera et al. 2000), also more than an order of magnitude less than the Morris & Serabyn lower limit. Larger-area infrared studies, covering the entire CMZ (Schultheis et al. 2009), give fairly similar values, although somewhat higher values in some regions. In addition, it has been estimated that one-third of the extinction to objects close to Sgr A$^*$ arises in molecular gas in foreground spiral arms (Whittet et al. 1997).

Brightness-limited infrared studies, such as that of Cotera et al. (2000) and the study described here, will tend to select objects in front of densest and highest-extinction CMZ clouds. Nevertheless, it seems clear from the above near-infrared and far-infrared–millimeter extinction results, and from the spectra that we present and discuss in this paper, that the previously estimated $f \geqslant 0.1$ for the volume filling factor of $n \geqslant 10^4 \, \mathrm{cm}^{-3}$ gas in the CMZ is far too high.

It has been pointed out by the referee that lower filling factors than this have been implicit in some previous papers on dense gas (e.g., Launhardt et al. 2002; Molinari et al. 2011; Sormani et al. 2018; Kruijssen et al. 2019).

### 1.3. Previous Observations of Diffuse Molecular Gas in the CMZ

Although a large majority of papers reporting radio emission from molecules in the CMZ deduce high $H_2$ number densities,

$n(H_2) \geqslant 3 \times 10^3 \, \mathrm{cm}^{-3}$, there are a few exceptions in which molecular emission lines at radio and millimeter wavelengths were interpreted to be from clouds of lower density than dense clouds. Oka et al. (1998a; Tomoharu Oka of Keio University, not to be confused with the first author of the present paper) concluded that "the total CO emission from the GC is dominated by the emission from low-density [$n(H_2) \approx 10^{2.5} \, \mathrm{cm}^{-3}$] gas." Independently, Dahmen et al. (1998) proposed a somewhat higher average density ($n(H_2) \approx 10^3 \, \mathrm{cm}^{-3}$) based on observations of $C^{18}O$ line emission. They also report $\approx 10^2 \, \mathrm{cm}^{-3}$ as a minor component. In a noteworthy but little referenced paper, Magnani et al. (2006) observed 3335 MHz CH emission, which traces low-density molecular gas, in a $30' \times 30'$ region and found broad-line profiles that are quite different from those of CO emission lines, which arise predominantly in dense clouds.

Although not mentioned explicitly in their publications, the absorption spectra of OH (Bolton et al. 1964a; Goldstein et al. 1964; Robinson & McGee 1970) and $H_2CO$ (Scoville et al. 1972) in the CMZ are likely to arise in low-density gas, some of which may be the gas with $n < 100 \, \mathrm{cm}^{-3}$ most effectively probed by $H_3^+$ that we have observed. Recently *Herschel* observations of rotational absorption spectra of molecular ions such as $OH^+$ and $H_2O^+$ (e.g., Goicoechea et al. 2013; Indriolo et al. 2015), $CH^+$ and $SH^+$ (Godard et al. 2012), and $ArH^+$ (Schilke et al. 2014) also indicate the presence of low-density regions. These molecular ions are rapidly destroyed by $H_2$ at the Langevin rate and thus can exist only in diffuse regions with low fractions of molecular hydrogen $f(H_2)$. So far, they have been observed only toward Sgr A and Sgr B, which contain dense giant molecular cloud complexes, but these molecular ions must reside in diffuse clouds in the outskirts of the complexes. Even the CMZ's HF and $H_2O$, which mainly exist in dense clouds, were interpreted to reside partly in the low-density clouds by Sonnentrucker et al. (2013), who conclude that a "very dilute phase seems pervasive around the Galactic center."

### 1.4. Temperatures

Kinetic temperatures in the CMZ have been found to be significantly higher than the few tens of kelvins typically found in the Galactic disk's interstellar medium. Early far-infrared studies found dust temperatures, $T_d$, less than 30 K (Hildebrand et al. 1978; Odenwald & Favio 1984) and more definitively later (e.g., $T_d = 15$–22 K by Lis et al. 2001). However, many studies of molecular line emission have reported kinetic temperatures, $T_k$, of 25–80 K, indicating dynamical heating of the gas (Ao et al. 2013; Ginsburg et al. 2016; Krieger et al. 2017). Observations of rotational emission lines of $H_2$ demonstrate that gas with $T_k = 150$ K is widespread (Rodríguez-Fernández et al. 2001). Although $H_2$ coexists with CO at high densities ($10^{3.5-4.0} \, \mathrm{cm}^{-3}$), most of the $H_2$ line emission may well originate in surrounding lower-density regions. Hot $NH_3$ is also observed in the CMZ, implying gas temperatures of a few hundred kelvins (Mauersberger et al. 1986). This is discussed in Appendix C.

### 1.5. A Brief History of Interstellar $H_3^+$

Trihydrium, a term recommended by J. K. G. Watson (2019, private communication) and used here for the first time, otherwise known as $H_3^+$, in which a proton is attached to $H_2$ in an equilateral triangular configuration, was discovered by

Thomson (1911). In $H_2$-dominated interstellar gases this simplest polyatomic molecule is the most abundant molecular ion. Martin et al. (1961) first proposed detecting interstellar $H_3^+$. Observing interstellar $H_3^+$ attained great importance when Herbst & Klemperer (1973) and Watson (1973) deduced that most interstellar molecules are produced by ion-neutral reactions and that $H_3^+$ plays the central role as the universal proton donor (acid) to initiate chains of such reactions. The infrared spectrum of the fundamental $\nu_2$ band, with band origin at $3.97\,\mu m$, was observed in the laboratory by Oka (1980). Following unsuccessful searches (Oka 1981; Geballe & Oka 1989), detections of absorption lines of interstellar $H_3^+$ in two dense interstellar clouds were made by Geballe & Oka (1996). The $H_3^+$ column densities observed in many dense clouds by them and others (McCall et al. 1999; Kulesa 2003; Brittain et al. 2004; Gibb et al. 2010) are approximately as expected from the theory. Readers are referred to a recent review (Oka 2013) for more details of the history, astronomy, physics, and chemistry of this fundamental molecular ion.

Once detected, $H_3^+$ has been observed in numerous interstellar molecular environments. Two big surprises were found soon after its discovery. First, absorption lines of $H_3^+$ with similar strengths to those in dense clouds were discovered in diffuse clouds (McCall et al. 1998a; Geballe et al. 1999; McCall et al. 2002), implying that $H_3^+$ column densities in diffuse clouds are comparable to those in dense clouds, despite the much higher abundance in diffuse clouds of $H_3^+$-destroying free electrons created by the ionization of carbon atoms. Extinctions through diffuse clouds are typically an order of magnitude less than through dense clouds, indicating that the fraction of $H_3^+$, $X(H_3^+) \equiv n(H_3^+)/n_H$, is $\sim 10$ times higher in diffuse clouds than in dense clouds. Because of this higher abundance, $H_3^+$ has emerged as a valuable probe of physical conditions in diffuse clouds. Further studies have led to the important conclusion that in the Galactic disk, on average, the rate of cosmic-ray ionization of $H_2$ in Galactic diffuse clouds is 10 times higher than in dense clouds (McCall et al. 2003; Indriolo et al. 2007; Indriolo & McCall 2012), contradicting the previous notion that the rate is more or less uniform in the Galaxy.

Second, $H_3^+$ column densities more than 10 times greater than the highest ones observed in the Galactic disk were found toward bright, dust-embedded infrared stars in the CMZ, GCS 3-2 in the Quintuplet Cluster, and GCIRS 3 in the Central Cluster (Geballe et al. 1999) and subsequently toward many other stars in the CMZ, as discussed below. This finding initiated our long-term systematic study of the CMZ using $H_3^+$ as a probe, which continues to this day. $H_3^+$ has been observed also in two extragalactic objects: the ultraluminous galaxy IRAS 08572+3915NW (Geballe et al. 2006) and type II Seyfert galaxy NGC 1068 (Geballe et al. 2015).

### 1.6. $H_3^+$ in the CMZ: Warm and Diffuse Gas

The kinetic temperatures of both dense and diffuse molecular clouds in the Galactic disk are typically a few tens of kelvins. Toward stars in the Central and Quintuplet Clusters, however, large amounts of $H_3^+$ in the metastable $(J, K) = (3, 3)$ level, 361 K above the lowest $(1, 1)$ level (see Figure 1), have been found via detection of absorption in the $R(3, 3)^l$ line at $3.53\,\mu m$ (Goto et al. 2002). The relative populations in those levels imply that $H_3^+$ in the CMZ exists in gas at temperatures of a few hundred kelvins (Oka et al. 2005). A significant population of
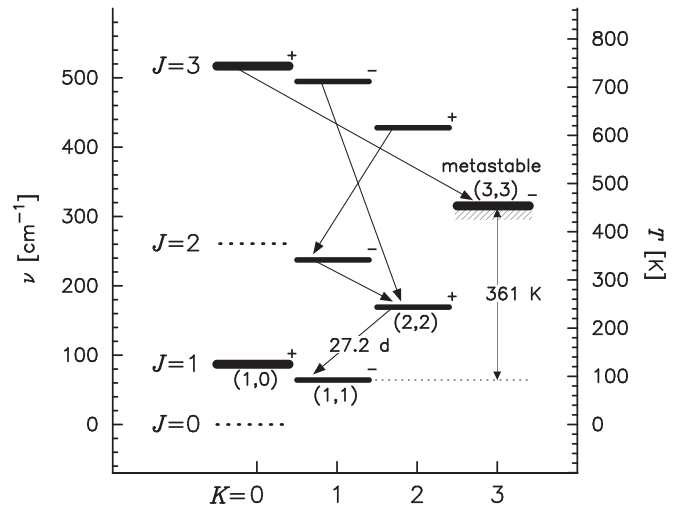


**Figure 1.** Lower rotational levels in the ground vibrational state of $H_3^+$, composed of ortho ($K = 3n$; thick line) and para ($K = 3n \pm 1$; thin line) nuclear spin states. The plus and minus signs indicate the parity $= (-1)^K$. The (0, 0) and (2, 0) levels are forbidden owing to nuclear spin statistics (as for the symmetric inversion levels of $NH_3$). Downward-pointing arrows indicate spontaneous emission due to SBS. The energy gap between the lowest level and the (3, 3) level and the lifetime of the (2, 2) level for spontaneous emission are shown. In the warm diffuse molecular gas of the CMZ, because of rapid spontaneous emission, only three levels (1, 1), (1, 0), and (3, 3) are significantly populated; in denser warm molecular gas the (2, 2) level is also significantly populated.

$H_3^+$ in the (3, 3) level has become the fingerprint of diffuse gas in the CMZ. Attempts to detect $H_3^+$ in the lower-lying (2, 2) level, which is only 150 K above the (1, 1) level, in the CMZ via the $R(2, 2)^l$ line at $3.62\,\mu m$ have largely failed (e.g., Goto et al. 2002; Oka et al. 2005). The extreme population inversion of the (3, 3) and (2, 2) levels is due to spontaneous emission from (2, 2) to (1, 1), a consequence of the spontaneous breakdown of symmetry (SBS; see Appendix C). A lifetime of 27 days of the (2, 2) level against this emission has been determined from high-quality ab initio theory (Neale et al. 1996) and corresponds to a critical density of $200\,cm^{-3}$ assuming the Langevin rate constant of $2 \times 10^{-9}\,cm^3\,s^{-1}$ for $H_3^+$–$H_2$ collisions. The decisive population inversion between these levels is a clear demonstration that the density of the warm gas is much less than $200\,cm^{-3}$. The rotational levels of $H_3^+$, shown in Figure 1, are ideally arranged to study this warm, low-density environment.

A more quantitative treatment of thermalization, in which many SBS emissions are treated accurately and collisional transitions approximately, based only on the principle of detailed balance (Oka & Epp 2004), has led to the finding of two-dimensional relationships between $T_k$ and $n(H_2)$ and between the column density ratios $N(3, 3)/N(1, 1)$ and $N(3, 3)/N(2, 2)$. These relations and their inverses, together with the observed $H_3^+$ column densities, allowed $H_3^+$ in the CMZ to be used as a thermometer and densitometer for GCS 3-2 (likely the brightest infrared star in the CMZ, based on its infrared magnitudes and colors) and for seven other stars located from Sgr A$^*$ to 30 pc east of it (Oka et al. 2005; Goto et al. 2008). Unlike the physical collisions between $NH_3$ and $H_2$, in which the ortho/para spin states conserve and the $\Delta k = \pm 3$ rule holds (Oka 1973), collisions between $H_3^+$ and $H_2$ are chemical collisions in which the protons are exchanged between $H_3^+$ and $H_2$, spin states may change, and thus the $\Delta k$ rule is violated

(Appendix C). The rotational distribution of $H_3^+$ is subthermal, and our attempts to detect higher metastable levels (4, 4), (5, 5), and (6, 6) have not been successful.

In this paper, we focus our analysis and discussion on $H_3^+$ in diffuse molecular CMZ gas, which, as we describe in subsequent sections, appears to exist in similar conditions throughout the CMZ and thus can be treated generally. In contrast, the contributions to the spectra on these sight lines by $H_3^+$ in dense clouds in the CMZ differ for each sight line, reflecting local conditions in those clouds, and are better dealt with individually. Observations and analyses of $H_3^+$ in dense clouds on several sight lines toward stars in the CMZ have been previously published (Goto et al. 2011, 2013, 2014).

### 1.7. Production and Destruction of $H_3^+$ in Diffuse Gas

In interstellar molecular gas $H_3^+$ is mainly produced by cosmic-ray ionization of $H_2$ to $H_2^+$ at a slow rate $\zeta$ followed by the very rapid Langevin reaction,

$$H_2 + H_2^+ \rightarrow H_3^+ + H, \tag{1}$$
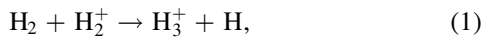
in which a proton hops from $H_2^+$ to $H_2$ (Section 2.2.1 of Oka 2013). In diffuse clouds, $H_3^+$ is mainly destroyed by dissociative recombination with electrons,

$$H_3^+ + e^- \rightarrow H + H + H, \quad H_2 + H, \tag{2}$$
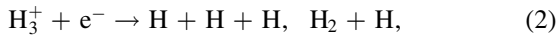
whose rate constant is $\sim$100 times larger than the Langevin rate constant (Section 2.3.3 of Oka 2013).

For $H_3^+$ in the diffuse molecular gas of the CMZ this simple chemistry leads to a linear relation between the product of $\zeta$ and column length, $L$, of the absorbing diffuse gas and the total $H_3^+$ column density $N(H_3^+)$,

$$\zeta L = 2 k_e N(H_3^+)(n_C/n_H)_{SV} R/f(H_2), \tag{3}$$

on the assumption that all electrons are from photoionization of C atoms (Oka et al. 2005). In the above relation $k_e$ is the rate constant for dissociative recombination (McCall et al. 2004), $(n_C/n_H)_{SV}$ is the carbon-to-hydrogen ratio in the solar vicinity (Sofia et al. 2004), $R$ is the increase of metallicity from the solar vicinity to the GC, and $f(H_2) = 2n(H_2)/[n(H) + 2n(H_2)]$ is the fraction of molecular hydrogen. The observed large $H_3^+$ column densities in the CMZ's warm and diffuse gas, $N(H_3^+) \sim 3 \times 10^{15}$ cm$^{-2}$ (Oka et al. 2005; Goto et al. 2008), yield high values of $\zeta L$ and, given reasonable constraints on $L$, likely cosmic-ray ionization rates of $H_2$ on the order of $\zeta \sim 3 \times 10^{-15}$ s$^{-1}$, an order of magnitude higher than in Galactic diffuse clouds and two orders of magnitude higher than in dense clouds. The above equation and resulting estimate for $\zeta$ (which was obtained on the assumptions that $f(H_2) \sim 1$ and $R \sim 3$) are modified in the present paper in a major way as discussed below and in Section 5.2.

Recently, Le Petit et al. (2016) in the Laboratoire d'Études du Rayonnement et de la Matière en Astrophysique et Atmosphères (LERMA) Meudon analyzed the $H_3^+$ column densities in the CMZ observed by us (Oka et al. 2005; Goto et al. 2008, 2011). Hereafter we refer to their analysis as the Meudon analysis. Instead of the simple chemistry based only on Equations (1) and (2), they used the Meudon photodissociation region (PDR) code (Le Petit et al. 2006), in which a great many species (165) and chemical reactions (2850) are simultaneously considered. They also used *Herschel* observations of HF, OH$^+$, $H_2O^+$, and $H_3O^+$

toward Sgr B2 to constrain the physical and chemical parameters of the CMZ. They extended the calculations to high values of $\zeta$ where the linear relation between $\zeta$ and $N(H_3^+)$ of Equation (3) no longer holds and obtained values for $\zeta$ of $(1–11) \times 10^{-14}$ s$^{-1}$, considerably larger than those derived by Oka et al. (2005) and Goto et al. (2008). They also used a more detailed calculation of thermalization by Gómez-Carrasco et al. (2012), which is based on the statistical theory of Park & Light (2007a), to determine temperature and density. The Meudon analysis is discussed in Sections 5.1.2 and 5.2.6. For a review of variations in the derived values of $\zeta$ over the years, see Oka (2019).

### 1.8. The $v = 2 \neg 0$ First-overtone Infrared Spectrum of CO

Unlike $H_3^+$, which is abundant in both diffuse and dense clouds, CO abundances and column densities in diffuse clouds are much lower than in dense clouds, due to diffuse clouds being permeated by CO—dissociating ultraviolet photons. Because of this difference, observations of $H_3^+$ combined with properly designed observations of CO can discriminate between $H_3^+$ in dense gas and diffuse gas. On sight lines to the CMZ, discrimination is made easier by the diffuse and dense gas having different radial velocities and line widths. In particular, the molecular clouds in the three foreground spiral arms produce narrow absorption features at well-known radial velocities, which usually can be easily separated from the absorption by the CMZ's diffuse gas.

The rotationally resolved infrared spectrum of $^{12}$CO in the CMZ was initially observed in the $v = 1 \leftarrow 0$ fundamental band near 4.7 $\mu$m (Geballe et al. 1989) and later by others (see Moultaka et al. 2019 and references therein). Because lines of this band that originate in the most populated levels are heavily saturated, in our studies we have used lines of the $v = 2 \leftarrow 0$ first-overtone band near 2.34 $\mu$m. The transition dipole moment of this band, $\langle 2|\mu|0 \rangle = (0.006518 \pm 0.000028)$ D (Zou & Varanasi 2002), is 16 times lower than that of the fundamental band, $\langle 1|\mu|0 \rangle = 0.1055$ D, that is, its absorption is 262 times weaker. Because of the very low abundance of CO in diffuse clouds, first-overtone absorption lines there are undetectable or very weak. However, in dense clouds, where CO has a high abundance, the overtone CO lines are much stronger and easily detectable. They are seldom saturated, however, allowing one to determine reliable CO column densities. Like the lines of the fundamental vibration–rotation band, the low-lying transitions of the pure rotational spectrum of $^{12}$CO (permanent dipole moment $\mu = 0.1098$ D; Muenter 1975) at millimeter and submillimeter wavelengths are highly saturated.

### 1.9. Observable Sight Lines in the CMZ and Outline of the Paper

Until 2008, spectra of $H_3^+$ in the CMZ were confined to sight lines toward previously known bright dust-embedded stars in the Central Cluster of massive stars surrounding Sgr A* (Becklin & Neugebauer 1975), similar stars in the Quintuplet Cluster (Nagata et al. 1990; Okuda et al. 1990), and the Nagata, Hyland, & Straw (NHS) stars reported by Nagata et al. (1993). Stars in the latter two groups are located no more than 30 pc to the east of Sgr A*, and thus collectively they and the Central Cluster sight lines sample only a small fraction of the longitudinal extent of the CMZ. In 2008, we began to search for bright stars suitable for high-resolution spectroscopy of the relatively weak lines of $H_3^+$, across the entire $r \sim 150$ pc CMZ. This search is outlined in Section 2.2. A paper containing

spectra of $H_3^+$ and CO toward two such stars in the Sgr B and Sgr E complexes (Geballe & Oka 2010) and a subsequent paper (Goto et al. 2011) both reported the discovery of $H_3^+$ in warm diffuse molecular gas and dense molecular gas on these sight lines. The presence of similar gas far from the warm diffuse gas seen toward stars near the center of the CMZ suggested that the newly found gas is widespread in the CMZ. However, observations on additional sight lines that are both more widely and more uniformly spread across the CMZ are required to more stringently test this possibility. This paper reports and discusses such observations.

We describe the observational considerations and the observations themselves in Section 2. The spectra are presented in Section 3. The basic interpretation of the spectra and determination of temperatures and column densities of the diffuse and dense CMZ gas are given in Section 4. In Section 5 the new analysis method is presented and compared with the Meudon analysis, and values of the cosmic-ray ionization rate, the column length of warm diffuse gas, and particle densities are estimated. The implications of these results are discussed in Section 6, and a summary and main conclusions are presented in Section 7. Readers may understand the essence of this paper by reading the last section alone. Some details of our analysis are discussed separately in appendices to this paper. More detailed information on and discussion of the morphology and dynamics of the gas obtained from velocity profiles of the lines will be given in a separate paper as Part II of this series.

## 2. Observation

### 2.1. Spectral Lines and Observing Sites

The $R$- and $Q$-branch lines of the fundamental $\nu_2$ vibration–rotation band of $H_3^+$ that are of particular astrophysical interest in studying the CMZ occur in the $L$ atmospheric window from 3.45 to 3.95 $\mu$m, a region relatively free from atmospheric interference (see Figure 1 of McCall et al. 1998b). That wavelength range is well above the 2.73 $\mu$m $\nu_1$ and 2.66 $\mu$m $\nu_3$ bands of $H_2O$ and well below that molecule's 6.27 $\mu$m $\nu_2$ band. The principal interference is caused by $P$-branch lines of the 3.31 $\mu$m $\nu_3$ band of $CH_4$ and by the 3.17 $\mu$m $2\nu_2$ band of $H_2O$. Particularly annoying is the strong $5_{05} \leftarrow 6_{34}$ transition of the latter band, whose frequency, 2830.008 $cm^{-1}$, is only 0.083 $cm^{-1}$ higher than that of the $R(3, 3)^l$ line of $H_3^+$. Observations of that $H_3^+$ line are thus very sensitive to variations in the column density of water vapor above the observatory, and it is generally more difficult to obtain reliable line profiles of it at lower-altitude sites, such as Cerro Pachon (2715 m) and Cerro Paranal (2635 m), than on Maunakea (4200 m).

Relevant $H_3^+$ transitions with frequencies and (vacuum) wavelengths taken from Oka (2013) and squares of dipole moments $|\mu|^2$ are listed in Table 1. From the observed equivalent widths $W_\lambda$, the $H_3^+$ column densities in the lower levels can be calculated by $N(H_3^+)_{level} = (3hc)/(8\pi^3\lambda)\,W_\lambda/|\mu|^2$. Because of the rapid SBS spontaneous emissions and the efficient chemical collisions with $H_2$, only four levels (1, 1), (1, 0), (2, 2), and (3, 3) in the ground vibrational state are observably populated in the CMZ. Therefore, the $\nu_2$ transitions that we have primarily observed are $R(1, 1)^l$, $R(3, 3)^l$, the close doublet of $R(1, 0)$ and $R(1, 1)^u$ (velocity separation = 35 km s$^{-1}$), and $R(2, 2)^l$. The $R(1, 1)^l$ and $R(3, 3)^l$ lines have been detected toward all stars in the CMZ, while $R(2, 2)^l$ has been detected only toward a few stars that lie behind or inside dense clouds within the CMZ. The

**Table 1**
$H_3^+$ and CO Transitions

| Transitions | $\nu$ (cm$^{-1}$) | $\lambda$ ($\mu$m) | $|\mu|^2$ (D$^2$) |
|---|---|---|---|
| | | $H_3^+$ | |
| $Q(1, 0)$ | 2529.724 | 3.95300 | 0.0254 |
| $Q(1, 1)$ | 2545.420 | 3.92862 | 0.0128 |
| *$R(1, 1)^l$ | 2691.443 | 3.71548 | 0.0141 |
| *$R(1, 0)$ | 2725.898 | 3.66852 | 0.0259 |
| *$R(1, 1)^u$ | 2726.220 | 3.66808 | 0.0158 |
| *$R(2, 2)^l$ | 2762.070 | 3.62047 | 0.0177 |
| *$R(3, 3)^l$ | 2829.925 | 3.53366 | 0.0191 |
| *$R(4, 4)^l$ | 2894.488 | 3.45484 | 0.0197 |
| | | CO | |
| $R(0)$ | 4263.837 | 2.34531 | 0.0000425 |
| $R(1)$ | 4267.542 | 2.34327 | 0.0000283 |
| $R(2)$ | 4271.177 | 2.34128 | 0.0000255 |
| $R(3)$ | 4274.741 | 2.33932 | 0.0000243 |
| $R(4)$ | 4278.234 | 2.33741 | 0.0000236 |
| $R(5)$ | 4281.657 | 2.33554 | 0.0000232 |

**Note.** Wavenumbers $\nu$, vacuum wavelengths $\lambda$, and transition strengths $|\mu|^2$ of the $H_3^+$ $\nu_2$ fundamental band and CO first-overtone band $v = 2 \rightarrow 0$ used in this paper. Excerpts from Table 2 of Oka (2013).

notation $R(1, 1)^l$ signifies the transition ($v_2 = 1$, $l = 1$ lower, $J' = 2$, $K' = 2$) $\leftarrow$ ($v_2 = l = 0$, $J = 1$, $K = 1$). See Lindsay & McCall (2001) for more details on the nomenclature. Other transitions in Table 1, such as $Q(1, 0)$ and $Q(1, 1)$, have been observed toward a limited number of stars.

CO has been observed mostly through its $K$-band $v = 2 \leftarrow 0$ vibration–rotation band. The relevant parameters for the observed lines are given in Table 1. The low-$J$ lines in this band are sharp toward the CMZ and are only moderately affected by atmospheric absorption. For some stars that are too faint in the $K$ band ($K > 11.5$ mag) for sufficiently accurate high-resolution absorption spectroscopy, the fundamental bands of $^{13}CO$ and $C^{18}O$ have been observed instead.

### 2.2. Selection of Background Infrared Sources

High-resolution infrared absorption spectroscopy of $H_3^+$ and CO at high signal-to-noise ratio (S/N) can be conducted only toward background objects with bright 2–5 $\mu$m infrared continua; such objects are almost entirely stars. Bright stars with complex photospheric spectra (e.g., Ridgway et al. 1984) cannot be used, however, as their spectra are superimposed on the lines arising in the interstellar gas, making analysis of the interstellar lines difficult or impossible. This eliminates as probes most infrared-bright stars, which are red giants. Consequently, only luminous hot stars whose spectra contain only lines of a few elements (e.g., hydrogen, helium, carbon) and luminous stars that are deeply embedded in warm opaque dust shells are suitable background sources. This is a serious limitation, when compared to observations of CO radio wavelength emission, which can be conducted toward any molecular cloud. However, absorption spectroscopy has the advantages that (a) the location of the absorbing gas is known to be in front of the continuum source, and hence it is clear whether the absorbing gas is moving toward or away from the star; (b) the optical depths of lines of the $H_3^+$ fundamental and CO first-overtone bands are almost always low ($\tau < 0.15$), and thus column densities are reliably determined; (c) the beam size
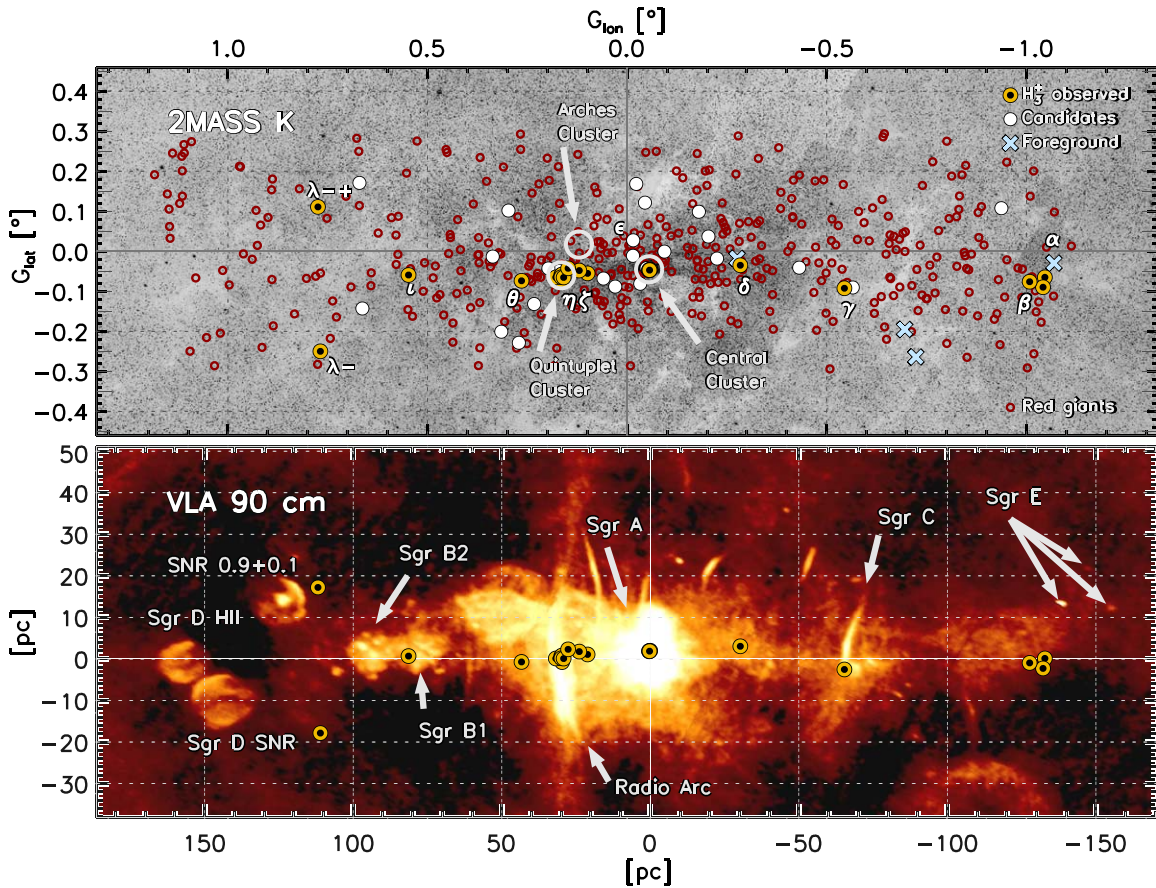
**Figure 2.** Top panel: locations of stars observed in the program. Symbols are as follows: yellow circles with dots—objects for which a set of $H_3^+$ and CO spectra have been observed; white circles—objects with clean continuum for which part of $H_3^+$ and CO spectra have been observed or are yet to be observed; red circles—red giants that have CO band head photospheric absorptions at 2.295 $\mu$m in the $K$-band medium-resolution spectroscopic survey (Geballe et al. 2019) and are not suitable for the $H_3^+$ spectroscopy; crosses—objects in front of the CMZ. All of the objects with yellow circles or white dots and a few of the objects with white circles are listed in Table 2. The three supermassive star clusters are indicated. Several stars in each of the Central Cluster and the Quintuplet Cluster overlap and are expressed with one circle. The background is the 2MASS image at $K_S$ band from Skrutskie et al. (2006). Bottom panel: locations of the stars on which a set of $H_3^+$ and CO spectra have been observed overlaid on the 90 cm radio continuum map taken from LaRosa et al. (2000). The major radio sources are marked and indicated. The projected physical distances are shown in grids centered at Sgr A$^*$, assuming a distance to the GC of 8 kpc.

is very small, on the order of 0$\farcs$00001; and (d) the column density can be simply calculated from the equivalent width without the need to consider collisions. The large emission optical depths of the highly saturated low-$J$ millimeter transitions of CO emission and observations of those lines with the large beam sizes of single-dish radio telescopes (10″–20″) both tend to give the impression that the CMZ is filled with high-density gas. Thus, infrared absorption spectroscopy of CO and $H_3^+$ toward point sources provides more reliable information on the amounts of both dense and diffuse gas.

Until very recently, almost no background sources suitable for spectroscopy of interstellar $H_3^+$ and CO on lines of sight toward the CMZ were known farther than ~30 pc from the center of the CMZ. In 2008 we initiated a search for bright, dust-embedded stars within the entire CMZ, a 10 times larger region. We first used the catalog of bright YSO candidates in the ISOGAL survey (Felli et al. 2002), which yielded one star suitable for spectroscopy of $H_3^+$, but which turned out to be in the foreground (see Section 3 and Figure 4). We then initiated a much more extensive star search using the *Spitzer Space Telescope* Galactic Legacy Infrared Mid-Plane Survey Extraordinaire (GLIMPSE) Catalog (Ramírez et al. 2008), which includes photometry from the Two Micron All Sky Survey

(2MASS) Point Source Catalog (Skrutskie et al. 2006). Out of the over 1 million objects in the catalog, 6000 stars with $L \leqslant 8$ mag are located in the central 2$\overset{\circ}{.}$39 $\times$ 0$\overset{\circ}{.}$6 (~340 $\times$ 85 pc) of the Galaxy, corresponding roughly to the dimensions of the CMZ. We dropped obvious late-type and/or low-extinction stars based on the 2MASS and GLIMPSE photometry. The remaining ~500 stars have been examined during the past 8 yr by medium-resolution $K$-band spectroscopy, which can distinguish dust-embedded stars from other stars with spectral features characteristic of red giants. For details of the star search and the $K$-band spectra of stars suitable for $H_3^+$ spectroscopy, see Geballe et al. (2019).

Plots of the survey highlighting the stars suitable for $H_3^+$ spectroscopy are shown in Figure 2. We have obtained spectra of ~40 of these stars, 29 of which show absorption by warm diffuse CMZ gas and are listed in Table 2. A very few clearly do not; these are likely to be foreground stars. For several the spectra are inconclusive, mainly due to low S/N. The newly found stars are all in the 2MASS catalog. For convenience, in discussions and compilations we have also designated these stars using the Greek alphabet from alpha to lambda (from west to east), and by adding + and − to the Greek notation as additional nearby stars are found.

**Table 2**
Targets toward Which $H_3^+$ in the CMZ Has Been Observed

| 2MASS | Star | $l$ (deg) | $b$ (deg) | $K$ (mag) | $L$ (mag) | $N(H_3^+)_{diffuse}$ [a] ($10^{15}$ cm$^{-2}$) |
|---|---|---|---|---|---|---|
| 17432173−2951430 | $\alpha$ | −1.0463 | −0.0651 | 6.484 | 3.792 | 1.57 |
| 17432823−2952159 | $\alpha+$ | −1.0417 | −0.0899 | 10.104 | 7.02 | 4.81 |
| 17432988−2950074 | $\beta$ | −1.0082 | −0.0762 | 8.823 | 4.531 | 1.53 |
| 17443734−2927557 | $\gamma-$ | −0.5651 | −0.0905 | 10.289 | 7.032 | |
| 17444083−2926550 | $\gamma$ | −0.5442 | −0.0925 | 9.404 | 6.406 | 2.87 |
| 17445895−2923259 | $\gamma+$ | −0.4604 | −0.1183 | 11.145 | 7.431 | |
| 17450483−2911464 | $\delta$ | −0.2834 | −0.0350 | 9.044 | 6.507 | |
| | GCIRS 8* | −0.0486 | −0.0422 | 13.3 | | |
| | GCIRS 10W | −0.0536 | −0.0469 | 11.170 | | |
| | GCIRS 3 | −0.0576 | −0.0461 | 10.64 | 4.84 | |
| | GCIRS 21 | −0.0561 | −0.0471 | 10.4 | 6.29 | |
| | GCIRS 16 NE | −0.0552 | −0.0467 | 9.18 | 7.16 | |
| | GCIRS 1W | −0.0549 | −0.0473 | 8.9 | 4.92 | |
| 17452861−2856049 | $\epsilon$ | −0.0150 | 0.0274 | 9.218 | 6.580 | |
| 17460215−2857235 | $\epsilon+$ | 0.0300 | −0.0882 | 8.076 | 4.197 | |
| 17460433−2852492 | NHS 21 | 0.0992 | −0.0553 | 7.558 | 4.604 | 1.03 |
| 17460562−2851319 | NHS 22 | 0.1200 | −0.0482 | 7.462 | 6.369 | |
| 17460825−2849545 | NHS 42 | 0.1479 | −0.0426 | 8.325 | 6.613 | 3.03 |
| 17461524−2850035 | NHS 25 | 0.1591 | −0.0654 | 7.291 | 5.629 | |
| 17461783−2850074 | $\eta$ | 0.1631 | −0.0742 | 7.84 | 5.519 | |
| 17461412−2849366 | GCS 3-4 | 0.1634 | −0.0581 | 7.717 | 3.903 | |
| 17461471−2849409 | GCS 3-2 | 0.1635 | −0.0605 | 7.293 | 3.162 | 3.48 |
| 17461586−2849456 | GCS 4 | 0.1646 | −0.0647 | 7.236 | 3.527 | |
| 17461481−2849343 | GCS 3-1 | 0.1652 | −0.0598 | 7.52 | 4.693 | |
| 17461798−2849034 | FMM 362 | 0.1787 | −0.0653 | 7.094 | 6.41 | 2.63 |
| 17463219−2844546 | $\theta$ | 0.2647 | −0.0738 | 9.209 | 6.381 | 3.37 |
| 17470898−2829561 | $\iota$ | 0.5477 | −0.0593 | 10.445 | 6.579 | |
| 17482472−2824313 | $\lambda-$ | 0.7685 | −0.2501 | 9.539 | 6.721 | 2.85 |
| 17470137−2813006 | $\lambda-+$ | 0.7746 | 0.1108 | 9.978 | 7.062 | |

**Note.**
[a] $N(H_3^+)_{diffuse}$ is the total column density in $10^{15}$ cm$^{-2}$ of $H_3^+$ in the diffuse gas of the CMZ. In addition to sight lines listed in this table, the following sight lines have been observed, but $H_3^+$ in the CMZ has not been definitely detected: 17431001−2951460 ($\alpha-$), 17445538−2941284 ($\beta+$), 17444319−2937526 ($\beta++$), 17443734 −2927557 ($\gamma-$), 17451618−2903156 (ISOGAL), 17452861−2856049 ($\epsilon$), 17460215−2857235 ($\epsilon+$), 17474486−2826365 ($\kappa$), 17473680−2816005 ($\lambda$). Some of these are believed to be foreground stars.

## 2.3. Spectrometers and Telescopes

Five infrared spectrographs at five different telescopes have been used to obtain the spectra presented here, three in Hawaii and two in Chile. Cold Grating Spectrometer 4 (CGS4), with a spectral resolution of $R \sim 40,000$, was used on the 3.8 m United Kingdom Infrared Telescope (UKIRT) from 1997 to 2004. The 8.2 m Subaru Telescope's Infrared Camera and Spectrograph (IRCS), with $R \sim 20,000$, was used from 2001 to 2015. The Phoenix spectrometer, with $R \sim 60,000$, was employed from 2003 to 2010 and from 2016 to 2017 at the 8.1 m Gemini South telescope. The Cryogenic Infrared Echelle Spectrograph (CRIRES), with $R \sim 50,000$–$100,000$, was used in 2007 on the 8.2 m Very Large Telescope (VLT) of the Paranal Observatory. The Gemini Near-Infrared Spectrograph (GNIRS), with $R \sim 20,000$, was used from 2011 to 2014 at the 8.1 m Frederick C. Gillett Gemini North telescope. Details of the operation of these spectrometers and data reduction procedures are given in Geballe et al. (1999) for CGS4, Goto et al. (2002) for IRCS, McCall et al. (2002) for Phoenix, Goto et al. (2014) for CRIRES, and Geballe et al. (2015) for GNIRS.

The IRCS, which contains an echelle and a cross-dispersion grating, allows multiple $H_3^+$ lines to be observed simultaneously (see Goto et al. 2002). For the other spectrometers the key lines can only be made one line at a time, except for the $R(1, 0)$–$R(1, 1)^u$ pair, which are separated by 0.322 cm$^{-1}$, and, for the GNIRS, this pair and the $R(1, 1)^l$ line, which are separated by 35 cm$^{-1}$. In contrast, all strong lines of the CO overtone $R$-branch are closely spaced in wavelength and could be observed simultaneously by all spectrographs. Absorption lines of $H_3^+$ in diffuse clouds have depths on the order of 0.5%–15%, requiring integration times sufficient for the S/Ns of up to few hundred on the continua of the background stars. Depending on the spectrometer and the brightness of stars, this required exposure times of 10 minutes to a few hours. Altogether, $\sim$100 lines of $H_3^+$ have been observed, amounting to a total integration time of several hundred hours. The CO lines typically have higher absorption depths than the $H_3^+$ lines, and for them S/Ns of $\sim$30 were sufficient.

## 3. Description of Spectra

Spectra of many of the suitable background stars in lines of $H_3^+$ and CO are shown in Figures 3–8. The spectra display a wide variety of profiles and are grouped so as to illustrate key characteristics. Each figure is described briefly below and is discussed in detail in Section 4.

Figure 3 contains spectra, obtained with Phoenix in 2003, of the $R(1, 1)^l$ line of $H_3^+$ toward four of the five bright infrared Quintuplet sources located close to the center of the Quintuplet Cluster. The spectra are nearly identical, which is perhaps not
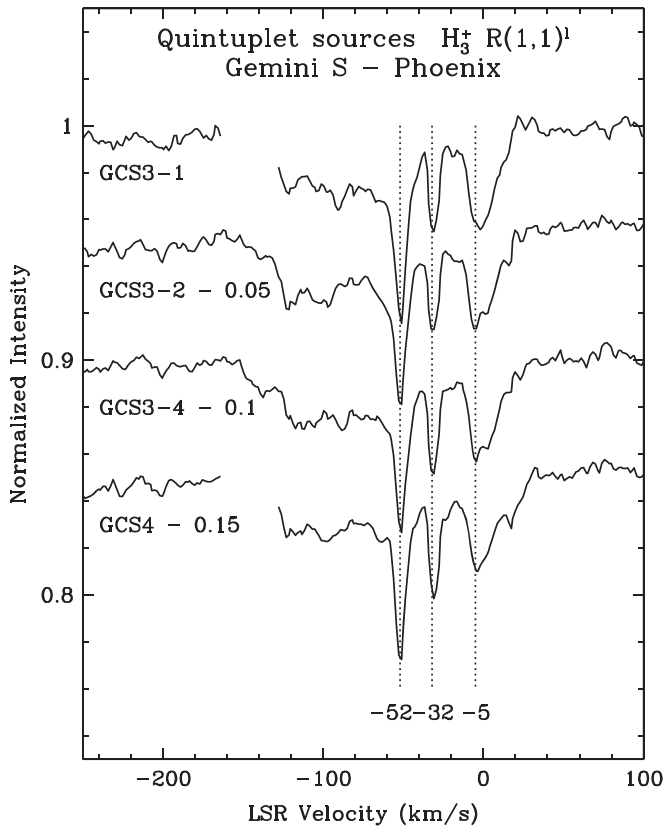
**Figure 3.** $H_3^+$ $R(1, 1)^l$ absorption toward four brighter stars of the Quintuplet Cluster observed by the Phoenix Spectrometer at the Gemini South Observatory. The three sharp absorptions at velocities of $-52$, $-32$, and $-5$ km s$^{-1}$ arise in the three foreground spiral arms. Note the presence of broad absorption troughs, due to $H_3^+$ in the CMZ, in addition to the narrow features.

**Figure 4.** Spectra of the $H_3^+$ $R(1, 1)^l$ line toward six stars near the Quintuplet Cluster. The three sharp absorptions at $\sim -52$, $-32$, and $-5$ km s$^{-1}$ are due to $H_3^+$ in the foreground three spiral arms. The spectra of GCS 4, NHS 25, NHS 42, and FMM 362 show troughs from $-150$ to $0$ km s$^{-1}$ with similar equivalent widths, while the spectrum of NHS 21 shows a weaker trough with a gap between $-100$ and $-80$ km s$^{-1}$. The bottom spectrum toward the 2MASS/ISOGAL star J17451618−2903156 has no absorption trough, only the narrow features arising in the spiral arms, indicating that this star lies between the CMZ and the 3 kpc arm.

surprising given the proximities of the stars to one another. Noteworthy features of the spectra are the three sharp absorptions at $-52$, $-32$, and $-5$ km s$^{-1}$ (LSR) due to $H_3^+$ in the three foreground spiral arms, the 3 kpc (Rougoor & Oort [1960]; Oort [1977]), 4.5 kpc or Norma (Menon & Ciotti [1970]), and Local arms, respectively, and a broad absorption trough extending from negative velocities as high as $-150$ km s$^{-1}$ to $0$ or slightly positive velocities. The same features with similar depths are seen toward sources in the Central Cluster (e.g., Goto et al. [2014], Figure 3). As discussed later in this paper, and as argued in previous papers (e.g., Oka et al. [2005]), this high-dispersion gas is located within the CMZ. The almost entirely negative absorption velocities imply that the vast majority of the gas is moving outward from the central region of the CMZ.

Figure [4] contains spectra of the same line of $H_3^+$, obtained in 2008 toward GCS 4, one of the Quintuplet stars observed in 2003, and five other stars near the Quintuplet Cluster, all observed using Phoenix. The spectra of GCS 4 in this figure and in Figure [3], obtained 5 yr apart, are essentially identical. The spectra of three of the five other stars show both the same narrow galactic spiral arm absorption features and the same broad absorption trough as the Quintuplet stars. The general similarity of these troughs to those seen toward the Quintuplet and Central Clusters indicates that the outward-moving, high-dispersion gas is not localized to a small region but is seen on sight lines covering an extended region of the CMZ near its center. Toward one of the stars, NHS 21, a portion of the trough, between $-100$ and $-80$ km s$^{-1}$, is missing, and the
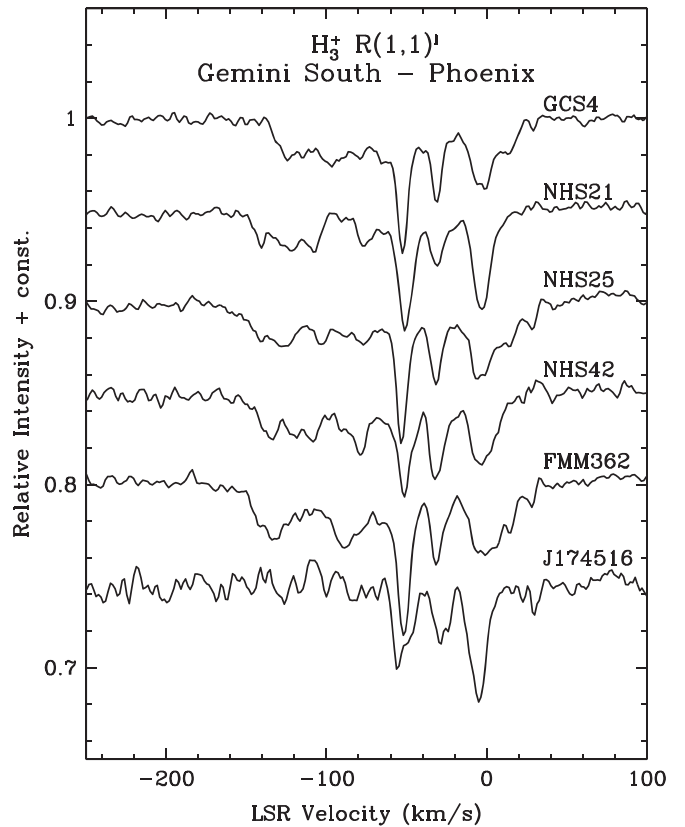
trough between $-80$ and $0$ km s$^{-1}$ is weaker than the previously described stars. The spectrum observed toward 2MASS J17451618−2903156 (bottom of the figure) differs greatly from all of the others in that the trough is completely absent. Our interpretations of the spectra of NHS 21 and J17451618 are given in Section [4.1].

Figure [5] contains spectra of the Quintuplet source GCS 3-2, which can be regarded as prototypical of stars located in the central part of the CMZ, and of two stars located near the western and eastern edges of the CMZ, J17432173−2951430 ($\alpha$) and J17470898−2829561 ($\iota$). The spectra shown for each of these stars are of the $H_3^+$ $R(1, 1)^l$ line and the four lowest-lying $R$-branch lines of CO. J17432173 ($\alpha$) is situated near the radio source Sgr E, while J17470898 ($\iota$) is located 85 pc west of Sgr A*, in the Sgr B molecular cloud complex between Sgr B1 and Sgr B2. All of the spectra were obtained with Phoenix at Gemini South and have been published earlier (Oka et al. [2005]; Geballe & Oka [2010]). They illustrate the most extreme differences in velocity profiles that we have found for sight lines in the CMZ.

Toward GCS 3-2 the CO absorptions consist almost entirely of the three narrow spiral arm features, with no evidence for the broad trough that is present in the $H_3^+$ line along with the narrow features. The spectra toward the other two stars in Figure [5] are strikingly different from both each other and the spectra of
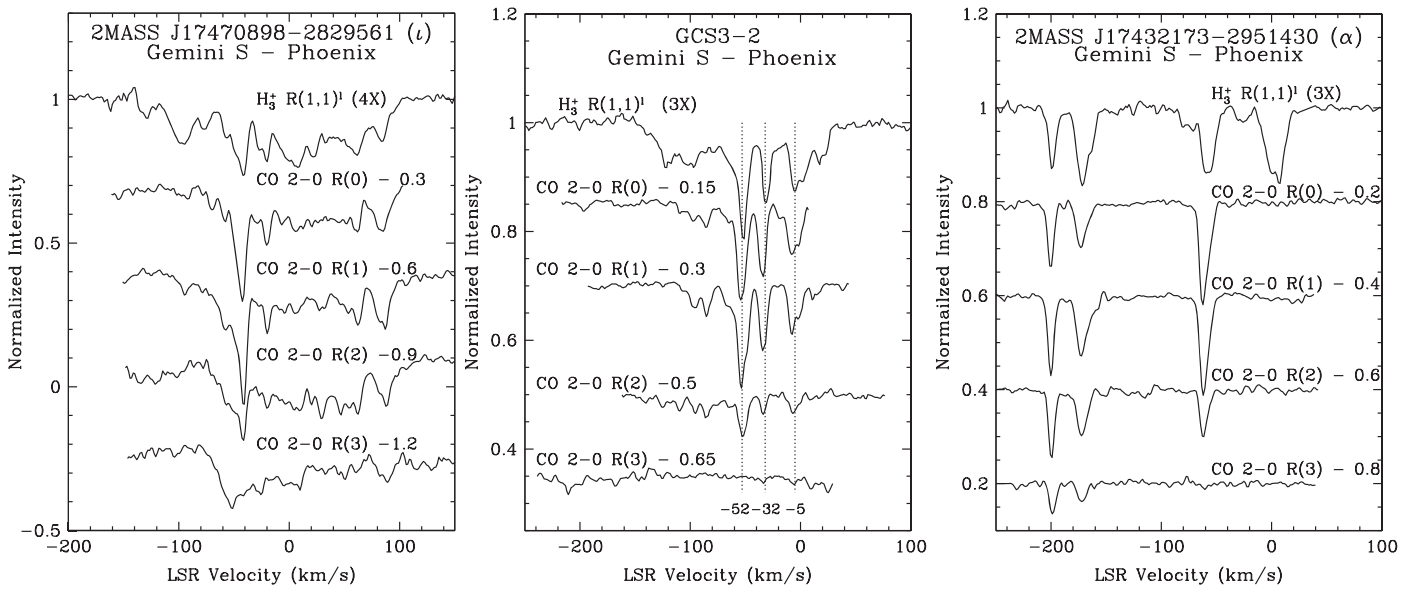
**Figure 5.** $R(1, 1)^l$ absorption spectra of $H_3^+$ (top traces) and CO overtone band absorption lines toward three stars located near the western edge (right panel), in the center (middle panel), and between Sgr B1 and B2, 85 pc to the east of center (left panel).

GCS 3-2 and other stars in the central region of the CMZ (e.g., those with spectra shown in Figures 3 and 4). J17432173 ($\alpha$) exhibits three narrow blueshifted absorption features in both $H_3^+$ and CO, only one of which, near $-60 \, \mathrm{km \, s^{-1}}$, corresponds to a foreground spiral arm. Its spectra also contain a prominent absorption feature in $H_3^+$ near $0 \, \mathrm{km \, s^{-1}}$, a velocity that approximately matches that expected from absorption by the Local Arm, but with no counterpart absorption at that velocity in CO, unlike the Quintuplet and Central Cluster sources. In contrast, the spectra of J17470898 ($\iota$) have much more complex absorption profiles extending over $\sim 200 \, \mathrm{km \, s^{-1}}$ in both species. Some narrow absorption features, e.g., those at $-45$ and $+80 \, \mathrm{km \, s^{-1}}$, are present in both species, while others, e.g., at $-130$ and $-100 \, \mathrm{km \, s^{-1}}$, are only present in $H_3^+$. These spectra are discussed in Sections 4.2.1–4.2.3.

Figure 6 contains spectra of the four lowest-lying $R$-branch transitions of the $v = 2 \leftarrow 0$ band of CO toward nine stars scattered across the CMZ, obtained with Phoenix at Gemini South. As discussed in Section 4.1, the strengths of $H_3^+$ absorption features due to gas in the CMZ indicate that all are deeply embedded in the CMZ. However, with the exceptions of J17432173 ($\alpha$) at top left and J17470898 ($\iota$) at bottom right these CO spectra are dominated by narrow absorption features whose velocities match those of the foreground spiral arms. In dense clouds, CO produces strong infrared absorption features, yet no additional strong absorption features attributable to dense clouds in the CMZ are seen toward the other 10 stars. The interpretations of these spectra are given in Section 4.1.

Figure 7 contains velocity profiles of the $H_3^+$ $R(1, 1)^l$ and $R(3, 3)^l$ lines toward nine stars in the CMZ, as observed by CGS4 at UKIRT, Phoenix at Gemini South, IRCS at Subaru, GNIRS at Gemini North, and CRIRES at the VLT. As explained in Section 1.6, the presence of the $R(3, 3)^l$ line is a hallmark of warm gas. To date that line has been detected nowhere else in the Galaxy except in the CMZ, whereas the $R(1, 1)^l$ absorption line, which originates from the lowest energy level of $H_3^+$, is observed both in the CMZ and in cold foreground clouds. The presence of the $R(3, 3)^l$ line on nearly all sight lines to sources in the direction of the CMZ that have

been observed to date indicates that the surface filling factor of the warm gas in the CMZ is near unity. As discussed in Section 5, it is highly likely that this warm gas fills a large fraction of the front half of the CMZ.

Figure 8 is a comparison of spectra, obtained at Subaru, of the $R(1, 1)^l$ and $R(2, 2)^l$ lines toward nine stars located within the CMZ. As explained in Section 1.6, in warm diffuse gas the strength of the $R(2, 2)^l$ line relative to $R(1, 1)^l$ is highly sensitive to density. In the CMZ the $R(2, 2)^l$ line has been detected only toward J17470898 ($\iota$) in the Sgr B complex (as shown in the figure) and toward GCIRS 3 in the Central Cluster, whose sight line intersects dense gas in the 2 pc diameter circumnuclear ring (Goto et al. 2014). The nondetection of this line on all other CMZ sight lines known to contain warm gas (by virtue of the presence of absorption by the $R(3, 3)^l$ line) implies that the portions of those sight lines passing through the CMZ cross low-density gas only.

## 4. Interpretation

Here we address, in considerably more detail than in the previous largely descriptive section, numerous issues regarding the interpretation of the spectra, presented here and elsewhere, of $H_3^+$ and CO toward stars within the CMZ.

### 4.1. How Deeply Are the Survey Stars Embedded in the CMZ?

A major question in interpreting infrared absorption spectroscopy of an object located within a region with high extinction is the depth of the object within the obscuring material. If the extinction within the CMZ is sufficiently large, then a brightness-limited CMZ survey such as ours will tend to select sources that are more shallowly embedded in the CMZ than average. There has been some thought that this selection effect is quite significant for the objects whose absorption spectra we have been measuring and that the stars we have observed are in the outer part of the CMZ, close to its front surface.

Toward the Central Cluster, a region of diameter $\sim 3 \, \mathrm{pc}$, containing many luminous stars and centered on Sgr A*, is arguably at the center of the CMZ; this possibility has been
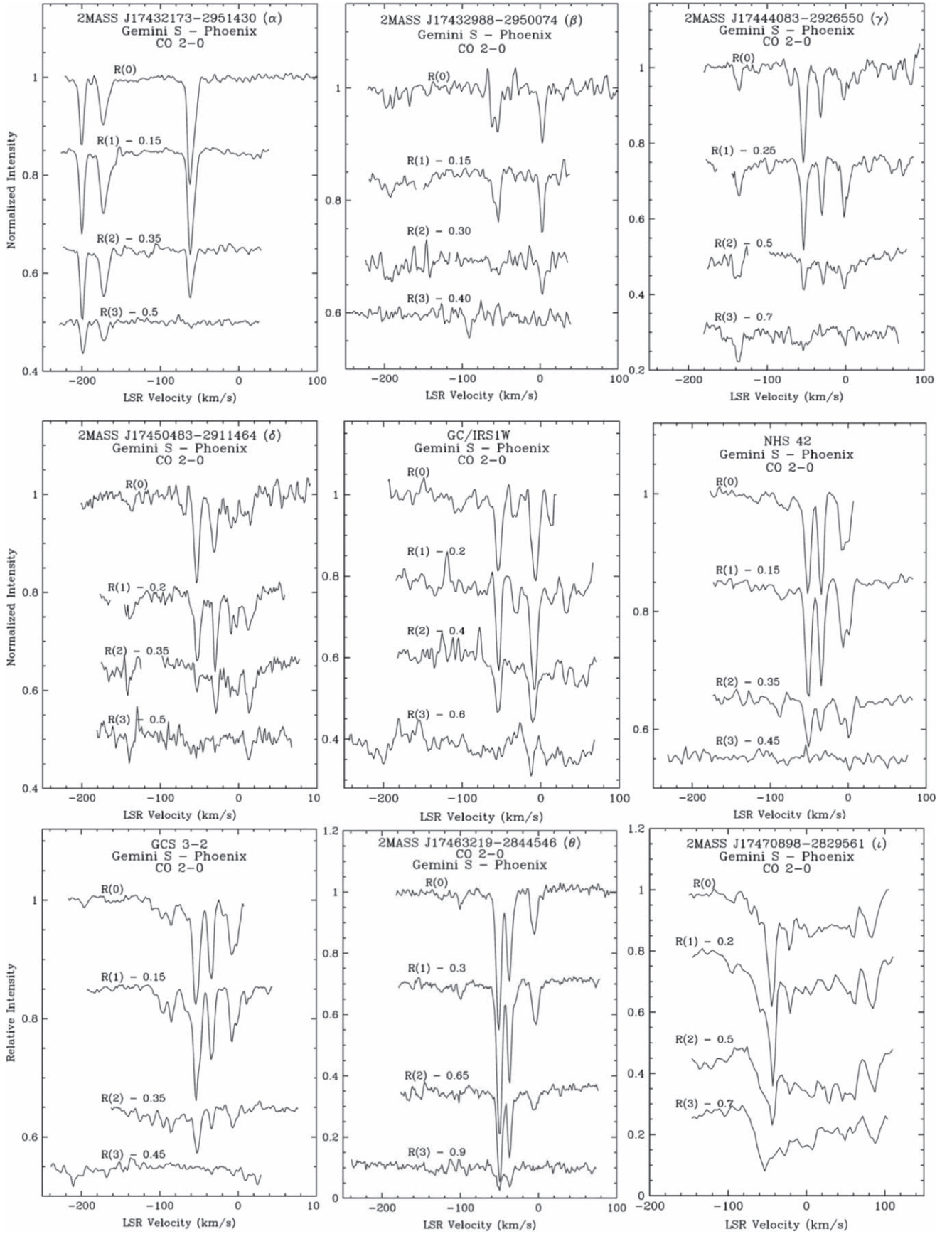
**Figure 6.** The $\nu = 2 \leftarrow 0$ first-overtone absorption lines $R(0)$, $R(1)$, $R(2)$, and $R(3)$ observed toward nine stars in the CMZ using the Phoenix Spectrometer at the Gemini South Observatory. The $H_3^+$ absorptions toward these stars indicate that the stars are all deeply embedded in the CMZ. Note that except for the stars J17432173 $-2951430$ ($\alpha$) (top left), which is in the Sgr E complex, and J17470898$-2829561$ ($\iota$) (bottom right) in the Sgr B complex, the CO spectra are dominated by absorptions due to the three foreground spiral arms, the 3 kpc arm, the 4.5 kpc arm, and the Local Arm.
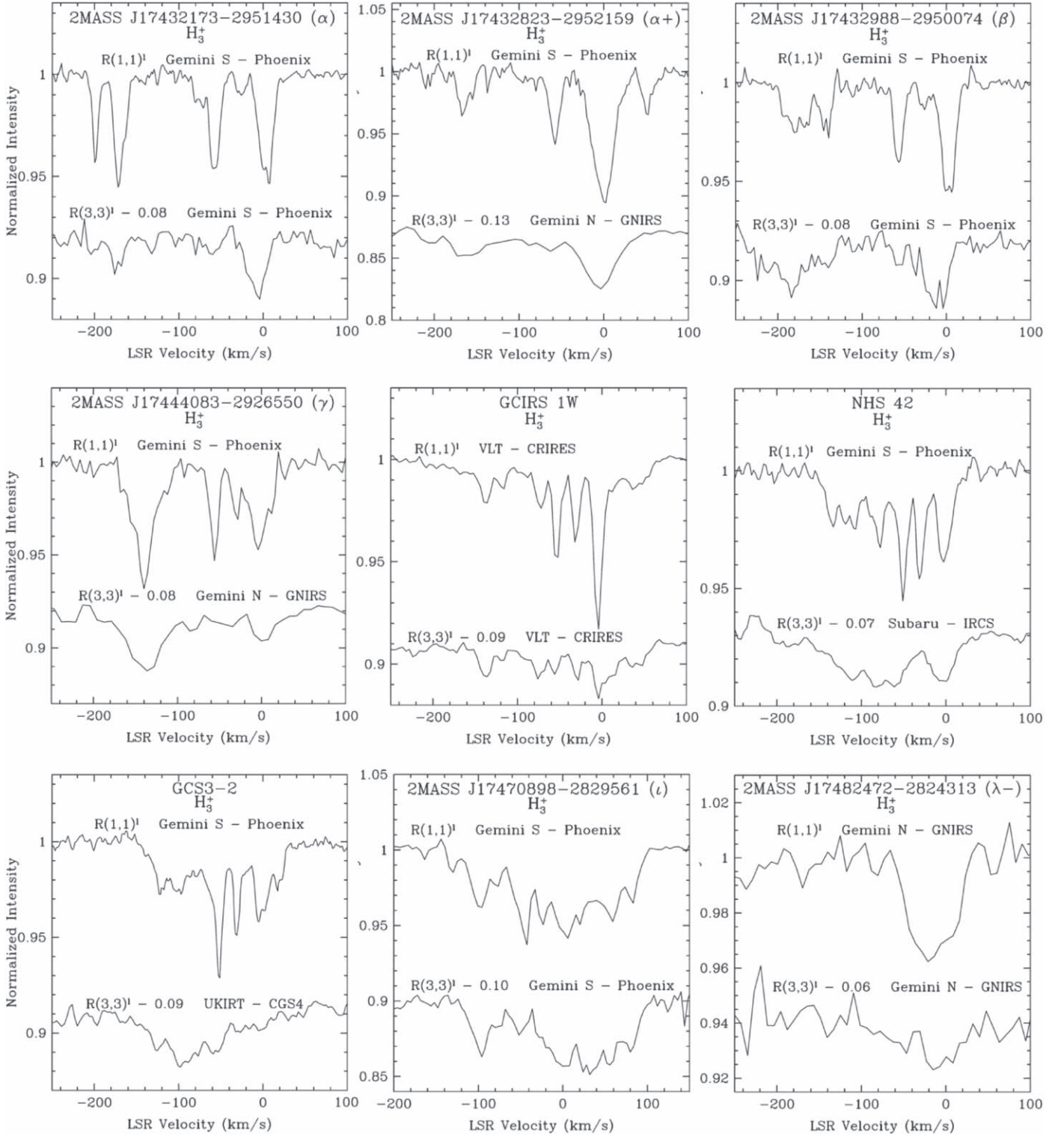
**Figure 7.** $R(1, 1)^l$ (upper trace) and $R(3, 3)^l$ (lower trace) absorption lines of $H_3^+$ toward 10 stars in the CMZ. The $R(1, 1)^l$ absorption profiles include $H_3^+$ in both the CMZ and the three foreground spiral arms, while the $R(3, 3)^l$ absorption is entirely from $H_3^+$ in the CMZ.

decisively negated by observations of many bright infrared stars of the Central Cluster (e.g., Viehmann et al. 2005). As discussed in Section 1.2, these stars suffer extinctions of only ∼30 visual magnitudes, corresponding to ∼3 and ∼1 mag in the $K$ and $L$ bands, respectively (Rieke & Lebofsky 1985), of which some occurs outside of the CMZ (e.g., in the foreground spiral arms). Our survey stars range in $L$ magnitude from 3 to 8,

suggesting a wide range of intrinsic stellar brightness and that extinction influencing the selection of targets is a minor issue, at least to the depth of the Central Cluster. Our spectral lines of the CO $v = 2 \leftarrow 0$ band toward these sources show little or no absorption due to dense clouds, apart from those in the three foreground spiral arms (see, e.g., Figure 6 and Goto et al. 2014, Figure 3). Clearly, giant molecular clouds do not exist in the
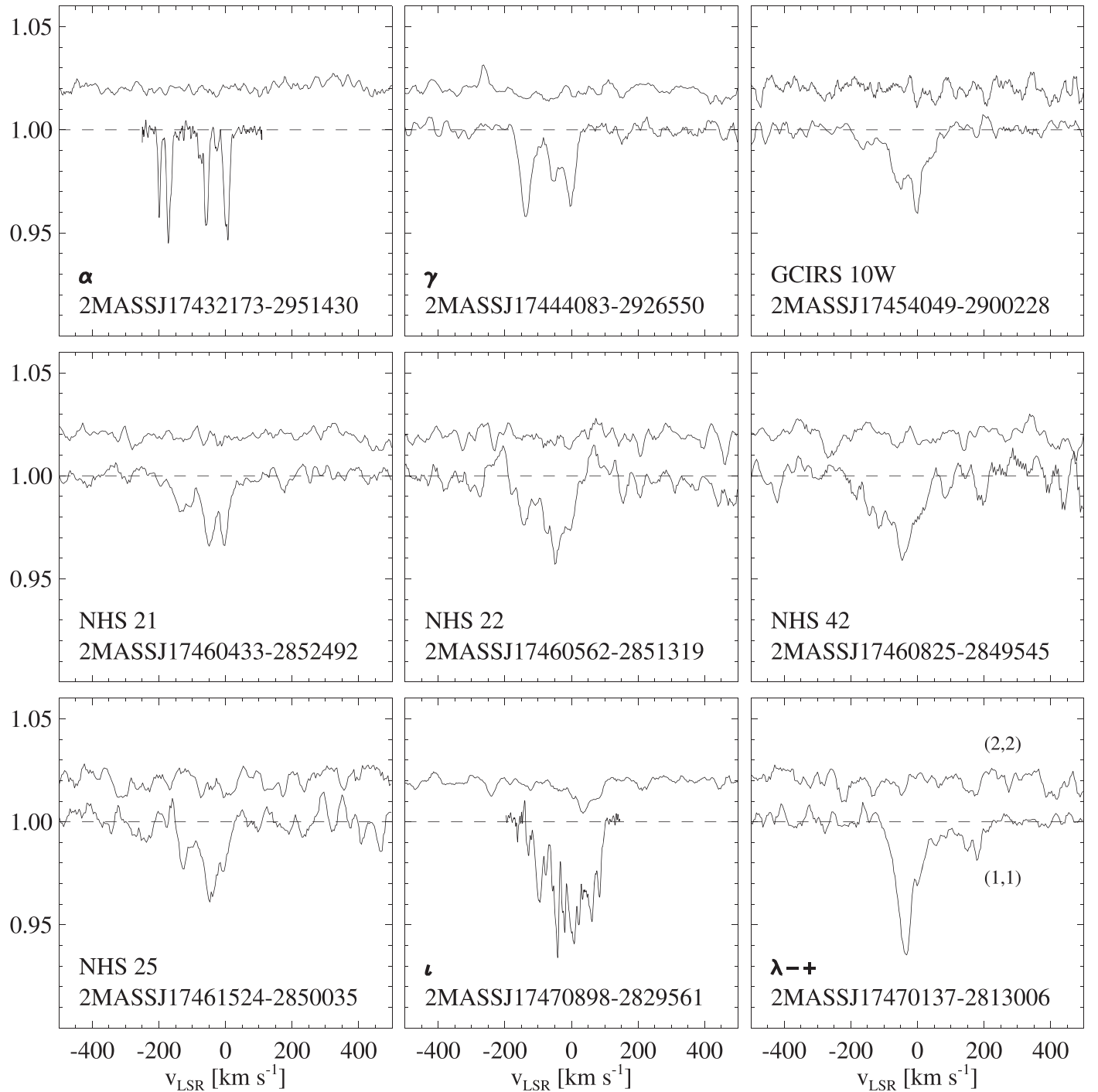
**Figure 8.** Comparison of the $R(1, 1)^l$ spectra from the (1, 1) ground rotational level (lower traces) and the $R(2, 2)^l$ spectra from the unstable (2, 2) level (upper traces) toward nine stars observed by the IRCS spectrometer of the Subaru Telescope. The $R(2, 2)^l$ absorption is definitively detected only toward J17470898−2829561 (ι), indicating that sight lines toward other stars cross low-density gas only.

CMZ in front of the Central Cluster; any such clouds that exist on that general sight line must be located behind the Central Cluster.

The Quintuplet Cluster is also thought to be located deep within the CMZ and close to the Central Cluster, as is the Arches Cluster, with all three clusters having formed in the past few to several million years (e.g., Espinoza et al. 2009; Schneider et al. 2014). As in the case of the Central Cluster, our spectra of CO $v = 2 \leftarrow 0$ band lines (e.g., GCS 3-2 in Figures 5 and 6) toward Quintuplet Cluster stars show no

evidence for large dense clouds in the front half of the CMZ on these sight lines. In addition, the high total column densities of $H_3^+$ in the absorption troughs, on the order of $3 \times 10^{15}\,cm^{-2}$, observed toward GCS 3-2 (Oka et al. 2005) and the other GCS stars (see Figure 3), are comparable to those toward the stars in the Central Cluster (Goto et al. 2008, 2013, 2014), which is an argument for the Quintuplet Cluster being as deeply embedded as the Central Cluster. Finally, the extinctions to stars in those two clusters (Liermann et al. 2010) are comparable. Thus, the evidence is overwhelming that the Quintuplet Cluster is as

deeply embedded in the CMZ as the Central Cluster. The extinction to the Arches Cluster (Habibi et al. 2013) is similar to that to the Quintuplet Cluster, indicating that it is as deeply embedded in the CMZ as the other two clusters. However, the stars of the Arches Cluster are too faint for high-resolution spectroscopy of $H_3^+$, as they are still on the main sequence and less luminous than the more evolved stars in the Quintuplet Cluster.

The depths in the CMZ of the other stars that we have observed are not known. However, the observed column densities of warm $H_3^+$ in Table 2 give an approximate idea of their depths inside the CMZ. This is because the ubiquity of the $R(3, 3)^l$ line (Figure 7) indicates that the surface filling factor of the CMZ's warm diffuse gas approaches 100%. Its volume filling factor is likely more than 50%, at least for the front hemisphere of the CMZ, as estimated in Section 5. This, together with the constancy of the $H_3^+$ number density (see Figure 3 of Oka 2013), makes the column density of warm $H_3^+$ in diffuse clouds an approximate yardstick for measuring the depths of stars in the CMZ.

The absorption profiles of the $H_3^+$ $R(1, 1)^l$ line toward six stars near the Quintuplet Cluster, shown in Figure 4, illustrate this. After excluding the three sharp absorption components due to $H_3^+$ in dense clouds in the three foreground spiral arms, there remain broad blueshifted absorption "troughs" extending from $\sim -150$ to near $0\,\mathrm{km\,s^{-1}}$, similar to those seen in the Quintuplet and Central Clusters. Similar to the stars in the Quintuplet and Central Clusters, the troughs are due to warm diffuse gas. The large equivalent widths, comparable to those of the cluster stars, toward four of these stars, GCS 4 (which is a member of the Quintuplet Cluster) NHS 25, NHS 42, and FMM 362, indicate that they are as deeply embedded in the CMZ as the Central Cluster. The spectrum of NHS 21 is somewhat different; the trough is not as deep and has a gap from $-100$ to $-80\,\mathrm{km\,s^{-1}}$. That suggests that NHS 21 is located somewhat in front of the aforementioned four stars, although still within the CMZ and much of the outwardly moving diffuse gas. The difference between the spectra of these five stars and that of J174516 (ISOGAL bottom spectrum) is much more pronounced, as a trough in the latter is completely absent. The narrow spiral arm features are still present in its spectrum, however, implying that J174516 lies between the outer (front) edge of the CMZ and the innermost (3 kpc) arm.

Some of the other stars that have been observed in $H_3^+$ also appear to be more shallowly embedded in the CMZ. Figure 7 contains spectra of one example, J17444083$-$2926550 ($\gamma$), which is located roughly midway between the center of the CMZ and its western edge. Its spectra show strong absorption by warm diffuse gas at high negative velocities, but little or no absorption by warm diffuse gas at less negative velocities, where the trough is prominent toward stars located near the center of the CMZ. Like the spectrum of this star, the spectra of other stars on similarly situated sight lines tend to show their strongest absorption by warm diffuse gas at the high negative velocity end of the absorption trough.

### 4.2. Differentiating between Dense and Diffuse Gas

The state of carbon changes from $C^+$ to C to CO as cloud density changes from diffuse to dense (e.g., Figure 1 of Snow & McCall 2006). On the other hand, $H_3^+$ exists in any interstellar environment as long as $H_2$ abounds, that is, in diffuse molecular clouds as well as in dense clouds. Thus, as

discussed in Section 1.8, high-resolution spectra of infrared CO and $H_3^+$ absorption lines on the same sight line can allow one to discriminate between $H_3^+$ in diffuse molecular clouds and in dense clouds. The spectra in Figure 5 demonstrate three strikingly different examples of the use of this property.

#### 4.2.1. GCS 3-2: Diffuse Blueshifted Gas

The Quintuplet Cluster star GCS 3-2, the brightest infrared star in the CMZ that we have employed as a background source ($L = 3.16$ mag), is located 30.7 pc to the east of Sgr A$^*$ and 2.0 pc below the Galactic plane. Its CO overtone spectrum (middle panel of Figure 5) is dominated by CO in dense clouds in the three foreground spiral arms at $-52$, $-32$, and $-5\,\mathrm{km\,s^{-1}}$. The only additional absorptions due to CO, at $-123$, $-97$, and $+19\,\mathrm{km\,s^{-1}}$, are weak, indicating that there is little dense gas within the CMZ on this sight line. As pointed out earlier, this paucity of dense CMZ gas is generally found toward all of the stars observed by us except those near Sgr E (Section 4.2.2) and Sgr B (Section 4.2.3). The $H_3^+$ $R(1, 1)^l$ spectrum in the same figure contains absorption features at the above six velocities, indicating that the absorbing $H_3^+$ responsible for those features must be in the same dense clouds. Removing them (by chopping them off as in Figure 4 of Oka et al. 2005) leaves a wide trough of absorption by $H_3^+$, from $-150$ to $+32\,\mathrm{km\,s^{-1}}$, arising in diffuse molecular clouds in the CMZ. Also as pointed out earlier, this gas is much warmer than diffuse gas in the Galactic disk. Blueshifted $H_3^+$ absorption troughs of similar depth and velocity extent are present toward many stars located in the central regions of the CMZ (e.g., Figure 4). This suggests that the blueshifted warm diffuse gas occupies a region of large and continuous or near-continuous radial extent in the front half of the CMZ, presumably with the highest velocities closest to the front edge and the lowest velocities near the center. The extensions of the troughs to slightly redshifted velocities observed on sight lines to GCS 3-2 and some of the stars in Figures 3 and 4 could mean that those stars are located slightly behind the region from which gas is being or has been ejected.

#### 4.2.2. J17432173$-$2951430 ($\alpha$): Diffuse Gas Moving Perpendicular to the Sight Line

This bright star ($L = 3.79$ mag), located 139 pc to the west of Sgr A$^*$ and 2.7 pc below the Galactic plane, near Sgr E and the western edge of the CMZ, most simply demonstrates the use of the CO overtone spectrum for discriminating between the $H_3^+$ in diffuse and dense clouds. The $H_3^+$ spectrum (right panel of Figure 5) is composed of four prominent absorptions at LSR velocities $-200\,\mathrm{km\,s^{-1}}$ (depth 4.4%), $-172\,\mathrm{km\,s^{-1}}$ (5.6%), $-60\,\mathrm{km\,s^{-1}}$ (4.6%), and a blend at 0 and $+8\,\mathrm{km\,s^{-1}}$ (5.4%), together with two much weaker absorptions at $-27\,\mathrm{km\,s^{-1}}$ (0.9%) and a doublet centered at $-75\,\mathrm{km\,s^{-1}}$ (1.5%). Three of the four deep $H_3^+$ absorptions are accompanied by CO absorption at the same velocities; thus, we interpret them as arising in dense gas. Of these, the two highest negative velocities agree with the velocities of $\sim -200\,\mathrm{km\,s^{-1}}$ observed toward the Sgr E complex in $^{13}$CO and the H70$\alpha$ radio recombination line by Liszt (1992) and more precisely with $-207$ and $-174\,\mathrm{km\,s^{-1}}$ of the CO cloud used for observations of $N^+$ and $C^+$ by Langer et al. (2015). Thus, these two dense clouds lie within the CMZ. They are fairly compact, as they are only seen over a small region in the CMZ. Where

**Table 3**
CO Column Densities toward Stars in the CMZ

| Star | Location | $v$ (km s$^{-1}$) | $\Delta v$ (km s$^{-1}$) | $N(0)$ ($10^{17}$ cm$^{-2}$) | $N(1)$ ($10^{17}$ cm$^{-2}$) | $N(2)$ ($10^{17}$ cm$^{-2}$) | $N(3)$ ($10^{17}$ cm$^{-2}$) | $N(\mathrm{CO})_{\mathrm{cloud}}$ ($10^{17}$ cm$^{-2}$) | $N(\mathrm{CO})_{\mathrm{total}}$ ($10^{17}$ cm$^{-2}$) | $A_V$ (mag) |
|---|---|---|---|---|---|---|---|---|---|---|
| | arm 1 | −62 | 26 | 4.22 | 5.94 | 2.81 | 0.25 | 12.7 | arm 12.7 | arm 13 |
| $\alpha$ | CMZ | −173 | 26 | 2.17 | 5.00 | 3.62 | 1.18 | 12.0 | CMZ 22.0 | CMZ 22 |
| | CMZ | −200 | 19 | 1.83 | 3.67 | 3.02 | 1.48 | 10.0 | | |
| | arm 3 | +3 | 15 | 1.33 | 2.14 | 2.05 | ... | 5.5 | arms 10.4 | arms 10 |
| $\beta$ | arm 1 | −58bl | 24 | 1.61 | 1.92 | 1.33 | ... | 4.9 | | |
| | CMZ | −193 | 17 | 0.82 | 1.38 | 1.89 | ... | 4.1 | CMZ 4.1 | CMZ 4 |
| | arm 3 | −1 | 22 | 1.83 | 3.66 | 2.01 | 0.76 | 8.3 | arms 24.0 | arms 24 |
| $\gamma$ | arm 2 | −32 | 14 | 1.57 | 2.28 | 1.09 | ... | 3.9 | | |
| | arm 1 | −54 | 18 | 3.66 | 4.67 | 1.61 | 0.84 | 10.8 | | |
| | CMZ | −136 | 15 | 0.87 | 1.85 | 2.61 | 2.91 | 8.2 | CMZ 8.2 | CMZ 8 |
| | CMZ | +13 | 19 | 1.35 | 2.82 | 2.85 | 1.27 | 8.3 | | |
| | arm 3 | −6bl | 18 | 1.59 | 2.68 | 2.77 | 0.63 | 7.7 | | |
| $\delta$ | arm 2 | −30 | 18 | 2.29 | 3.55 | 2.05 | ... | 7.9 | arms 23.5 | arms 24 |
| | arm 1 | −53 | 18 | 2.75 | 4.09 | 1.09 | ... | 7.9 | | |
| | CMZ | −143 | 14 | 0.69 | 2.10 | 1.61 | 0.68 | 5.1 | CMZ 13.4 | CMZ 13 |
| | CMZ | +57 | 13 | 0.65 | ... | 1.41 | ... | 2.1 | CMZ 4.8 | CMZ 5 |
| | CMZ | +44 | 13 | ... | ... | 1.49 | 1.22 | 2.7 | | |
| GCIRS 21 | arm 3 | −2 | 27 | 7.86 | 10.17 | 7.92 | 4.81 | 30.8 | | |
| | arm 2 | −31 | 12 | 1.64 | 1.99 | 1.01 | ... | 4.6 | arms 45.9 | arms 46 |
| | arm 1 | −55 | 20 | 4.07 | 4.24 | 2.21 | ... | 10.5 | | |
| | CMZ | +68 | 34 | ... | ... | ... | 5.99 | 6.0 | | |
| | CMZ | +44 | 13 | 1.35 | ... | 2.45 | 1.06 | 4.9 | CMZ 24.9 | CMZ 25 |
| | CMZ | +25 | 26 | 2.72 | 5.18 | 3.02 | 1.10 | 12.0 | | |
| GCIRS 3 | arm 3 | −2 | 27 | 7.95 | ... | ... | 1.86 | 9.8 | | |
| | arm 2 | −31 | 12 | 2.51 | 3.00 | ... | ... | 5.5 | arms 23.5 | arms 24 |
| | arm 1 | −55 | 20 | 3.64 | 3.58 | 1.01 | ... | 8.2 | | |
| | CMZ | −74 | 17 | 0.70 | 0.43 | 0.88 | ... | 2.0 | | |
| | CMZ | +57 | 13 | 0.22 | 1.45 | 1.29 | ... | 3.0 | | |
| | CMZ | +44 | 13 | 0.24 | 1.67 | 1.37 | ... | 3.3 | CMZ 14.8 | CMZ 15 |
| | CMZ | +25 | 26 | ... | 1.67 | 3.38 | 1.90 | 7.0 | | |
| GCIRS 16NE | arm 3 | −2 | 27 | 5.78 | 9.41 | 8.44 | 2.79 | 26.4 | | |
| | arm 2 | −31 | 12 | 1.54 | 1.74 | 1.13 | ... | 4.4 | arms 44.0 | arms 44 |
| | arm 1 | −55 | 20 | 3.90 | 6.15 | 2.41 | 0.72 | 13.2 | | |
| | CMZ | −74 | 17 | 0.51 | 1.01 | ... | ... | 1.5 | | |
| | CMZ | +57 | 13 | 0.63 | 1.19 | ... | 0.72 | 2.5 | | |
| | CMZ | +44 | 13 | 2.39 | 4.53 | 5.67 | 2.74 | 15.3 | CMZ 27.7 | CMZ 28 |
| GCIRS 1W | CMZ | +25 | 26 | 1.88 | 4.63 | 2.01 | 1.39 | 9.9 | | |
| | arm 3 | −2 | 27 | 7.98 | ... | 3.22 | 1.94 | 13.1 | | |
| | arm 2 | −31 | 12 | 2.02 | 1.92 | ... | ... | 3.9 | arms 25.5 | arms 26 |
| | arm 1 | −55 | 20 | 3.57 | 3.55 | 1.41 | ... | 8.5 | | |
| | arm 3 | −5bl | 18 | 3.37 | 4.45 | 2.05 | ... | 9.9 | arms 25.3 | arms 25 |
| NHS 21 | arm 2 | −35 | 12 | 1.08 | 1.41 | 0.56 | ... | 3.1 | | |
| | arm 1 | −51 | 27 | 3.78 | 4.81 | 2.77 | 0.89 | 12.3 | CMZ | CMZ - |
| | arm 3 | −6bl | 23 | 2.19 | 3.29 | 1.33 | ... | 6.8 | arms 27.3 | arms 27 |
| NHS 22 | arm 2 | −38 | 13 | 0.99 | 0.98 | 0.68 | ... | 2.7 | | |
| | arm 1 | −51 | 20 | 5.37 | 6.88 | 4.74 | 0.84 | 17.8 | CMZ - | CMZ - |
| | CMZ | +2 | 12 | 0.72 | 1.67 | 1.61 | ... | 4.0 | CMZ 7.1 | CMZ 7 |
| | arm 3 | −6 | 16 | 1.49 | 2.86 | 1.25 | ... | 5.6 | | |
| NHS 42 | arm 2 | −34 | 19 | 2.72 | 4.20 | 1.53 | ... | 8.5 | arms 25.4 | arms 25 |
| | arm 1 | −51 | 24 | 3.30 | 5.47 | 2.49 | ... | 11.3 | | |
| | CMZ | −86 | 25 | 0.82 | 1.38 | 0.88 | ... | 3.1 | | |
| | arm 3 | −6bl | 23 | 2.51 | 3.66 | 0.88 | ... | 7.1 | | |
| NHS 25 | arm 2 | −33 | 13 | 1.74 | 2.46 | 0.68 | ... | 4.9 | arms 25.0 | arms 25 |
| | arm 1 | −54 | 25 | 4.41 | 6.41 | 3.06 | ... | 13.9 | | |
| | arm 3 | −4 | 21 | 2.39 | 2.90 | 1.89 | ... | 7.2 | | |
| $\eta$ | arm 2 | −33 | 12 | 2.00 | 2.46 | 0.68 | ... | 5.1 | arms 23.9 | arms 24 |

**Table 3**
(Continued)

| Star | Location | $v$ (km s$^{-1}$) | $\Delta v$ (km s$^{-1}$) | $N(0)$ ($10^{17}$ cm$^{-2}$) | $N(1)$ ($10^{17}$ cm$^{-2}$) | $N(2)$ ($10^{17}$ cm$^{-2}$) | $N(3)$ ($10^{17}$ cm$^{-2}$) | $N(\mathrm{CO})_{\mathrm{cloud}}$ ($10^{17}$ cm$^{-2}$) | $N(\mathrm{CO})_{\mathrm{total}}$ ($10^{17}$ cm$^{-2}$) | $A_V$ (mag) |
|---|---|---|---|---|---|---|---|---|---|---|
| | arm 1 | −50 | 25 | 4.02 | 5.65 | 1.93 | ⋯ | 11.6 | | |
| | CMZ | −108 | 18 | 0.60 | 1.38 | 0.96 | ⋯ | 2.9 | CMZ 2.9 | CMZ 3 |
| | arm 3 | −8bl | 20 | 2.34 | 2.61 | 1.01 | ⋯ | 6.0 | | |
| | arm 2 | −36 | 16 | 1.83 | 2.32 | 0.68 | ⋯ | 4.8 | arms 21.5 | arms 22 |
| GCS 3−2 | arm 1 | 54 | 20 | 3.16 | 5.43 | 2.09 | ⋯ | 10.7 | | |
| | CMZ | −66 | 12 | 0.46 | 0.58 | 0.56 | ⋯ | 1.6 | | |
| | CMZ | −85 | 13 | 0.67 | 1.09 | 1.09 | ⋯ | 2.9 | CMZ 6.6 | CMZ 7 |
| | CMZ | −98 | 12 | 0.48 | 0.91 | 0.68 | ⋯ | 2.1 | | |
| | arm 3 | −9bl | 29 | 3.37 | 2.86 | 1.69 | ⋯ | 7.9 | | |
| GCS 4 | arm 2 | −34 | 19 | 2.02 | 2.32 | 0.84 | ⋯ | 5.2 | arms 25.6 | arms 6 |
| | arm 1 | −54 | 21 | 3.69 | 5.76 | 3.06 | ⋯ | 12.5 | | |
| | CMZ | −66 | 10 | 0.55 | 1.38 | 0.80 | ⋯ | 2.7 | CMZ 2.7 | CMZ 3 |
| | CMZ | +13 | 13 | 0.34 | 0.65 | 0.84 | ⋯ | 1.8 | | |
| | arm 3 | 0 | 12 | 0.75 | 1.41 | 0.60 | ⋯ | 2.8 | | |
| | arm 3 | −11 | 9 | 1.25 | 0.94 | 0.36 | ⋯ | 2.6 | arms 28.9 | arms 29 |
| FMM 362 | arm 2 | −34 | 13 | 2.27 | 1.88 | 1.45 | ⋯ | 5.6 | | |
| | arm 1 | −53 | 19 | 5.40 | 7.28 | 4.86 | 0.34 | 17.9 | | |
| | CMZ | −70 | 10 | 0.60 | 0.80 | 1.53 | 0.25 | 3.2 | CMZ 10.9 | CMZ 11 |
| | CMZ | −93bl | 28 | 1.54 | 2.14 | 2.01 | 0.25 | 5.9 | | |
| | arm 3 | −6 | 16 | 2.22 | 3.37 | 2.57 | ⋯ | 8.2 | | |
| $\theta$ | arm 2 | −38 | 17 | 4.53 | 8.18 | 4.54 | 1.60 | 18.9 | arms 55.0 | arms 55 |
| | arm 1 | −52 | 18 | 6.89 | 11.73 | 7.56 | 1.69 | 27.9 | | |
| | CMZ | −101 | 14 | 0.72 | 1.01 | ⋯ | ⋯ | 1.7 | CMZ 1.7 | CMZ 1.7 |

**Note.** The LSR velocities $v$, velocity widths $\Delta v$, level column densities $N(J)$, total column densities $N(\mathrm{CO})_{\mathrm{cloud}}$ for each cloud, total arm column densities $N(\mathrm{CO})_{\mathrm{arm}}$, total CMZ column densities $N(\mathrm{CO})_{\mathrm{CMZ}}$, and estimated total visual extinction of arms $(A_V)_{\mathrm{arm}}$ and of the CMZ $(A_V)_{\mathrm{CMZ}}$ are given. "bl" denotes blended components.

they are present, their spectral profiles vary drastically with the Galactic coordinates as can be seen by comparing the H$_3^+$ spectrum of $\alpha$ with the H$_3^+$ spectra of nearby stars $\alpha+$ and $\beta$ (Figure 7). The source-to-source variations must be due to the peculiar morphology and dynamics of the dense clouds in this part of the CMZ and are not of interest in this paper. The third deep absorption at −60 km s$^{-1}$ is caused by H$_3^+$ in dense clouds of the foreground 3 kpc spiral arm. Dense clouds in the other two spiral arms, near −30 and 0 km s$^{-1}$, do not exist on this sight line.

The deep blend of absorptions by H$_3^+$ at 0 and +8 km s$^{-1}$ and the weaker features at −27 and −75 km s$^{-1}$ are also due to H$_3^+$ in diffuse molecular clouds. It is possible that some of the H$_3^+$ absorption near zero velocity is due to cold foreground diffuse gas, as such gas, which could be associated with the Local Arm, does not produce detectable CO absorption. However, the presence of strong absorption in the $R(3, 3)^l$ line of H$_3^+$ at these low velocities (Figure 7, top left panel) implies that much, if not all, of the absorbing H$_3^+$ is both diffuse and warm and therefore located within the CMZ.

Although the near-zero radial velocity of warm H$_3^+$ on this sight line near the western edge of the CMZ could be due to the absorbing gas traveling at low speed, in view of the rapid radial outward motions observed closer to the center of the CMZ, it is much more natural to interpret it as the same rapid gas motion (velocities up to 150 km s$^{-1}$) as seen toward the center, but perpendicular to the line of sight. In other words, the overall motion of the warm diffuse gas is most naturally interpreted as a roughly radial expansion originating near the center of the CMZ. This low radial velocity absorption by warm diffuse gas

is also seen in the other stars located near the western edge of the CMZ, $\alpha+$ and $\beta$ (Figure 7), again demonstrating the large dimension of the warm, diffuse gas. We interpret the variation of their H$_3^+$ column densities from sight line to sight line as due to variations of these stars' depths in the CMZ. The weaker absorption at −27 km s$^{-1}$ and a doublet centered at −75 km s$^{-1}$, which are not accompanied by CO absorptions, are also due to H$_3^+$ in diffuse clouds. We interpret them as due to small stray clouds.

### 4.2.3. 17470898-2829561($\iota$): The Only Sight Line with CO Dominated by CMZ Absorption

This star, 84.5 pc east of Sgr A$^*$ (about 60% of the distance from Sgr A$^*$ to the eastern edge of the CMZ) and 1.8 pc below the Galactic plane, is located between Sgr B1 and B2, a region of dense giant molecular clouds undergoing massive star formation. This is the only sight line in our survey whose CO absorption is dominated by high-dispersion CMZ gas (Figure 5 left). The H$_3^+$ absorption component at −98 km s$^{-1}$ is the only clear feature not seen in CO absorption, and thus it is the only absorption definitely arising in diffuse gas. The $R(3, 3)^l$ spectrum (Figure 7) also has a strong absorption at this velocity, further attesting to this H$_3^+$ absorption component arising in the warm diffuse gas of the CMZ. The observed H$_3^+$ column density in the −98 km s$^{-1}$ component indicates that this star is embedded in the CMZ at least a few tens of parsec from the front of the expanding diffuse gas. The remainder of the H$_3^+$ $R(1, 1)^l$ absorption, whose depth is approximately 4% continuously from $v \sim −90$ to +100 km s$^{-1}$, is accompanied by CO absorption and hence arises in dense gas of the giant

molecular cloud complex. As seen in the figure, the $v = 2 \leftarrow 0$ absorption lines of CO toward this star are strong out to the most highly excited line shown ($R$(3)), unlike the CO spectra toward other stars in which the $R$(3) absorption is absent or very weak (see Figure 6). Indeed, significant absorption is present in J17470898 ($\iota$) out to $R$(5). This indicates high kinetic temperatures in this dense molecular cloud complex. Apart from the $-98 \, \mathrm{km \, s^{-1}}$ feature, analysis of the complex spectra of this star is beyond the scope of this paper.

### 4.3. Column Densities of Dense Gas in the Foreground and CMZ

Although the large beam size of single-dish radio observations HPBW $\sim 16''$ (0.62 pc) (Oka et al. 1998b) and the highly saturated $J = 1 \rightarrow 0$ CO emission found toward the CMZ might give the impression that the CMZ is packed with dense clouds, pencil-beam spectroscopy of lines of the first vibrational overtone of CO toward our survey stars tells quite a different story. As seen in Figure 6, in nine stars located from 140 pc west to 85 pc east of Sgr A$^*$, the vast majority of spectra show very little absorption by CO, apart from features associated with foreground spiral arms, and hence very little dense gas resident in the CMZ on their sight lines. All of these stars are deeply embedded in the CMZ as demonstrated by the observed $H_3^+$ total column densities of $N(H_3^+) > 2 \times 10^{15}$ cm$^{-2}$ and in many cases by their inferred locations relative to the Central Cluster. The only sight lines where prominent absorption by CO within the CMZ is observed are toward several stars near Sgr E on the western extremity of the CMZ (e.g., J17432173$-$2951430 ($\alpha$), Figure 6, top left), toward J17470898$-$2829561 ($\iota$) in the Sgr B molecular cloud complex (Figure 6, bottom right), and toward several stars in the Central Cluster.

The CO column densities for each velocity component toward 18 stars are given in Table 3. They were calculated using $N(CO)_{level} = (3hc)/(8\pi^3\lambda) W_\lambda/|\mu|^2$ from measured equivalent widths $W_\lambda = \int [\Delta I(\lambda)/I(\lambda)] d\lambda$ of the $R$(0), $R$(1), $R$(2), and $R$(3) absorption lines for levels $J = 0$, 1, 2, and 3, respectively, and the transition strength $|\mu|^2 = (J+1)/(2J+1)\langle 2|\mu|0\rangle^2$ with the transition dipole moment $\langle 2|\mu|0\rangle = 0.006518$ D (Zou & Varanasi 2002). It should be noted that these values are much more accurate and reliable than the CO column densities measured from radio CO emission because (1) the upper level of a transition is not populated, (2) the absorption is not saturated because of the small transition dipole moment, and, most significantly, (3) the large velocity gradient method (Goldreich & Kwan 1974) used to overcome the complication of radiation trapping need not be invoked to determine the column density. As discussed in the previous section, the sight line toward J17470898$-$2829561($\iota$) is unique, with multiple blended velocity components, which we do not attempt to separate; we list it separately in Table 4.

#### 4.3.1. CO in the Three Spiral Arms

As described earlier, sight lines toward the GC cross three spiral arms, Norma, Scutum, and Sagittarius (e.g., Figure 2 of Vallée 2016), which leave their fingerprints on nearly all of the spectra of $H_3^+$ and CO presented in this paper. Staying out of the controversy regarding the detailed structure of spiral arms, and whether or not the Norma arm and the 3 kpc arm are identical, etc. (e.g., Vallée 2014), we refer to them hereafter as the 3 kpc arm

**Table 4**
CO Column Densities toward $\iota$ in the CMZ

| $N(0)$ | $N(1)$ | $N(2)$ | $N(3)$ | $N(4)$ | $N(5)$ | $N(CO)_{total}$ | $A_V$ |
|---|---|---|---|---|---|---|---|
| 44.3 | 75.7 | 68.7 | 54.9 | 19.9 | 6.4 | 270 | 270 |

**Note.** Same as in Table 3, but for the star $\iota$ toward Sgr B, which has a complicated velocity profile with high velocity dispersion; only total CO column densities are given.

(Rougoor & Oort 1960) (arm 1), the 4.5 kpc arm (Menon & Ciotti 1970) (arm 2), and the Local Arm (arm 3). Deep absorption due to CO in the 3 kpc arm is observed toward all nine stars in Figure 6 and 18 stars listed in Table 3 and is the strongest of the three spiral arm absorptions toward most stars. When this absorption feature is not observed toward a star, we regard the star to be in front of the 3 kpc arm. The absorption velocity due to this arm varies from $-62 \, \mathrm{km \, s^{-1}}$ on the western edge of the CMZ to $-50 \, \mathrm{km \, s^{-1}}$ on the eastern edge. Such radial velocity gradients in Galactic longitude are well known and are used for studies of kinematics and dynamics of the gas in the GC region (e.g., Sofue 2006). Weaker absorption lines of CO in the 4.5 kpc arm with velocities from $-32$ (west) to $-38 \, \mathrm{km \, s^{-1}}$ (east) are observed toward all 20 stars except two stars in the west end, J17432173$-$2951430 ($\alpha$) and J17432988$-$2950074 ($\beta$). We interpret this as due to incidental absence of dense clouds in that arm on those sight lines. Finally, deep and relatively broad absorption at $\sim 0 \, \mathrm{km \, s^{-1}}$ is due to CO in the pileup of local gas closest to the Sun. This absorption feature is observed toward all but one star, J17432173$-$2951430 ($\alpha$), whose sight line must also happen to avoid local dense molecular gas.

The total CO column densities in the three spiral arms, $N(CO)_{arms}$, are also listed in Table 3. Fourteen of the 18 sight lines have column densities in the range $(1.04-2.89) \times 10^{18}$ cm$^{-2}$. Four stars, the aforementioned J17470898$-$2829561 ($\iota$), GCIRS 21, GCIRS 16NE, and J17473219$-$2844546 ($\theta$), have much higher values. The higher column densities toward GCIRS 21 and GCIRS 16NE are due to exceptionally high values in the $\sim 0 \, \mathrm{km \, s^{-1}}$ component, where contributions from the Local Arm and dense clouds in the CMZ overlap and cannot be separated. The high value toward Star $\theta$ is due to an exceptionally high column density of dense molecular gas in the 3 kpc arm on its sight line. Assuming the ratio of $H_2$ to CO number densities to be $10^4$, the 14 "normal" values of $N(CO)_{arms}$ correspond to $H_2$ column densities, $N(H_2)_{arms} \sim (1-3) \times 10^{22}$ cm$^{-2}$, which correspond to $A_V \sim 10-30$ mag, if the standard conversion factor from hydrogen column density to color excess $E(B-V)$ (Bohlin et al. 1978) and $A_V/E(B-V)$ ratio of $\sim 3$ (both caused by interstellar dust) are used. The values of $A_V$ for the arms are also given in Table 3. The value of the total CO column density $N(CO)$ in the units of $10^{17}$ cm$^{-2}$ and the visual extinction $A_V$ in magnitudes happen to be nearly identical using this conversion.

A detailed analysis of CO in the spiral arms is beyond the scope of this paper and will be published in a separate paper.

#### 4.3.2. CO in the CMZ

We have already demonstrated that most of our survey stars are embedded approximately as deeply in the CMZ as the stars in the Central Cluster. It is thus apparent, from both Figure 6 and Table 3, that on most observed sight lines the CO column densities in the front half of the CMZ are far less than the

column densities in the foreground spiral arms. Out of the 17 stars listed in Table 3, the values of $N(CO)_{CMZ}$ are somewhat higher than $N(CO)_{arms}$ only for three stars, $\alpha$ in the Sgr E complex and GCIRS 3 and GCIRS 1W in the Sgr A complex. The visual extinctions due to dense clouds in the CMZ are $A_V \sim$ 20–30 mag toward the three stars and $\sim$300 mag for star $\iota$ listed in Table 4. For the remaining 14 stars in Table 3, $A_V$ is very much smaller and a far cry from the mean value $A_V \sim$ 500 mag obtained assuming that dense ($n \geqslant 10^4\,cm^{-3}$) gas has a volume filling factor of $f \geqslant 0.1$ in the CMZ. In calculating these extinctions due to dense gas in the CMZ, which are based on our CO measurements, we have assumed that the dust-to-gas ratio scales with the carbon abundance and thus compensates for the higher than solar value of [C/H] in the CMZ (see Appendix A.2). This assumption is crudely consistent with the dependency of dust-to-gas ratio on galactocentric radius found by Giannetti et al. (2017).

Cotera et al. (2000) and Schultheis et al. (2009) used infrared photometry of stars in the GC to derive total visual extinctions ( i.e., due to dust in both dense and diffuse gas). The former authors, who relied on 2MASS values, found total extinctions in the range 25–40 mag for stars in the CMZ, while the latter authors, who used both 2MASS and longer-wavelength *Spitzer* IRAC photometry, which detects more highly obscured stars than 2MASS, determined somewhat higher values. To compare our values with theirs, we must add to the extinction that we derive owing to dense clouds in the CMZ and the spiral arms the extinction by dust in diffuse gas along the entire sight line. The extinction due to diffuse gas on sight lines to objects near Sgr A$^*$ has been roughly estimated by Whittet et al. (1997) to be 20 visual magnitudes, by subtracting their estimate of 10 visual magnitudes of extinction due to dust in dense clouds, from the canonical 30 mag of total extinction. Note, however, that almost all of our estimates of visual extinction by dense clouds on such sight lines are much higher than 10 mag (Table 3), suggesting that the extinction due to dust in diffuse gas may be significantly less than 20 mag, or perhaps that the dust-to-gas ratio in the CMZ derived from $N(CO)$ does not scale with the carbon abundance. Adding 10–20 mag to the sum of the values of $A_V$ due to dense clouds in Table 3 gives total visual extinctions of 20–70 mag for most of the sight lines that we observed, in general agreement with the ranges reported by Cotera et al. and Schultheis et al.

The case of J17470898−2829561 ($\iota$), where the visual extinction based on the column density of CO is $\sim$300 mag, poses a severe problem. The use of a standard extinction dependency on wavelength (e.g., $\propto \lambda^{-1.7}$) or the more recently derived $\lambda^{-2.11}$ in the region of the Central Cluster (Fritz et al. 2011) leads to absurdly high values for the extinction in the $K$ and $L'$ bands ($\sim$24 and $\sim$10 mag, respectively, for the standard dependency and $\sim$13 and $\sim$4 mag, respectively, for the Fritz et al. dependency), given the apparent brightness of this star ($K_{2MASS} = 10.4$ mag, $L_{IRAC} = 6.6$ mag). Either the dust-to-gas ratio in this portion of the Sgr B cloud is vastly lower than predicted from the value of [C/H], or the extinction falloff with increasing wavelength on this sight line is considerably steeper than the above extinction curves. It is unclear whether either of these possibilities is manifested in dense clouds elsewhere in the CMZ; if so, the effect would be to greatly lower the extinctions (reducing the impact of the selection effect discussed earlier). Given the modest dense cloud extinctions found on the other sight lines in the CMZ, neither of these

possibilities affects the major conclusions of this paper. The properties of the interstellar gas and dust toward star $\iota$ will be presented and discussed in more detail in a forthcoming paper (T. R. Geballe et al. 2019, in preparation).

### 4.4. $H_3^+$ in the CMZ

As discussed in Section 4.1 and shown in Table 2, column densities of warm $H_3^+$ on the order of $3 \times 10^{15}\,cm^{-2}$ are observed toward stars deeply embedded in the CMZ. In the following sections, we describe how the individual column densities in the para-(1, 1) ground level, the ortho-(1, 0) level, the unstable para-(2, 2) level, and the metastable ortho-(3, 3) level provide information on the temperature and density of the gas in which $H_3^+$ is located.

The observed (1, 1) and (1, 0) column densities include contributions from the CMZ and the foreground spiral arms. Only in the high-resolution spectra obtained with UKIRT/ CGS4, Gemini South/Phoenix, and VLT/CRIRES can these contributions be separated (see Figure 4 of Oka et al. 2005). On the other hand, the column densities in the (2, 2) and (3, 3) levels come entirely from the CMZ and can be measured with all of the spectrographs that we have used. Figure 7 shows the $R(1, 1)^l$ (upper traces) and $R(3, 3)^l$ (lower traces) absorption spectra toward nine stars from 139 pc west of Sgr A$^*$ ($\alpha$) to 116 pc east ($\lambda-$). The column densities contributed by the CMZ and individual spiral arms, where separable, are given in Table 5. For the $R(1, 1)^l$ absorption different velocity components are separately measured using high-resolution ($R \geqslant 40{,}000$) spectrometers of CGS 4 at UKIRT, Phoenix at the Gemini South Observatory, and CRIRES at VLT, in order to discriminate between the $H_3^+$ absorptions in the three foreground spiral arms. See Figure 4 of Oka et al. (2005). On the other hand, for the $R(3, 3)^l$ absorption, which does not exist in the low-temperature spiral arms, low-resolution observations suffice.

#### 4.4.1. $H_3^+$ in the Metastable (3, 3) Level: Evidence of High Temperature

As indicated in Section 1.6, the ratio of $H_3^+$ column densities in the metastable (3, 3) and the ground (1, 1) levels, separated in energy by 361 K, is a sensitive measure of the temperature in diffuse warm gas. Unlike collisions between $NH_3$ and $H_2$, which are physical and do not convert ortho and para species (Oka 1973), collisions between $H_3^+$ with $H_2$ are chemical, in that protons are exchanged between $H_3^+$ and $H_2$ and connect the ortho (3, 3) level and the para (1, 1) level (Quack 1977; Uy et al. 1997; Oka 2004). Since ortho-to-para conversion occurs rapidly, the temperature of the gas can be approximately determined from the excitation temperature $T_{ex}(3, 3/1, 1)$, which is calculated from

$$\frac{N(3, 3)}{N(1, 1)} = \frac{14}{3} \exp\left(-\frac{361\,K}{T_{ex}(3, 3/1, 1)}\right). \quad (4)$$

The actual kinetic temperature is higher than the excitation temperature because the rapid symmetry-breaking $\Delta k = \pm 3$ spontaneous emissions cool the $H_3^+$. A more accurate determination of temperature taking into account this effect will be discussed in Section 5.1.

Toward three stars, J17432173−2951430 ($\alpha$), J17432823 −2952159 ($\alpha+$), and J17432988−2950074 ($\beta$), located near Sgr E and the western edge of the CMZ ($G_{lon} = -1°.0463, -1°.0417, -1°.0082$, respectively), the $R(3, 3)^l$

**Table 5**
Level Column Densities of $H_3^+$ from Spectroscopy at Gemin South, Gemini North, and UKIRT

| Star | $v_{\mathrm{LSR}}$ (km s$^{-1}$) | $\Delta v_{\mathrm{LSR}}$ (km s$^{-1}$) | $N(J, K)$ (10$^{15}$ cm$^{-2}$) | | |
|---|---|---|---|---|---|
| | | | (1, 1)[a] | (1, 1)[b] | (3, 3) |
| $\alpha$ | +2 | 35 | 0.55[c] | | 0.19[c,d] |
| | −26 | 17 | 0.06[c] | | |
| | −60 | 21 | 0.39 | | |
| | −77 | 19 | 0.12[c] | | |
| | −172 | 31 | 0.55 | | |
| | −200 | 23 | 0.28 | | |
| Total | | | 1.90 | 0.00 | 0.19[c] |
| $\alpha+$ | +51 | 30 | 0.28[c] | | |
| | +1 | 62 | 1.82[c] | | 0.86[c,d] |
| | −58 | 27 | 0.48 | | |
| | −167 | 25 | 0.32 | | |
| Total | | | 2.90 | 0.00 | 0.86[c,d] |
| $\beta$ | +2 | 35 | 0.58[c] | | 0.40[c,d] |
| | −27 | 16 | 0.09 | | |
| | −57 | 23 | 0.30 | | |
| | −143 | 23 | 0.22 | | |
| | −176 | 41 | 0.43 | | |
| Total | | | 1.62 | 0.00 | 0.40[c,d] |
| $\gamma$ | −4 | 38 | 0.72 | | |
| | −30 | 16 | 0.20 | | |
| | −56 | 22 | 0.37 | | |
| | −136 | 60 | 1.16[c] | | 0.64[c] |
| Total | | | 2.44 | | 0.64[c] |
| $\delta$ | +0 | 10 | 0.05 | | |
| | −8 | 18 | 0.19 | | |
| | −29 | 20 | 0.33 | | |
| | −54 | 28 | 0.45 | | |
| | −126 | 30 | 0.19 | | |
| | −155 | 18 | 0.06 | | |
| Total | | | 1.27 | 0.85[c] | |
| NHS 21 | −3 | 30 | 0.34 | | |
| | −30 | 24 | 0.14 | | |
| | −50 | 24 | 0.32 | | |
| | −125 | 50 | 0.45[c] | | 0.17[c] |
| Total | | | 1.25 | | |
| NHS 22 | −9 | 29 | 0.35 | | |
| | −38 | 17 | 0.17 | | |
| | −57 | 22 | 0.43 | | |
| | −83 | 24 | 0.09 | | |
| Total | | | 1.04 | 0.55[c] | |
| NHS 42 | −3 | 30 | 0.14 | | |
| | −31 | 24 | 0.19 | | |
| | −50 | 28 | 0.25 | | |
| | −78 | 29 | 0.13 | | |
| | −113bl? | 29 | 0.11 | | |
| | −134 | 17 | 0.06 | | |
| Total | | | 1.16 | 1.24[c] | |
| NHS 25 | +30 | 10 | 0.04 | | |
| | +17 | 9 | 0.05 | | |
| | −2bl? | 25 | 0.27 | | |
| | −32 | 18 | 0.14 | | |
| | −52 | 26 | 0.31 | | |
| | −77 | 14 | 0.05 | | |
| | −86 | 10 | 0.03 | | |
| | −100 | 13 | 0.05 | | |
| | −125 | 23 | 0.12 | | |
| | −140? | 8 | 0.03 | | |
| Total | | | 1.09 | 1.43[c] | |
| GCS 3-2 | +17 | 15 | 0.10 | | |
| | +2 | 13 | 0.14 | | |
| | −6 | 15 | 0.16 | | |
| | −32 | 18 | 0.21 | | |
| | −52 | 34 | 0.43 | | |
| | −97 | 19 | 0.08 | | |
| | −123 | 12 | 0.03 | | |
| Total | | | 1.15 | 1.45[c,e] | 0.70[c,e] |
| FMM 362 | −1 | 48 | 0.55 | | |
| | −32 | 20 | 0.20 | | |
| | −52 | 26 | 0.41 | | |
| | −87 | 28 | 0.18 | | |
| Total | | | 1.34 | 1.13[c] | |
| $\theta$ | −1 | 24 | 0.41 | | |
| | −32 | 10 | 0.14 | | |
| | −51 | 32 | 0.79 | | 0.36[c,f] |
| | −122 | 48 | 0.22 | | |
| Total | | | 1.56 | 1.24[c] | 0.95[c,d,f] |
| $\iota$ | +0 | 234 | 4.32 | 0.00 | 1.68[c,d,f] |
| $\lambda-$ | −19 | 89 | 1.27[f,g] | | 0.43[c,d,f] |
| $\lambda-+$ | +150? | 86 | 0.61[f] | | |
| | +50? | 46 | 0.15 | | |
| | −30bl | 133 | 2.19[c,f,g] | | |
| Total | | | 2.94 | | |

**Notes.** Observed peak velocities, absorption widths, and $H_3^+$ column densities for the ground level for each peak, for the trough, and $N(3, 3)$ for the metastable level. Most lines have been observed in the Gemini South Observatory using the Phoenix spectrometer, unless otherwise noted.
[a] Sharp absorption lines with peaks.
[b] Trough absorption component.
[c] Isolated diffuse gas.
[d] $N(3, 3)$ are contaminated by atmospheric water absorption.
[e] Observed at the UKIRT using the CGS4 spectrometer (Oka et al. 2005).
[f] Observed at the Gemini North Observatory using the GNIRS spectrometer.
[g] $N(1, 1)$ values are blended with the absorptions in spiral arms.

absorption occurs near 0 km s$^{-1}$ radial velocity (Figure 7, top three spectra). As discussed in Section 4.2.2 for the case of the $R(1, 1)^l$ line, the radial velocity at these locations is most simply interpreted as gas expanding perpendicular to the line of sight.

Toward the star J17444083−2926550 ($\gamma$) ($G_{\mathrm{lon}} = -0°.5442$) near the Sgr C complex the $R(3, 3)^l$ spectrum (Figure 7, middle left) shows a prominent absorption extending from −170 to −110 km s$^{-1}$ centered at −136 km s$^{-1}$. As the depth of this star in the CMZ is unknown, it is not clear whether this rather narrow blueshifted absorption range and lack of a trough is due to this star's shallow depth within the CMZ or if it is more deeply embedded but its sight line somehow avoids gas at lower blueshifted velocities.

For the three stars in the central 30 pc, GCIRS 1W ($G_{\mathrm{lon}} = -0°.0553$), NHS 42 ($G_{\mathrm{lon}} = 0°.1479$), and GCS 3-2 ($G_{\mathrm{lon}} = 0°.1635$), all deeply embedded in the CMZ, the $R(3, 3)^l$ spectra show a broad absorption feature extending from

$\sim -160 \, \text{km s}^{-1}$ all the way to $\sim 0 \, \text{km s}^{-1}$ (Figure 7, middle center and right, and bottom left panels). In Section 5 we show that this is best interpreted as originating in a large volume of warm gas occupying most of the sight line within the front half of the CMZ. This absorption feature is also seen in the $R(1, 1)^l$ line as a "trough" superimposed on the sharp absorption features due to the foreground spiral arms (e.g., Figures 3 and 4; see also Figure 4 of Oka et al. 2005).

The sight line toward J17470898−2829561 ($\iota$) ($G_{\text{lon}} = 0°.5477$, Figure 7, bottom middle panel), located in the direction of the Sgr B complex, is as unique in its $H_3^+$ spectra as it is in its CO spectra discussed previously (Section 4.2.3). The broad $R(1, 1)^l$ and $R(3, 3)^l$ absorption features centered at $-98 \, \text{km s}^{-1}$ represent the only clear diffuse cloud component (as there is no CO absorption feature at this velocity; see Figure 6). The deep, broad, and structured $R(1, 1)^l$ and $R(3, 3)^l$ profiles from $\sim -70$ to $+100 \, \text{km s}^{-1}$ are produced by $H_3^+$ in a conglomeration of warm dense clouds on the line of sight. Although this gas is denser than the diffuse gas seen on all other observed sight lines in the CMZ, it is not very dense since the $R(2, 2)^l$ absorption (discussed in the next section) is not as strong as it would be if the (2, 2) level were populated in LTE at the temperature derived from Equation (4). The absorption profiles of $H_3^+$ and CO toward this star are discussed in some detail by Goto et al. (2011) and are beyond the scope of this paper.

The star J17482472−2824313 ($\lambda-$) ($G_{\text{lon}} = 0°.7745$; Figure 7, bottom right) is the easternmost star (116 pc from Sgr A*) for which both the $R(1, 1)^l$ and $R(3, 3)^l$ line profiles have been observed. In both lines the only velocity component present is centered near $-20 \, \text{km s}^{-1}$. We interpret this rather low velocity in the same way as we did for the westernmost stars, $\alpha$, $\alpha+$, and $\beta$, in Section 4.2.2, as a radial expansion nearly perpendicular to the line of sight.

### 4.4.2. $H_3^+$ in the Unstable (2, 2) Level: Evidence of Low Density

As discussed in Section 1.6, the column density of $H_3^+$ in the unstable (2, 2) level provides a good measure of the gas density. In Figure 8, $R(2, 2)^l$ spectra toward nine stars observed by the IRCS spectrometer on the Subaru Telescope are compared with the $R(1, 1)^l$ spectra toward those stars. Except for the special case of the star J17470898−2829561 ($\iota$) in the Sgr B complex, absorption in the $R(2, 2)^l$ line is totally absent, implying that in general the density of the diffuse gas that we have observed in the CMZ is considerably less than the critical density, $200 \, \text{cm}^{-3}$.

### 4.4.3. Observed $H_3^+$ Level Column Densities

In addition to column densities of the (1, 1), (3, 3), and (2, 2) levels, which are needed to determine temperature and density, the column density of the (1, 0) level is needed to determine the total $H_3^+$ column density $N(H_3^+)_{\text{total}}$. For this purpose we observed the $Q(1, 0)$ transition (Goto et al. 2002) or $R(1, 0)$ transition, which appears as a doublet with the $R(1, 1)^u$ transition (Geballe & Oka 1996). For the doublet, which is blended in the CMZ owing to the wide velocity profiles of each line, we determine $N(1, 1) + N(1, 0)$ and calculate $N(1, 0)$ by subtracting $N(1, 1)$ determined from the $R(1, 1)^l$ line. The IRCS spectrometer of the Subaru Telescope is especially useful for this because of its wide wavelength coverage. This procedure gives a value of $N(1, 0)/N(1, 1)$ on the order of $\sim 0.5$. A

detailed thermalization analysis shows that the excitation temperature $T_{\text{ex}}(1, 0/1, 1)$, defined by

$$\frac{N(1, 0)}{N(1, 1)} = 2 \exp\left(-\frac{32.9 \, \text{K}}{T_{\text{ex}}(1, 0/1, 1)}\right), \tag{5}$$

is approximately 30 K (sometimes called the "spin temperature") and is a slowly varying function of the kinetic temperature for $T_k \sim 200 \, \text{K}$ and densities $n \sim 50 \, \text{cm}^{-3}$, as shown in Figure 6 of Oka & Epp (2004). We use $N(1, 0) = 0.7 N(1, 1)$ as estimated values. We believe that the errors introduced by this in calculating $N(H_3^+)_{\text{diffuse}}$ are less than 4%, well within the uncertainties in the measured column densities.

Finally, the level column densities of $H_3^+$ in diffuse gas $N(J, K)$ are summarized in Table 6, along with the total $H_3^+$ column densities $N(H_3^+)_{\text{diffuse}}$. The latter is calculated from $N(H_3^+)_{\text{diffuse}} = 1.1[N(1, 1) + N(3, 3) + N(1, 0)]$, where the 10% increase is allowed for populations of metastable levels higher than (3, 3), such as (4, 4), (5, 5), (6, 6), etc., which individually are not observable but will amount to 10% of the total as discussed in Figure 5 of Oka & Epp (2004). Such metastable levels are recently discussed by Smith et al. (2018). Table 6 also contains population ratios and information on temperature and density. We here list stars with relatively complete $H_3^+$ measurements, but we have observed many other stars with similar $N(J, K)$.

## 5. Analysis

### 5.1. Temperature and Density of the Diffuse Gas in the CMZ

As shown in Table 6, the observed $N(3, 3)/N(1, 1)$ ratios give excitation temperatures that average to $160 \pm 24 \, \text{K}$. When cooling due to symmetry-breaking spontaneous emission, discussed in Section 1.6, is taken into account in the rotational thermalization of $H_3^+$ (Oka & Epp 2004), the actual kinetic temperature $T_k$ of the diffuse gas is significantly higher than $T_{\text{ex}}(3, 3/1, 1)$. On the other hand, a low number density of the diffuse gas $n$ is suggested by the nondetection of absorption in the $R(2, 2)^l$ line, which sets an upper limit on $N(2, 2)$.

### 5.1.1. Determining $T_k$ and Setting Upper Limits on the Density

Figure 4 of Oka & Epp (2004) and Figure 6 of Oka et al. (2005) plot the ratios $N(3, 3)/N(1, 1)$ and $N(3, 3)/N(2, 2)$ as functions of kinetic temperature $T_k$ and number density $n$. Here we inverted the plots to generate ones in which $T_k$ and $n$ are shown as functions of $N(3, 3)/N(1, 1)$ and $N(3, 3)/N(2, 2)$ (as in Figure 4 of Goto et al. 2008). Using the observed values of $N(3, 3)/N(1, 1)$ and the observed lower limits to $N(3, 3)/N(2, 2)$, $T_k$ and $n$ are determined as shown in Figure 9. This gives $T_k = 140–230 \, \text{K}$ and $n < 20–650 \, \text{cm}^{-3}$, with higher temperatures generally associated with lower upper limits on density. The values of $T_k$ and upper limits to $n$ are listed in Table 6 for sight lines toward six stars from $\sim 140$ pc west to $\sim 120$ pc east of Sgr A*. Readers are referred to Figure 4 of Goto et al. (2008), where measurements had higher uncertainties but give similar density and temperature.

### 5.1.2. Comparison with the Meudon Analysis

While the treatment of thermalization by Oka & Epp (2004) (hereafter called the Chicago model) uses the Einstein coefficients calculated by Neale et al. (1996), which are

**Table 6**
Level Column Densities and Total Column Densities of $H_3^+$ in Diffuse Clouds and Temperature and Density of Diffuse Clouds

| Star | $N(1, 1)$ ($10^{15}$ cm$^{-2}$) | $N(3, 3)$ ($10^{15}$ cm$^{-2}$) | $N(1, 0)$[a] ($10^{15}$ cm$^{-2}$) | $N(2, 2)$[b] ($10^{15}$ cm$^{-2}$) | $N(H_3^+)_{diffuse}$[c] ($10^{15}$ cm$^{-2}$) | $N(3, 3)/N(1, 1)$ | $T_{ex}(3, 3/1, 1)$[d] (K) | $T_k$[e] (K) | $n$[f] (cm$^{-3}$) |
|---|---|---|---|---|---|---|---|---|---|
| $\alpha$ | 0.73 | 0.19[h] | 0.51 | <0.03 | 1.57 | 0.26 | 125 | 154 | <17 |
| $\alpha+$ | 2.10 | 0.86[h] | 1.47 | <0.29 | 4.84 | 0.41 | 148 | 182 | <58 |
| $\beta$ | 0.58 | 0.40[h] | 0.41 | … | 1.53 | 0.69 | 189 | … | … |
| $\gamma$ | 1.16 | 0.64 | 0.81 | <0.14 | 2.87 | 0.55 | 169 | 227 | <45 |
| $\delta$ | 0.85 | … | 0.60 | … | … | … | … | … | … |
| NHS 21 | 0.45 | 0.17 | 0.32 | <0.21 | 1.03 | 0.38 | 172 | 141 | <651 |
| NHS 22 | 0.55 | … | 0.39 | <0.29 | … | … | … | … | … |
| NHS 42 | 1.24 | 0.64 | 0.87 | <0.41 | 3.03 | 0.52 | 164 | 181 | <178 |
| NHS 25 | 1.43 | … | 1.00 | <0.33 | … | … | … | … | … |
| GCS 3-2 | 1.45 | 0.70 | 1.01 | <0.14 | 3.48 | 0.48 | 159 | 211 | <36 |
| FMM 362 | 1.13 | 0.47 | 0.79 | … | 2.63 | 0.35 | 138 | … | … |
| $\theta$ | 1.24 | 0.95[g] | 0.87 | … | 3.37 | 0.77 | 200 | … | … |
| $\lambda-$ | 1.27[g] | 0.43 | 0.89[g] | … | 2.85 | 0.34 | 138 | … | … |
| $\lambda-+$ | 2.94[g] | … | 2.16[g] | <0.30 | … | … | … | … | … |

**Notes.**
[a] Calculated from $N(1, 0) = 0.7 N(1, 1)$; see text.
[b] Upper limits are $1\sigma$.
[c] Sum of $N(1, 1)$, $N(3, 3)$, $N(1, 0)$ and multiplied by 1.1; see text.
[d] Excited temperature calculated from Equation (4).
[e] Kinetic temperature $T_k$ of diffuse clouds calculated in Section 5.1.1.
[f] Upper limits of densities $n = n(H) + n(H_2)$ of diffuse clouds calculated in Section 5.1.1.
[g] $N(1, 1)$ values include contributions from spiral arms.
[h] $N(3, 3)$ values may be compromised by atmospheric water absorption.

accurate perhaps to within 5%, it uses roughly estimated collision rate constants based only on the Boltzmannian principle of detailed balancing and their symmetric division (their Equations (1)–(3)). This treatment also ignores the nuclear spin selection rules in the $H_3^+$–$H_2$ collisions (Quack 1977; Oka 2004). A more detailed state-to-state calculation of collisional rate constants including the spin selection rules has since been given by Park & Light (2007a, 2007b) using a statistical method. A more recent paper by Gómez-Carrasco et al. (2012), which is based on the statistical treatment of Park and Light but uses the full potential energy surface of the $H_5^+$ complex (Aguado et al. 2010) and the quasi-classical trajectory method, is used in the Meudon model analysis of Le Petit et al. (2016).

A comparison between the Chicago model and the Meudon model calculations of the two-dimensional $N(3, 3)/N(1, 1)$ and $N(3, 3)/N(2, 2)$ plots in terms of $n$ and $T_k$ is given in the top and bottom panels, respectively, of Figure 10 of Le Petit et al. (2016). Their study indicates that the crudely estimated collision rates of the Chicago model provide the essential features of the Meudon model in the region of interest of $n$ and $T_k$ and that the difference between the two approaches is due mainly to a scaling factor for the number density $n$; the two diagrams agree approximately if the scale of the number density $n$ in the Chicago models is multiplied by a factor of $\sim 8$. This suggests that the rate constant for the $H_3^+$ $(2, 2) \rightarrow (1, 1)$ collision-induced transition used in the Chicago model is 8 times higher than in the Meudon model. Since the total collision rate constant is normalized approximately to the Langevin rate constant of $2 \times 10^{-9}$ cm$^{-3}$ in Equation (3) of Oka & Epp (2004), in Section 3F of Park & Light (2007a), and in Figure 7 of Gómez-Carrasco et al. (2012), the difference must be due to the quantum number dependence of the rate constant, which is not considered in the Chicago model. Whether a quantum number dependence as significant as that
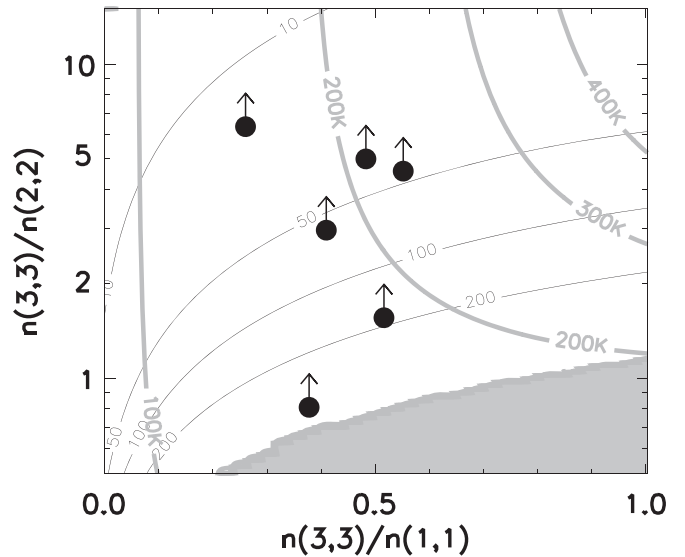


**Figure 9.** Temperature and density plotted in filled circles as functions of population ratios $n(3, 3)/n(1, 1)$ and $n(3, 3)/n(2, 2)$ by inverting the diagram of Oka & Epp (2004). The $n(3, 3)/n(2, 2)$ are all lower limits.

shown in Figure 7 of Gómez-Carrasco et al. exists for chemical collisions remains to be seen.

In spite of this difference, Le Petit et al. (2016) obtained a roughly similar, although somewhat higher, kinetic temperature range, $T_k = 212$–$505$ K, and a similar upper density limit, $n \leqslant 100$ cm$^{-3}$, to the Chicago model.

### 5.2. Cosmic-Ray $H_2$ Ionization Rate $\zeta$ and Dimension of Diffuse Clouds

In this section, we estimate the cosmic-ray ionization rate in the CMZ, using $T_k = 200$ K and $n \leqslant 100$ cm$^{-3}$ as representative

values for the diffuse interstellar medium there. We start from the original Chicago model, in which the quantum number dependence of collision rate and the nuclear spin selection rules are neglected; otherwise, the calculation becomes extremely complicated. For example, the quantum number dependences of rate constants themselves depend on temperature. Also, in order to use nuclear spin selection rules, it is necessary to include an additional parameter, the $H_2$ spin temperature.

### 5.2.1. Reconsidering the Relation between $\zeta_L$ and $N(H_3^+)$

In deriving the extremely simple Equation (3) relating the observed total $H_3^+$ column density $N(H_3^+)$ and the cosmic-ray $H_2$ ionization rate $\zeta$, Oka et al. (2005) neglected two effects: (1) the charge exchange reaction,

$$H_2^+ + H \rightarrow H_2 + H^+, \qquad (6)$$
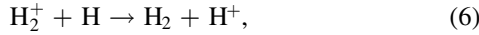
which is exothermic by $1.831\,eV$ and reduces the $H_3^+$ production rate if the fraction of molecular hydrogen $f(H_2)$ is significantly lower than unity; and (2) the production of free electrons by cosmic-ray ionization of $H_2$ and H, which increases the $H_3^+$ destruction rate if $\zeta$ is higher than $\sim 10^{-15}$ $s^{-1}$. (Previously, only electrons produced by vacuum ultraviolet first photoionization of C atoms had been included.) Both of these effects reduce $N(H_3^+)$ from values calculated from Equation (3), so that a higher value of $\zeta$ is required to obtain the same value of $N(H_3^+)$.

Values of $\zeta \sim (2\text{--}7) \times 10^{-15}\,s^{-1}$ obtained for the diffuse gas in the CMZ by Oka et al. (2005) and a slightly lower value estimated by Goto et al. (2008), using Equation (3), are more than 100 times higher than the early canonical values of $\sim 10^{-17}\,s^{-1}$ (Spitzer & Tomasko 1968; Webber 1998: see Dalgarno 2006 for a review). We did not consider $\zeta$ values higher orders of magnitude than $10^{-15}\,s^{-1}$ in those papers. In the meantime McCall et al. (2003) obtained a value of $\zeta$ on the order of $10^{-16}\,s^{-1}$ in the diffuse cloud toward $\zeta$ Persei, which led subsequently to the universally high $\zeta$ values on the order of $10^{-16}\,s^{-1}$ in diffuse clouds in the Galactic disk (Indriolo et al. 2007; Indriolo & McCall 2012).

Initially the high values of $\zeta$ in the GC were viewed with skepticism (e.g., Amo-Baladrón et al. 2011). However, soon after they were first reported, even higher values of $2 \times 10^{-14}$ $s^{-1}$ and $5 \times 10^{-13}\,s^{-1}$ were reported toward Sgr B1/B2 and Sgr C, respectively, from multiwavelength observations and analysis of $^{13}CO$ radio emission, X-rays, and $\gamma$-rays (Yusef-Zadeh et al. 2007). Yusef-Zadeh et al. (2013) further reported $\zeta = (1\text{--}10) \times 10^{-15}\,s^{-1}$ for a wider region of the central $300 \times 120\,pc$. Also, Indriolo et al. (2015) reported even higher values of $\zeta$, approaching $4 \times 10^{-14}\,s^{-1}$, for some velocity components of four far-infrared sources in the CMZ (M-0.13–0.08, M-0.02–0.07, Sgr B2(M), and Sgr B2(N)) using the extensive *Herschel* observations of $OH^+$, $H_2O^+$, and $H_3O^+$. Finally, Le Petit et al. (2016) reported values of $(1\text{--}11) \times 10^{-14}$ $s^{-1}$ from an analysis of the $H_3^+$ column densities reported by Oka et al. (2005) and Goto et al. (2008, 2011).

All of these results imply that to neglect the production of free electrons by ionization of H and $H_2$, assumed in deriving Equation (3), is not justified. Here we develop a formalism in which effects 1 and 2 mentioned at the start of this subsection are included. We use large-scale chemistry taking into account only hydrogenic species and electrons. The chemistry of helium, which may introduce uncertainties on the order of

10%, is neglected. We believe that our treatment is meaningful, even after the highly detailed analysis of Le Petit et al. (2016) using the Meudon code, in order to have an overall view, in particular because the Meudon results underestimate the observed $H_3^+$ column density of $3 \times 10^{15}\,cm^{-2}$ in obtaining their reported value of $\zeta = (1\text{--}11) \times 10^{-14}\,s^{-1}$ (see their Figure 1) for $n < 10^2\,cm^{-3}$, which is a reasonable choice of density as discussed above.

### 5.2.2. Reduction of $H_3^+$ Production Rate due to Charge Exchange Reaction

If $f(H_2)$ is significantly less than 1, the charge exchange reaction between $H_2^+$ and H, Equation (6), competes with the $H_3^+$ production reaction of Equation (1) and reduces the production rate of $H_3^+$ by

$$\Phi\left(f(H_2), \frac{k_6}{k_1}\right) = \left[1 + \frac{2k_6}{k_1}\left(\frac{1}{f(H_2)} - 1\right)\right]^{-1} \qquad (7)$$

(Indriolo & McCall 2012; Equation (6) of Oka 2013), where $k_1$ and $k_6$ are the rate constants of Equations (1) and (6), respectively. The reduction of the production rate due to dissociative recombination of $H_2^+$ is negligible due to the small number density of electrons. While $k_1$ in Equation (7) is a well-established Langevin rate constant $k_1 = (2.08 \pm 0.21) \times 10^{-9}$ $cm^3\,s^{-1}$ (Anicich & Huntress 1986), the value of $k_6$ is not well known. Based on the arguments given in Appendix A.4, we assume $k_6 = k_1/2$, partly because it gives a simple expression

$$\Phi = f(H_2). \qquad (8)$$

Compared with the previous $H_3^+$ production rate $\zeta f(H_2)$ used by Oka et al. (2005), in which $f(H_2)$ was assumed to be 1, the revised $H_3^+$ production rate $\zeta[f(H_2)]^2$ is approximately 3 times lower for the value $f(H_2) = 0.6$ reported by Le Petit et al. (2016) (see Appendix A.3).

### 5.2.3. Increase of $H_3^+$ Destruction Rate due to Ionization of $H_2$ and H

Considering only pure hydrogenic species and electrons, the production rate of electrons from $H_2$ and H due to cosmic-ray ionization is

$$\left(\frac{dn_e}{dt}\right)_{prod} = \zeta n(H_2) + \zeta_H n(H) \sim \frac{\zeta n_H}{2}, \qquad (9)$$

where $\zeta_H \sim \zeta/2$ (Glassgold & Langer 1974; Rudd et al. 1985; Dalgarno 2006) is the ionization rate of H and $n_H = 2n(H_2) + n(H)$ is the total number of H. The destruction rate of free electrons is

$$\left(\frac{dn_e}{dt}\right)_{dest} = [k_e n(H_3^+) + k_r n(H^+)]n_e^*, \qquad (10)$$

where $n_e^*$ is the number density of electrons produced from cosmic-ray ionization of $H_2$ and H, and $k_r$ is the radiative recombination rate constant for $H^+$. The destruction of electrons due to dissociative recombination of $H_2^+$ is negligible because, unlike $H_3^+$ and $H^+$, $H_2^+$ is rapidly destroyed by both $H_2$ and H and thus has an extremely small number density. While the production rates of $H_3^+$ and $H^+$ are comparable, their destruction rates are widely different because the dissociative recombination rate constant,

$k_e \sim 10^{-7} \, \mathrm{cm^3 \, s^{-1}}$ (Appendix A.1), is more than 4 orders of magnitude higher than the radiative recombination rate constant $k_r \sim 5 \times 10^{-12} \, \mathrm{cm^3 \, s^{-1}}$ (Appendix A.5). This means that $n(\mathrm{H^+})$ is more than 4 orders of magnitude higher than $n(\mathrm{H_3^+})$. Thus, from the condition of neutrality $n(\mathrm{H^+}) + n(\mathrm{H_3^+}) = n_e^*$, $n(\mathrm{H^+}) = n_e^*$ to a good approximation. We therefore obtain the steady-state equation for electrons, $\zeta n_\mathrm{H}/2 = [k_e n(\mathrm{H_3^+}) + k_r n_e^*]n_e^*$, which gives

$$n_e^* = \frac{k_e}{2k_r}n(\mathrm{H_3^+})\left[\sqrt{1 + \frac{2\zeta k_r n_\mathrm{H}}{[k_e n(\mathrm{H_3^+})]^2}} - 1\right]. \qquad (11)$$

The total electron number density is given by

$$n_e = \left(\frac{n_\mathrm{C}}{n_\mathrm{H}}\right)_\mathrm{SV} R n_\mathrm{H} + n_e^*, \qquad (12)$$

where the first and second terms represent electrons from the photoionization of carbon atoms and the cosmic-ray ionization of $\mathrm{H_2}$ and H, respectively. Using the carbon-to-hydrogen ratio after depletion of $(n_\mathrm{C}/n_\mathrm{H})_\mathrm{SV} = 1.6 \times 10^{-4}$ (Sofia et al. 2004) and the increase of metallicity from the solar vicinity to the GC of $R > 3$ (Appendix A.2), we find the electron number density from photoionization of carbon to be higher than $5 \times 10^{-4} n_\mathrm{H}$.

For a low value of $\zeta$, $n_e^*$ is negligible as given in our earlier analysis (Oka et al. 2005). Equation (11) indicates that as $\zeta$ increases, $n_e^*$ increases approximately as $\zeta n_\mathrm{H}/2k_e n(\mathrm{H_3^+})$. Numerical estimates indicate that the fraction of $n_e^*$ arising from ionization becomes significant for $\zeta = 10^{-15} \, \mathrm{s^{-1}}$, in approximate agreement with the result in Figure 2 of Le Petit et al. (2016). The above simplified treatment, in which the number density from carbon atoms is set as a constant and their participation neglected in the analysis, introduces some error in the region where $n_e^*$ is comparable to $(n_\mathrm{C}/n_\mathrm{H})_\mathrm{SV} R n_\mathrm{H}$, but Equation (8) and equations thereafter are accurate in regions with $\zeta \gg 10^{-15} \, \mathrm{s^{-1}}$ where $n_e^* \gg (n_\mathrm{C}/n_\mathrm{H})_\mathrm{SV} R n_\mathrm{H}$, which applies to the CMZ, as shown below.

### 5.2.4. Self-consistent Solution for $\zeta$

With the reduced $\mathrm{H_3^+}$ production rate discussed in Section 5.2.2 and the increased electron number density discussed in Section 5.2.3, steady-state $\mathrm{H_3^+}$ chemical equilibrium is described by

$$\zeta n_\mathrm{H}[f(\mathrm{H_2})]^2 = k_e[(n_\mathrm{C}/n_\mathrm{H})_\mathrm{SV} R n_\mathrm{H} + n_e^*]n(\mathrm{H_3^+}). \qquad (13)$$

Since $n_e$ is a function of $n(\mathrm{H_3^+})$ (Equation (8)), which in turn is a complicated function of $\zeta$, it is a hopeless task to solve this equation directly. Instead, we make use of the observed total $\mathrm{H_3^+}$ column density $N(\mathrm{H_3^+})$ and calculate $n(\mathrm{H_3^+}) = N(\mathrm{H_3^+})/L$ for assumed column lengths $L$. Equations (8) and (9) then have only two unknowns, $\zeta$ and $n_\mathrm{H}$. For each value of $n_\mathrm{H}$ we obtain $\zeta$ by simply solving a quadratic equation as shown in Appendix B.

We use $N(\mathrm{H_3^+}) = 3 \times 10^{15} \, \mathrm{cm^{-2}}$, which is typical of observed $\mathrm{H_3^+}$ column densities toward deeply embedded stars that are located near the center of the CMZ such as GCS 3-2, GCIRS 3, GCIRS 1W, etc. Plots of $\zeta$ as a function of $n_\mathrm{H}$ for assumed column lengths $L$ are given in Figure 10.
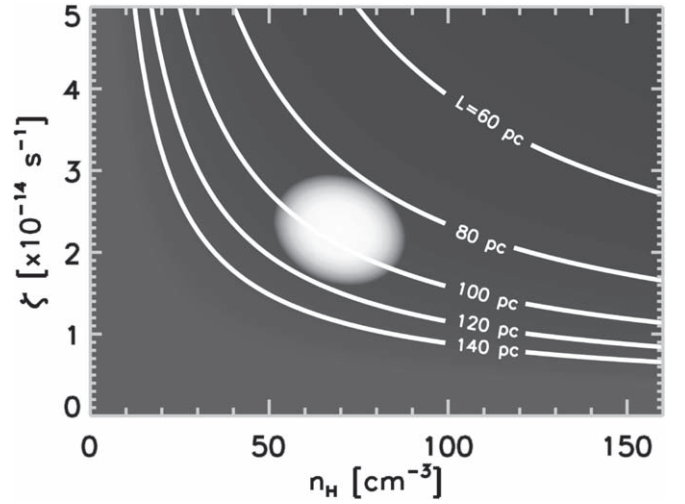


**Figure 10.** Cosmic-ray ionization rate $\zeta$ vs. hydrogen atom number density $n_\mathrm{H}$ for different values of diffuse cloud path length, $L$. This is a plot of Equation (B5) in which $x \equiv n_\mathrm{H}$ and $H \equiv N(\mathrm{H_3^+})/L$, where $N(\mathrm{H_3^+})$, the total column density of $\mathrm{H_3^+}$, is assumed to be $3 \times 10^{15} \, \mathrm{cm^{-2}}$. The white ellipse represents the most plausible values of $\zeta$, $n_\mathrm{H}$, and $L$.

### 5.2.5. Estimating $\zeta$ and L

Figure 10 indicates that the observed $\mathrm{H_3^+}$ column densities can be obtained by a wide range of $\zeta = (1\text{–}5) \times 10^{-14} \, \mathrm{s^{-1}}$, $n_\mathrm{H} = (20\text{–}140) \, \mathrm{cm^{-3}}$, and $L = (60\text{–}140)$ pc. This situation is parallel to Oka et al. (2005), in which $\zeta L$ was obtained from observed $N(\mathrm{H_3^+})$, but $\zeta$ and $L$ could not be uniquely separated. In this section, we attempt to separate them using various considerations to arrive at the most likely approximate mean values of $\zeta$, $n_\mathrm{H}$, and $L$ in the front half of the CMZ.

First, the analysis of observed data in Section 4.4 gave $n < 100 \, \mathrm{cm^{-3}}$. Since $n = n(\mathrm{H}) + n(\mathrm{H_2})$ and $n_\mathrm{H} = n(\mathrm{H}) + 2n(\mathrm{H_2})$ are related as $n = [1 - f(\mathrm{H_2})/2]n_\mathrm{H}$, the constraint on $n$ sets the upper limit of $n_\mathrm{H}$ in Figure 10 to be $n_\mathrm{H} < 140 \, \mathrm{cm^{-3}}$ for $f(\mathrm{H_2}) = 0.6$ (Appendix A.3). Although observational data from which to determine the value of $n$ are lacking, $n$ is unlikely to be much lower than the above upper limit in view of the high column density of $\mathrm{H_3^+}$. We adopt $n_\mathrm{H} \sim (60\text{–}70) \, \mathrm{cm^{-3}}$ and $L \sim (60\text{–}140)$ pc with $n(\mathrm{H_3^+})/n_\mathrm{H} \sim 10^{-7}$ as the most plausible values.

As for the most likely value of the cloud length $L$, we regard the large velocity spreads of the $\mathrm{H_3^+}$ absorption troughs of many of the spectra of centrally located stars (those shown in Figures 3 and 4) as indicating long absorption path lengths covering most of the distance from the center of the CMZ to its edge. As the sight line moves away from the center, the velocity dispersion decreases with relatively sharp absorptions found toward stars located near the eastern and western edges. This behavior is consistent with the warm and diffuse gas occupying a large portion of the CMZ, and therefore we assume $L \sim 100$ pc corresponding to a volume filling factor $f \sim 2/3$ for it.

From these considerations we propose the following parameters to be the most likely average values of the warm and diffuse gaseous environment: $\zeta \sim 2 \times 10^{-14} \, \mathrm{s^{-1}}$, $L \sim 100$ pc, $f = 2/3$, $n_\mathrm{H} \sim 70 \, \mathrm{cm^{-3}}$, $n \sim 50 \, \mathrm{cm^{-3}}$, $n(\mathrm{H_2}) \sim 20 \, \mathrm{cm^{-3}}$, $n(\mathrm{H}) \sim 30 \, \mathrm{cm^{-3}}$, $n(\mathrm{H_3^+}) \sim 1 \times 10^{-5} \, \mathrm{cm^{-3}}$, $n(\mathrm{H^+}) \sim n_e^* \sim 0.30 \, \mathrm{cm^{-3}}$, $n_e \sim 0.33 \, \mathrm{cm^{-3}}$. These values of $\zeta$, $L$, and $n_\mathrm{H}$ are shown in Figure 10 with approximate error limits. Assuming that the warm diffuse gas is in the shape of a disk with radius

**Table 7**
Most Likely Parameters for the Diffuse Molecular Cloud in the CMZ

| Physical Parameter | Symbol | Value | Units |
|---|---|---|---|
| Comic-ray ionization rate | $\zeta$ | $2 \times 10^{-14}$ | $(s^{-1})$ |
| Path length | $L$ | 100 | (pc) |
| Volume filling factor | $f$ | $\frac{2}{3}$ | |
| Density of hydrogen nuclei | $n_H$ | 70 | $(cm^{-3})$ |
| Gas density | $n$ | 50 | $(cm^{-3})$ |
| Density of molecular hydrogen | $n(H_2)$ | 20 | $(cm^{-3})$ |
| Density of atomic hydrogen | $n(H)$ | 30 | $(cm^{-3})$ |
| Density of $H_3^+$ | $n(H_3^+)$ | $1 \times 10^{-5}$ | $(cm^{-3})$ |
| Density of ionized hydrogen | $n(H^+)$ | 0.30 | $(cm^{-3})$ |
| Total density of electron | $n(e)$ | 0.33 | $(cm^{-3})$ |
| Mass of diffuse molecular cloud | | $6 \times 10^6$ | $(M_\odot)$ |

150 pc and scale height 30 pc, its total mass is estimated to be $\sim 6 \times 10^6 \, M_\odot$. A summary is given in Table 7.

### 5.2.6. Comparison with the Meudon Analysis

The Meudon analysis of Le Petit et al. (2016) uses a highly sophisticated code taking into account 165 species and 2850 chemical reactions. In contrast, here we consider only hydrogen and electrons. Le Petit et al. also consider the effects of the radiation scaling factor ($G_0$), radiative transfer, grains, polycyclic aromatic hydrocarbons, etc., which are all ignored in our treatment. We regard these differences of the treatments as minor in view of the dominant abundance of hydrogen and the smallness of the latter effects reported by Le Petit et al.

There, however, are two essential differences between the two methods. First, the Meudon analysis is for "small" diffuse clouds with maximum visual extinction $A_V$ max=1 mag with stars located outside of the cloud, while our calculation is for a much larger diffuse cloud with $A_V \sim 10$–30 mag and with the stars inside. Le Petit et al. thus explain our measured $H_3^+$ column densities as due to a pileup of absorptions from many small diffuse clouds, while we regard them as due to a single or a few large diffuse clouds covering large areas of the CMZ. Perhaps this is the reason why the path lengths $L$ shown in their Figures 13 and 14 are so much smaller than those shown in Figure 10 of this paper.

Second, the Meudon code calculates the $H_3^+$ abundance " ab initio" from assumed chemical abundances and environmental parameters. Thus, none of the $H_3^+$ column densities shown in Figure 1 of Le Petit et al. match the observed $N(H_3^+)$ of $3 \times 10^{15} \, cm^{-2}$ unless $n_H$ is considerably larger than $100 \, cm^{-3}$, contradictory to their limit of $n_H \leqslant 100 \, cm^{-3}$. On the contrary, all points in Figure 10 of this paper give the observed $N(H_3^+)$.

## 6. Discussion

### 6.1. Predominance of the Warm and Diffuse Gas in the CMZ

The analysis given above strongly suggests that the central 300 pc of the GC is dominated by warm ($T \sim 200$ K) and diffuse ($n < 100 \, cm^{-3}$) gas. This gas is of a different category than the diffuse component associated with dense gas, with $n \sim 10^{2.5} \, cm^{-3}$ and with lower temperature reported by Oka et al. (1998a) from observations of the $J = 2 \rightarrow 1$ CO emission and by Dahmen et al. (1998) from $J = 1 \rightarrow 0$ $C^{18}O$ emission. The new category of gas reported here, with

lower density and higher temperature, is not probed efficiently by molecular rotational radio emission since, even for CO with its abnormally small permanent dipole moment of $\mu = 0.1098$ D (Muenter 1975), the critical density for the lowest $J = 1 \rightarrow 0$ emission is much higher, on the order of $700 \, cm^{-3}$. Nevertheless, there have been several previous observations of the diffuse gas, albeit not as clearly stated as in this paper.

#### 6.1.1. Previous Observations of Diffuse ($n < 100 \, cm^{-3}$) Gas in the CMZ

The highly blueshifted broad OH radio absorptions at 1.6 GHz toward Sgr A, observed in early days of radio astronomy at velocities near $-120 \, km \, s^{-1}$ by Goldstein et al. (1964) and more accurately with higher spatial resolution at $-135 \, km \, s^{-1}$ by Bolton et al. (1964b), originate in the diffuse gas discussed in this paper. Robinson & McGee (1970) observed the 1667 MHz absorption continuously over a wide range of Galactic longitudes and noted that the blueshift decreases with longitude. Their measurements, along with the morphological studies by McGee (1970), led to the claimed existence by Kaifu et al. (1972) of the "Expanding Molecular Ring" (EMR) with an expansion velocity of $130 \, km \, s^{-1}$. The variation of blueshift with the Galactic longitude in Figure 2 of Robinson & McGee is similar to our observations of $H_3^+$ shown in Figure 7.

Likewise, the 4830 MHz absorption line of $H_2CO$, whose distribution is "very similar" to that of OH as observed (with higher angular resolution) by Scoville et al. (1972), must also be in the diffuse gas, although the blueshifted absorption is not as clearly noted in their Figure 2 as in Figure 2 of Robinson & McGee (1970). Nevertheless, Scoville (1972) also interpreted their observations as due to the "Expanding Molecular Ring," with an expansion velocity of $145 \, km \, s^{-1}$ similar to that of Kaifu et al. (1972). The existence of $H_2CO$ in diffuse clouds is well documented by Liszt & Lucas (1995); Liszt et al. (2006).

While the expansion velocities of the rings, 130 and $145 \, km \, s^{-1}$ observed in OH and $H_2CO$, respectively, are close to the maximum radial velocity, $\sim 140 \, km \, s^{-1}$, of the diffuse clouds observed in $H_3^+$, as shown in Figure 4, the velocity dispersion is much higher for the $H_3^+$ lines. Therefore, the morphology of the gas observed in OH and $H_2CO$ appears more like a ring. This suggests that $H_3^+$ is pervasive in the diffuse gas while OH and $H_2CO$ are more localized at higher radius, closer to the front of the expanding diffuse gas, and perhaps have a lower temperature (Goto et al. 2011). More detailed discussions on the morphology of this gas will be given in Paper II of this series.

Radio emission can also probe low-density gas if the critical density of the observed transition is low. The 3335 MHz CH emission line, with a critical density on the order of $3 \, cm^{-3}$, observed at high velocity dispersion by Magnani et al. (2006), must originate in the diffuse gas discussed in this paper. We note, though, that line emission has disadvantages compared with absorption in that (1) it does not straightforwardly discriminate between expansion and contraction and (2) determinations of column densities are complicated since collisions need to be taken into account. However, we expect that the general observability of CH makes its emission a powerful future probe for studying the diffuse gas in the CMZ.

In a recent noteworthy paper Corby et al. (2018) observed low-frequency (1–50 GHz) rotational *absorption* lines of 10

molecules, OH, c-C$_3$H$_2$, H$_2$CO, SiO, CS, CCS, HCS$^+$, H$_2$CS, l-C$_3$H, and l-C$_3$H$^+$, in the sight line toward Sgr B2(N) and interpreted all of them to be in diffuse or translucent clouds. While not all of them are likely in the $n < 100\,\mathrm{cm}^{-3}$ gas in which H$_3^+$ reside, their large column densities demonstrate the richness of chemistry in the diffuse interstellar medium in the CMZ.

### 6.1.2. The CMZ Is Not as Opaque as Previously Proposed

As pointed out in Section 1.2 and demonstrated by the relatively low extinctions we derive to stars in the Central Cluster, the Quintuplet Cluster, and other stars stretching across the CMZ, the CMZ is not as dominated by dense molecular clouds ($f \geqslant 0.1$), and therefore not as opaque, as originally proposed by Morris & Serabyn (1996). The intensity of the millimeter-wave dust continuum across the CMZ as mapped by Bally et al. (2010) also yields much lower extinctions over the vast majority of the CMZ than predicted by the above estimate (Appendix D). The most direct evidence for the much higher transparency of the CMZ based on data reported here comes from the absorption spectra of CO overtone lines, which are shown in Figure 6, whose characteristics are given in Table 3, and which are discussed in Section 4.3. All 18 stars listed in Table 3 are deeply embedded in the CMZ, as indicated by the large H$_3^+$ column densities toward them, and yet for most of them the CO absorptions are dominated by those in the foreground three spiral arms, whose total CO column densities correspond to visual extinctions ranging from 10 to 30 mag. The CO column densities arising in the CMZ correspond to visual extinctions of 10 mag or less for these stars. For the stars physically associated with the Sagittarius complexes A and E, the total CO column densities in the CMZ are higher, but still only comparable to those in the foreground arms rather than vastly larger. On all but one of these sight lines the visual extinction is at least an order of magnitude less than the mean value associated with such a large filling factor of dense gas.

It is only toward star $\iota$ in the Sagittarius B complex that overtone CO absorption is dominated by CO in the CMZ, as described in Section 4.2.3. The CO column density measured toward this star corresponds to $A_V \sim 300$ mag, which is unrealistically large as discussed in Section 4.3.2. The nature of this star, how deeply it is buried in Sgr B, the extinction law in Sgr B, and the dust-to-gas ratio in that dense molecular cloud complex are intriguing questions.

Radiation from stars located behind giant molecular clouds will be largely blocked. Therefore, there is some bias in interpreting column densities determined from CO infrared absorption spectroscopy as characterizing the entire CMZ. However, this effect must be minor in view of the very much smaller values of $A_V$ due to CMZ gas compared to the $A_V$ in the spiral arms toward almost all of the sight lines listed in Table 3. The only three cases in Table 3 for which $A_V$ in the CMZ is large and comparable to $A_V$ from the spiral arms are star $\alpha$, which lies behind two localized dense clouds, and GCIRS 3 and GCIRS 1W, which probably lie behind the circumnuclear disk. The cases of $\alpha$ and GCIRS 3 were discussed earlier in the paper (Sections 4.2.2 and 4.2.3). Moreover, although absorption spectroscopy probes only the columns of CMZ gas in front of the stars, it seems highly unlikely that, whatever determines the current distribution of gas in the CMZ, the asymmetry between gas abundances in the front and rear halves of the CMZ would be so extreme as having virtually all of the

$n \geqslant 10^4\,\mathrm{cm}^{-3}$ molecular gas located in the rear half of the CMZ, in order to explain the claimed filling factor of 0.1 or higher.

We therefore maintain that the combination of $n \geqslant 10^4\,\mathrm{cm}^{-3}$ and $f \geqslant 0.1$ in the CMZ is an overestimate by a factor of more than 30. On the other hand, if the observed CO is mostly located in gas with number densities of $\sim 10^{2.5}\,\mathrm{cm}^{-3}$ as reported by Oka et al. (1998a) and Dahmen et al. (1998), the volume filling factor of $f \geqslant 0.1$ may be approximately right. The filling factor of 0.1 for gas of density $10^4\,\mathrm{cm}^{-3}$ corresponds to a mass of $\sim 1 \times 10^9\,M_\odot$, 1/30 of which is comparable to the masses given by Oka et al. (1998a), $(2–6) \times 10^7\,M_\odot$, and Dahmen et al. (1998), $(2–5) \times 10^7\,M_\odot$.

The discovery of the predominance of diffuse molecular gas reported in this paper makes the term CMZ even more fitting.

### 6.1.3. The Highly Spatially Extended Ultrahot ($10^8$ K) X-Ray-emitting Plasma Does Not Exist

Intense apparently diffuse emission in the 6.7 keV iron line was discovered from the Galactic ridge (Koyama et al. 1986) and from the GC (Koyama et al. 1989) and was interpreted by those authors as thermal X-ray emission from ultrahot plasmas with temperatures of $\sim 10$ keV $\sim 10^8$ K. The emission extends over an angular size of $1°\!.8$, which suggested that its volume filling factor in the GC is large, possibly approaching unity. On the other hand, others (e.g., Pavlinsky et al. 1992), who observed X-rays in the same energy range, interpreted its origin differently because of the difficulty in finding a mechanism to create and maintain such spatially extended high-temperature gas (Sunyaev et al. 1993). Nevertheless, the concept of an ultrahot plasma dominating interstellar medium in the GC was accepted by many authors (e.g., Figure 9 of Lazio & Cordes 1998).

The *Chandra X-ray Observatory*, with a high spatial resolution ($0''\!.5$), resolved part of the diffuse X-ray emission into point sources (Muno et al. 2003), although it was reported that the dominant part of observed X-rays was still diffuse (Muno et al. 2004) in the GC, as well as in the Galactic ridge (Ebisawa et al. 2001, 2005). On the other hand, Wang et al. (2002) suggested that the presence of a large amount of $10^8$ K gas was no longer required. Belmont et al. (2005) maintained that an ultrahot helium plasma (after the ultrahot hydrogen escaped the GC region) extends over a few hundred parsecs in the GC region and proposed a viscous heating mechanism to heat and maintain it (Belmont & Tagger 2006). In contrast, Revnivtsev et al. (2006) interpreted the diffuse X-rays from the Galactic ridge as due to accumulation of point sources, mostly cataclysmic variables and coronally active binaries. Revnivtsev et al. (2009) resolved 80% of the seemingly diffuse X-ray emission into discrete sources, and Warwick (2014) and Warwick et al. (2014) associated virtually all X-ray sources with coronally active late-type stars. Others, however, have continued to maintain the presence of a large amount of pervasive ultrahot gas in the CMZ (Nobukawa et al. 2016; Yamauchi et al. 2016). Thus, whether such an ultrahot plasma occupies a large fraction of the volume of the CMZ has been a long-standing debate.

The predominance of the warm and diffuse gas claimed in this paper argues against the presence of a pervasive ultrahot plasma. The mechanism for production of such gas and maintaining an ultrahigh temperature is not known. Temperatures as high as $10^8$ K are possible only in the vicinities of stars

and supernovae. The high-energy ultrahot gas cannot coexist with extensive low-energy gas, such as the warm, diffuse gas reported here, because it is quickly cooled by the latter. Thus, we suspect that diffuse X-rays must be due to stars yet to be resolved and to the scattering of stellar X-rays by interstellar matter.

## 6.2. High $H_2$ Ionization Rate and Cosmic-Ray Flux

The estimated cosmic-ray $H_2$ ionization rate of $\zeta \sim 2 \times 10^{-14}$ s$^{-1}$ in the CMZ derived in Section 5.2 is an order of magnitude higher that that reported by Oka et al. (2005). The value derived here is near the low end of the range of values calculated by Le Petit et al. (2016), $\zeta = (1-11) \times 10^{-14}$ s$^{-1}$, but is the highest value determined for an extended region apart from that of Le Petit et al. From X-ray observations, Yusef-Zadeh et al. (2007) give much higher values of $\zeta = 5 \times 10^{-13}$ s$^{-1}$ for Sgr C and a similar value to ours for Sgr B1, Sgr B2, and the radio arc. Yusef-Zadeh et al. (2013) give a much lower value, $\zeta = (1-10) \times 10^{-15}$ s$^{-1}$, for a much more extended region ($\sim 300 \times 120$ pc) of the GC. The highest local value of $\zeta$ reported so far is $\zeta \sim 4.5 \times 10^{-12}$ s$^{-1}$ by Becker et al. (2011) for $\gamma$-ray-emitting supernova remnants.

### 6.2.1. Magnetic Fields in the CMZ

This work establishes that the cosmic-ray flux in the CMZ is $\sim 1000$ times higher than that in the solar vicinity (Webber 1998). If the equipartition assumption (e.g., Yoast-Hull et al. 2016) applies to the CMZ, as it does in the solar vicinity, this indicates an average magnetic field in the CMZ on the order of 100 $\mu$G. This is an order of magnitude lower than the estimates of $\sim 1$ mG by Yusef-Zadeh & Morris (1987) along the giant Radio Arc (Yusef-Zadeh et al. 1984) and by Morris & Yusef-Zadeh (1989), who argued that milligauss magnetic fields pervade much of the volume of the CMZ. On the other hand, Sofue et al. (1987) suggested a smaller magnetic field of 10–100 $\mu$G in the region of the Radio Arc. More recently a milligauss magnetic field was reported by Chuss et al. (2003) from submillimeter polarimetric observations based on the model calculations of Uchida et al. (1985).

However, as a result of observations of smaller-scale nonthermal filaments that look randomly oriented and of magnetic-field-related phenomena such as the Zeeman effect and Faraday rotation, as well as other astrophysical measurements, smaller pervading magnetic fields of less than 100 $\mu$G and even in the range of 1–10 $\mu$G have become favored (Boldyrev & Yusef-Zadeh 2006). For example, LaRosa et al. (2005) estimate the mean magnetic field in the GC to be on the order of 10 $\mu$G, an order of magnitude less than our estimate based on equipartition. Thus, there remain huge uncertainties in the mean value of the magnetic field in the GC, and the applicability or nonapplicability of equipartition law to the GC (Morris 2006) remains to be determined.

### 6.2.2. Heating and Cooling of the Gas in the CMZ

The high ionization rate on the order of $10^{-14}$ s$^{-1}$ indicates that the CMZ belongs to the category of giant cosmic-ray-dominated regions (CRDRs; Papadopoulos 2010), where cosmic rays are the ultimate regulator of temperature and ionization. The efficiency of X-rays in heating the gas was calculated by Ao et al. (2013) to be far too small. The ionization of the gas by X-rays is more than 3 orders of magnitude lower (M. Notani & T. Oka, in preparation). Other dynamic heating mechanisms such as turbulence claimed for heating of dense clouds in the CMZ (e.g., Ginsburg et al. 2016) will not work for the large-scale diffuse gas reported in this paper.

Heating the gas to a temperature much higher than the dust temperature, which is on the order of 20 K (e.g., Lis et al. 2001) in giant molecular clouds in the GC and 20 K + 50 K in diffuse clouds of the Arches and Quintuplet Cluster in the two-temperature model of Kaneda et al. (2012), must be due to cosmic rays. On the other hand, the temperature of the diffuse gas, 200 K, is far below that expected from the equipartition hypothesis. This is at least partly due to the efficient cooling of the gas by the spontaneous emission of the $H_3^+$ symmetry-breaking rotational transitions (Pan & Oka 1986) discussed in Section 1.6. $H_3^+$ is known to be an efficient coolant in planetary ionospheres (Miller et al. 2010, 2013). There, the role of $H_3^+$ is so decisive that the term "$H_3^+$ thermostat" was coined by Miller et al. (2000). $H_3^+$ as a coolant in the chemistry of primordial star formation was considered by Glover & Savin (2006, 2009).

## 7. Summary and Conclusions

In this paper, we have presented and analyzed velocity-resolved spectra, obtained at several telescopes, of selected lines of the fundamental band of $H_3^+$ in the 3.5–4.0 $\mu$m interval and of the first-overtone band of CO near 2.34 $\mu$m, on sight lines to stars stretching across the CMZ of the Galaxy, a region of radius 150 pc and thickness of $\sim 30$ pc. Previous observations of these lines, obtained toward stars within a few tens of pc of Sgr A*, and therefore near the very center of the CMZ, strongly suggested that on those sight lines most of the CMZ's $H_3^+$ resides in warm ($T \sim 200$ K) diffuse ($n < 100$ cm$^{-3}$) gas covering a large fraction of radius of the CMZ, and that the cosmic-ray ionization rate in the CMZ is considerably higher than in either dense or diffuse molecular clouds in the Galactic disk. We have since identified additional stars suitable for spectroscopy of interstellar $H_3^+$ and CO that cover a much wider range of Galactic longitudes within the CMZ. The present study demonstrates that the above gaseous environment and the high cosmic-ray ionization rate exist essentially throughout the front half of the CMZ. We believe that it is likely to exist in the rear half of the CMZ as well.

The key to understanding the physical conditions in this warm, diffuse gaseous environment is the $H_3^+$ molecule (trihydrium), first detected in the interstellar medium in 1996 (Geballe & Oka 1996) and first observed toward the GC in 1997 (Geballe et al. 1999). Although the number density of $H_3^+$ in the CMZ is only $\sim 10^{-6}$ times that of $H_2$ owing to its high chemical reactivity, the fully dipole-allowed infrared vibration–rotation spectrum of $H_3^+$ is $\sim 10^9$ times stronger than the quadrupole spectrum of $H_2$ (Oka 1981). Thus, the infrared absorption spectrum of $H_3^+$ is much more readily observable than that of $H_2$. $H_3^+$ also has a number of characteristics that make spectroscopy of it a highly sensitive probe of physical conditions in interstellar molecular gas, the main ones being its suitability as both a thermometer and (at low densities) a densitometer, as discussed in Section 1. Being a charged molecule and being created in a simple and straightforward manner following cosmic-ray ionization of $H_2$, it also is a powerful in situ probe to measure the cosmic-ray flux.

The spectra of $H_3^+$ lines in the CMZ reveal that the warm diffuse gas has high velocity dispersion, often producing line widths exceeding $100 \, \mathrm{km \, s^{-1}}$. For such a large range of velocities to exist on many widely separated sight lines, the gas must occupy a large volume within the CMZ. In contrast, in almost all cases the spectra of CO on these sight lines show little absorption attributable to CO in the CMZ, and in cases where such CO is evident, it exists in mostly narrow absorption features, suggesting that those absorptions arise in compact dense clouds. Because of the ubiquity of cosmic rays, $H_3^+$ exists wherever $H_2$ abounds, be it dense clouds or diffuse molecular clouds. CO, on the other hand, resides mostly in dense clouds. Thus, by comparing spectra of $H_3^+$ and CO on the same sight line, one usually can discriminate between $H_3^+$ absorption in dense and diffuse clouds. This is particularly useful for separating $H_3^+$ in the CMZ from $H_3^+$ in the foreground Galactic spiral arms.

Prior to our studies, the CMZ was widely considered to contain a large amount of dense ($n \geqslant 3 \times 10^3 \, \mathrm{cm^{-3}}$) gas with a significant volume filling factor ($f \geqslant 0.1$). The mean visual extinction of $A_V \geqslant 500$ mag over the $\sim 150$ pc radius of the CMZ would make it impossible to observe deeply into the CMZ on most sight lines. This is clearly far from the situation for the stars in the Central Cluster, which surround the supermassive central black hole, Sgr A*, and are easily observed, as well as for stars in the Quintuplet Cluster. The depths of the other stars that we have observed in this study are less well known or not known at all, but observations of high $H_3^+$ column densities comparable to those found toward stars in the Central Cluster, as well as similar extinctions to many of them as to the stars in the Central Cluster, indicate that most of them are also deeply embedded in the CMZ. Indeed, the ubiquity of the warm diffuse clouds containing copious $H_3^+$ allows one to adopt $N(H_3^+)$ as an approximate depth meter for the stars. We find that the above extinction is an overestimate, at least by a factor of 30.

That finding appears to be in accord with the large-scale infrared photometric surveys of stars in the GC by Cotera et al. (2000) and Schultheis et al. (2009), as well as with the millimeter-wave dust continuum mapping of Bally et al. (2010) (Appendix D). Undoubtedly there are some selection effects: our study is brightness limited, we cannot observe stars deeply embedded in or behind giant molecular clouds, and our observations are limited to only detecting absorption by gas in front of our background stars. But the statistics seem overwhelming. Whatever the mechanism of molecular production and dynamics, it is highly unlikely that average gas densities differ by an order of magnitude or more between the front and the back halves of the CMZ.

Two effects not included in our previous analyses of the diffuse cloud chemistry of $H_3^+$ have been added in the analysis presented here (Section 5). The exothermic charge exchange reaction $H_2^+ + H \rightarrow H_2 + H^+$, which reduces the $H_3^+$ production rate significantly for clouds with low $H_2$ fractions, is now included. Also, unlike in Oka et al. (2005), in which only electrons resulting from the photoionization of neutral carbon were considered, electrons produced from cosmic-ray ionization of H and $H_2$ are now taken into account (following Le Petit et al. 2016). We have developed a chemical model calculation in which only hydrogen and electrons are considered. Instead of the simple linear equation connecting the cosmic-ray ionization rate $\zeta$ and the observed $N(H_3^+)$ (Oka et al. 2005), a quadratic equation results from the present

analysis. As in Oka et al. (2005), $\zeta$ and the cloud length $L$ cannot be separated uniquely, but various considerations (chemistry, velocity dispersion, morphology, etc.) point to $\zeta \sim 2 \times 10^{-14} \, \mathrm{s^{-1}}$ and $L \sim 100$ pc being the most likely average values, the latter corresponding to a volume filling factor of $\sim 2/3$ for the warm diffuse gas. We find the most likely chemical parameters to be $n(H_2) \sim 20 \, \mathrm{cm^{-3}}$, $n(H) \sim 30$ $\mathrm{cm^{-3}}$, $n(H_3^+) \sim 1 \times 10^{-5} \, \mathrm{cm^{-3}}$, and $n_e \sim 0.33 \, \mathrm{cm^{-3}}$.

These observations and analyses lead to the following conclusions:

(1) Warm ($T \sim 200$ K) diffuse ($n \sim 50 \, \mathrm{cm^{-3}}$) gas dominates the volume of the CMZ. We have already pointed out above that the filling factor for dense gas must be much less than 0.1. The ultrahot ($T \sim 10^8$ K) X-ray-emitting plasma, which some thought to dominate the CMZ, cannot coexist with the warm diffuse gas and thus does not exist over extended regions. The observed diffuse X-ray emission in the CMZ must be due to point sources yet to be resolved and to scattering by interstellar atoms and molecules.

(2) The average cosmic-ray $H_2$ ionization rate in the CMZ that we deduce, $\zeta$, $\sim 2 \times 10^{-14} \, \mathrm{s^{-1}}$, is about 1000 times higher than in Galactic dense clouds and 10–100 times higher than in Galactic diffuse clouds. If the equipartition law stands, this suggests a pervading magnetic field in the CMZ on the order of $\sim 100 \, \mu$G.

## Appendix A
## Critical Evaluation of Parameters

*A.1. Rate Constant of the $H_3^+$ Dissociative Recombination, $k_e$*

In our previous analyses (Oka et al. 2005; Goto et al. 2008), the temperature-dependent experimental formula for $k_e$

determined using an ion storage ring by McCall et al. (2004), their Equation (7), was used. It was found subsequently that the rotational temperature $T_{rot}$ of $H_3^+$, which had been measured to be low (22–37 K) at the inlet of the ring, was much higher in the body of the ring and $\sim 380$ K (Petrignani et al. 2011; Kreckel et al. 2012). The dependence of $k_e$ on $T_{rot}$ of $H_3^+$ is a complicated issue.

Here we continue to use the value of McCall et al. (2004) based on the following two justifications: (1) Figure 2 of Fonseca dos Santos et al. (2007) gives their theoretical calculations of $k_e$ as a function of electron energy $E_\parallel$(eV) for $T_{rot} = 13$ and 300 K. The two curves cross at $E_e \sim 21.5$ meV $\sim 250$ K, suggesting nearly equal $k_e$ for $T_{rot} = 30$ and 360 K. (2) It has been reported that the reaction rates for $C + H_3^+$ (O'Connor et al. 2015) and $O + H_3^+$ (de Ruette et al. 2016) are not significantly affected by the $H_3^+$ internal temperature. Argument 2 is not as direct as argument 1, but the temperature range is very high ($\sim 3000$ K).

### A.2. The C/H Ratio in the CMZ, $(n_C/n_H)_{SV}R$

Along diffuse and translucent sight lines in the solar vicinity, the carbon-to-hydrogen ratio in the gas phase is $(n_C/n_H)_{SV} = 1.6 \times 10^{-4}$ (Sofia et al. 2004). In the GC the ratio is multiplied by a factor of $R$ to take into account the increase of metallicity from solar vicinity to the GC. In the past we (Oka et al. 2005; Goto et al. 2008) have used $R = 3$–$10$ on the assumption that the increase of metallicity is close to that of $1/X = I_{CO}/N(H_2)$ (Sodroski et al. 1995; Arimoto et al. 1996).

There is considerable literature on the measurements of the elemental abundance gradient $g$ (in dex kpc$^{-1}$) in the Galactic disk that gives $R = 10^{gD}$, where $D$ (in kpc) is the distance to the GC. The summary of measured abundance gradients in Table 1 of Chiappini et al. (2001) indicates that interstellar measurements in the H II regions and planetary nebulae give fairly consistent abundance gradients ($g \sim 0.07$ dex kpc$^{-1}$) with low measurement uncertainties, while those of stars give smaller gradients with high uncertainties and values scattered from 0 to 0.1 dex kpc$^{-1}$, perhaps reflecting individual characteristics of the stellar atmospheres. Here we use interstellar measurements because of their consistency and also because we are applying them to interstellar gas.

Most measurements do not extend all the way to the GC. Among those few who do, Simpson et al. (1995) give an [N/H] gradient of $-(0.10 \pm 0.02)$ dex kpc$^{-1}$ corresponding to $R = 7.1 \pm 1.4$. Afflerbach et al. (1997) find an [N/H] gradient of $-(0.072 \pm 0.006)$ dex kpc$^{-1}$ and an [O/H] gradient of $-(0.064 \pm 0.009)$ dex kpc$^{-1}$, corresponding to $R = 4.1 \pm 0.4$ and $R = 3.5 \pm 0.5$, respectively. Rudolph et al. (1997) give an [N/H] gradient of $-(0.111 \pm 0.012)$ dex kpc$^{-1}$ corresponding to $R = 8.8 \pm 0.9$. All those authors assumed a GC distance of 8.5 kpc. Other observations reported in many other papers that do not reach the GC tend to give somewhat lower gradient and $R$ values. Most measurements are for O, N, and S, and very few are for C, although Rolleston et al. (2000) (GC distance 8.5 kpc) give a [C/H] gradient of $-(0.07 \pm 0.01)$ dex kpc$^{-1}$ corresponding to $R = 3.9 \pm 0.5$. A higher [C/H] gradient of $-(0.103 \pm 0.018)$ dex kpc$^{-1}$ has been reported by Esteban et al. (2005) (GC distance 8.0 kpc), which corresponds to $R = 6.7 \pm 1.3$.

Based on the above values, we continue to use $R = 3$ (Oka et al. 2005; Goto et al. 2008) as the lower limit for the increase of C/H ratio from the solar vicinity to the GC. The accuracy of $R$ is less essential in the chemical analysis of this paper than in Oka et al. (2005) since the electrons from cosmic-ray ionization of $H_2$ and H, rather than from photoionization of C, are dominant.

### A.3. Fraction of Molecular Hydrogen, $f(H_2)$

This parameter affects the value of $\zeta$ seriously because its square appears in the master Equation (13). In our previous papers (Oka et al. 2005; Goto et al. 2008), where the master equation was linear in $f(H_2)$, we assumed $f(H_2) = 1$. This seriously underestimates the value of $\zeta$ if $f(H_2)$ is significantly smaller than 1. Values of $f(H_2)$ are given for diffuse clouds in the Galactic disk toward the star $\zeta$ Per and X Per as 0.60 and 0.76, respectively, in Table 4 of Indriolo et al. (2007) based on the direct measurements of $N(H_2)$ and $N(H)$ by the *Far Ultraviolet Spectroscopic Explorer* (Rachford et al. 2002). For other stars, they used $f(H_2) = 2/3 = 0.67$, which approximates those values and corresponds to the special case of $n(H) = n(H_2)$.

For the CMZ, Le Petit et al. (2016) find $f(H_2) = 0.6$, from their analysis using the Meudon PDR code of the $OH^+$, $H_2O^+$, and $H_3O^+$ column densities toward Sgr B2(N) reported by Indriolo et al. (2015). Le Petit et al. claim that this value agrees with the value calculated directly from $N(H)$ reported by Indriolo et al. (2015) and $N(H_2)$ obtained from the Meudon analysis of HF (Godard et al. 2012) listed in their Table 6. The value of 0.6 is also consistent with their Figure 3, in which $f(H_2)$ is plotted as a function of $\zeta$.

The Meudon value of $f(H_2) = 0.6$ is drastically different from $f(H_2) = 0.08 \pm 0.02$ of the analysis toward Sgr B2(N) by Indriolo et al. (2015). Le Petit et al. pointed out that this discrepancy was caused by the small electron fraction $x_e \sim 1.5 \times 10^{-4}$ based on the assumption that electrons are all from photodissociation of C atoms, the same assumption Oka et al. (2005) made. This is reasonable for ordinary diffuse clouds in the Galactic disk, where $\zeta$ is less than $10^{-15}$ s$^{-1}$, but not for the GC, where $\zeta$ and thus $x_e$ are much higher.

Based on these considerations, here we use $f(H_2) = 0.6$.

### A.4. Rate Constant for Charge Exchange Reaction $H_2^+ + H \rightarrow H_2 + H^+$

The experimental value of $k_6 = (6.4 \pm 1.2) \times 10^{-10}$ by Karpas et al. (1979) may not be accurate because the quoted low uncertainty does not include the systematic error in the ratio of atomic and molecular hydrogen [H]/[H$_2$] used in its derivation. The theoretical cross sections of the reaction given in Table 1 of Last et al. (1997) are ordinary Langevin cross sections, suggesting that the experimental $k_6$ may be too low. Also, Table 1 of Karpas et al. (1979) indicates that their method tends to give a low rate constant even for ordinary ion-neutral reactions. In view of this uncertainty we here assume $k_6 = k_1/2$ partly because it gives a simple expression of the $H_3^+$ production rate $\zeta[f(H_2)]^2$. If the experimental value is correct, this assumption underestimates the $H_3^+$ production rate by 14% for $f(H_2) = 0.6$ reported by Le Petit et al. (2016). If $k_6 \sim k_1$, this overestimates the $H_3^+$ production rate by 40%. Since charge exchange reactions often are slower than the Langevin rate (Huntress, private communication), the assumption of $k_6 = k_1/2$ may be reasonable. Determination of $k_6$ using modern

experimental techniques (e.g., Allmendinger et al. 2016) and more theoretical study of this important reaction are highly desirable.

### A.5. Radiative Recombination Rate Constant of H$^+$

Since the groundbreaking work by Menzel (1937), radiative recombination of protons has been studied by many astrophysicists (e.g., Spitzer 1948; Seaton 1959). Hollenbach & McKee (1989) used

$$k_r = 3.60 \times 10^{-12}(T/300)^{-0.75} \text{ cm}^3 \text{ s}^{-1}, \tag{14}$$

by Aldovandi & Péquignot (1973), which gives $k_r = 4.1 \times 10^{-12}$ cm$^3$ s$^{-1}$ for $T = 200$ K. A more recent calculation by Badnell (2006) using

$$k_r = A\left[\sqrt{\frac{T}{T_0}}\left(1 + \sqrt{\frac{T}{T_0}}\right)^{1-B}\left(1 + \sqrt{\frac{T}{T_1}}\right)^{1+B}\right]^{-1} \tag{15}$$

with $A = 8.32 \times 10^{-11}$ cm$^3$ s$^{-1}$, $T_0 = 2.97$ K, and $T_1 = 7.0 \times 10^5$ K gives $k_r = 5.7 \times 10^{-12}$ cm$^3$ s$^{-1}$ for $T = 200$ K. Thus, the radiative recombination rate constant $k_r$ of H$^+$ is $2 \times 10^4$ times smaller than the dissociative recombination of H$_3^+$, $k_e$.

### Appendix B
### Solution of Equation (9)

From Equations (8) and (9) the steady-state equation for H$_3^+$ is written explicitly as

$$\zeta n_H[f(H_2)]^2 = k_e n(H_3^+)\left[\left(\frac{n_C}{n_H}\right)_{SV} R n_H\right.$$
$$\left. + \frac{k_e}{2k_r}n(H_3^+)\left(\sqrt{1 + \frac{2\zeta k_r n_H}{[k_e n(H_3^+)]^2}} - 1\right)\right], \tag{16}$$

which gives the solution

$$\zeta = \frac{2\rho K}{f^2} + \frac{K^2(1-f^2)}{kf^4} + \frac{1}{f^4}\sqrt{\frac{4\rho K^3 f^2}{k} + \frac{K^4(1-f^2)^2}{k^2}}, \tag{17}$$

where $\rho \equiv (n_C/n_H)_{SV}R$, $K \equiv k_e n(H_3^+)$, $f \equiv f(H_2)$, and $k = n_H k_r$. Using numerical values $k_e = 8.68 \times 10^{-8}$ cm$^3$ s$^{-1}$, calculated from Equation (7) of McCall et al. (2004) for $T = 200$ K, $\rho = 4.8 \times 10^{-4}$, $f(H_2) = 0.6$, and $k_r = 5.7 \times 10^{-12}$ cm$^3$ s$^{-1}$ discussed in Appendices A.1, A.2, A.3, and A.5, respectively, we obtain a numerical expression for $\zeta$ in terms of $n_H \equiv x$ and $n(H_3^+) = N(H_3^+)/L \equiv H$ as

$$\zeta = (1.50 \times 10^{-11}Hx^2 + 4.23 \times 10^{-4}H^2x$$
$$+ \sqrt{2.00 \times 10^{-14}H^3x^3 + 1.79 \times 10^{-7}H^4x^2})/0.0648x^2. \tag{18}$$

In Figure 10, $\zeta$ is plotted as a function of $x$ for assumed values of $L$.

### Appendix C
### Similarities and Differences between H$_3^+$ and NH$_3$

H$_3^+$ is similar to NH$_3$ in many ways. They have identical symmetry of $D_{3h}$ and hence the same ortho ($I = 3/2$) and para ($I = 1/2$) spin modifications and parity $(-1)^K$. H$_3^+$ and NH$_3$ (and isoelectronic H$_3$O$^+$) are the only oblate symmetric tops observed in the CMZ, and their rotational level structures are similar (Figure 1); both have $J = K$ metastable levels that are lower than $J > K$ levels. However, they have a few differences that result in profound differences in their astrophysical behaviors as observed in the CMZ.

### C.1. Planar Nonpolar H$_3^+$ versus Quasi-planar Polar NH$_3$

While the equilibrium structure of H$_3^+$ is planar, NH$_3$ is pyramidal with high permanent dipole moment $\mu = 1.468$ D (Townes & Schawlow 1955), and its plane symmetry is caused by the inversion motion of the molecule. The motion produces many strong inversion lines in the centimeter region whose frequencies are only mildly dependent on the rotational quantum numbers $J$ and $K$, and thus very high rotational levels can be observed. NH$_3$ and its isoelectronic H$_3$O$^+$ (Liu & Oka 1985; Lis et al. 2014) are unique in this respect. On the other hand, H$_3^+$ is nonpolar and its observation is limited to the infrared.

Initially the lifetimes of the $J = K$ metastable levels were thought to be longer than that of the universe (Cheung et al. 1969). Theoretical work indicated that because of SBS due to vibration–rotation interaction, they are many orders of magnitude shorter (Oka et al. 1971). The lifetime of the spontaneous emission is approximately proportional to $B^{-6}$, where $B$ is the rotational constant and is much shorter for H$_3^+$ ($B \sim 44$ cm$^{-1}$) than for NH$_3$ ($B \sim 9.9$ cm$^{-1}$) (Pan & Oka 1986). While for NH$_3$ the lifetime of the $(2, 2) \rightarrow (1, 1)$ spontaneous emission is ~230 yr, it is 27 days for H$_3^+$, with the critical density on the order of 200 cm$^{-3}$.

Although the lowest $(0, 0)$ rotational level is allowed for the asymmetric inversion $(-)$ level of NH$_3$, it is not allowed for H$_3^+$, making the $(1, 1)$ level the ground level (Landau & Lifshitz 1977). NH$_3$ in the $(3, 3)^\pm$ levels may reach the ground $(0, 0)^-$ level via three spontaneous emissions, while H$_3^+$ in the $(3, 3)$ level cannot make transitions to lower levels without violating the ortho-para rule, which takes longer than the lifetime of the universe.

### C.2. Chemical (H$_3^+$) versus Physical (NH$_3$) Collisions

Collisions between H$_3^+$ and H$_2$ are qualitatively different from those between NH$_3$ and H$_2$. The former are chemical reactions in which protons scramble in the $(H_5^+)^*$ intermediate complex, making ortho-para transitions possible for both H$_3^+$ and H$_2$ (Quack 1977; Oka 2004). Thus, collision-induced transitions can occur between any pair of H$_3^+$ levels. On the other hand, a collision between NH$_3$ and H$_2$ is a physical collision in which protons do not scramble. The collisional processes follow near rigorous ortho–ortho and para–para selection rules (Oka 1968, 1973). While H$_3^+$ thermalizes quickly to any level at the high Langevin rate, NH$_3$ thermalizes slowly following the spin isomer rule to limited levels. An NH$_3$ molecule in a high metastable $J = K$ ($J > 2$) level changes its quantum state only to $(J', K - 3)$ with $J' \geqslant K - 3$.

### C.3. Subthermal $H_3^+$ versus Suprathermal $NH_3$

Because of the rapid symmetry-breaking spontaneous emission, the rotational distribution of $H_3^+$ is subthermal, as demonstrated by the observed low population in the (2, 2) level. Along with the rapid vibrational spontaneous emission, this makes $H_3^+$ an efficient coolant in planetary ionospheres (Miller et al. 2000; see Section 5.2.2). On the other hand, for $NH_3$, the $(J, J)$ metastable level is higher than the $(J − 1, J − 3)$ level for $J \leqslant 10$, but their order reverses at $J = 10$. Therefore, the symmetry-breaking spontaneous emissions $(J, J) \rightarrow (J − 1, J − 3)$ are quenched beyond $J > 10$; the only way for them to cool is via collisions. But the $\Delta K = 3$ collisions are slow (Oka 1973). $NH_3$ in those metastable levels cannot cool easily. The rotational distribution of $NH_3$ is suprathermal. The observation of $NH_3$ at high energy levels, 1930 K for the (14, 14) metastable level reported by Hüttemeister et al. (1995) and 3130 K for the (18, 18) metastable level reported by Wilson et al. (2006), is due to this effect. The presence of metastable levels may also explain the higher kinetic temperatures $T_k > 600$ K toward Sgr B2 reported by Hüttemeister et al. (1995), $T_k = (700 \pm 100)$ K toward Sgr B2 by Ceccarelli et al. (2002), and $T_k \sim 600$ K toward many giant molecular clouds by Mills & Morris (2013) using $NH_3$, compared with lower temperatures of $T_k \sim 300$–500 K toward Sgr B2 reported by Cernicharo et al. (2006) and $T_k \geqslant 400$ K toward the Sgr A complex reported by Sonnentrucker et al. (2013) using $H_2O$, which does not have the metastability.

## Appendix D
## Agreement between Visual Extinction from Our CO Absorption and from Dust Continuum Emission by Bally et al. (2010)
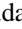
The visual extinctions $A_V$ obtained from the infrared absorption of CO listed in Table 3 of this paper and those determined from millimeter dust continuum by Bally et al. (2010) in their Table 3 are remarkably similar in view of the entirely different methods of the observations and analyses. Both observations indicate that the previous estimate of volume filling factor $f \geqslant 0.1$ for dense clouds with density $n \geqslant 10^4$ cm$^{-3}$, is an overestimate by a factor of at least 30.

Out of the 1429 Bolocat clumps listed in the paper by Bally et al., 616 lie within the CMZ. In both tables, there is a region of minimum optical thickness in the direction of the Quintuplet Cluster. Their Bolocam Galactic Survey (BGPS) #63 ($G_{lon} = 0°.164$, $G_{lat} = 0°.079$) gives equivalent column density $N_{40} = 6 \times 10^{21}$ cm$^{-2}$, which corresponds to $A_V \sim 6$ mag in their analysis. Our CO measurement in Table 3 gives $A_V$(CMZ) $\sim 7$ mag toward GCS 3-2 ($0°.164$, $-0°.061$). In this comparison we assume that the emission observed by Bally et al. is from relatively high temperature dust in the CMZ and that the emission from low-temperature spiral arms is negligible. In both tables the region of highest optical thickness is toward Sgr B2; BGPS #227 ($0°.680$, $-0°.029$) gives $N_{40} = 1.9 \times 10^{24}$ cm$^{-2}$ corresponding to $A_V \sim 1900$ mag, while our CO observation toward J17470898 ($\iota$) ($0°.549$, $-0°.059$) between Sgr B1 and B2 gives $A_V \sim 270$ mag. Out of the 616 BGPS data BGPS #227 is the only one that shows $A_V > 500$ mag. The second highest is BGPS #223 ($0°.656$, $-0°.045$), with $N_{40} = 4.6 \times 10^{23}$ cm$^{-2}$ and $A_V \sim 460$ mag. The values of $A_V$ of all other BGPS objects are lower than 120 mag.

These and other agreements between the results of two different measurements must be somewhat fortuitous, but this justifies the following statistical argument using Table 3 of Bally et al. (2010). The majority (80%) of the BGPS data give more than 30 times lower values of $A_V$ than would be produced by dust in dense ($n \geqslant 10^4$ cm$^{-3}$) clouds with a CMZ filling factor $f \geqslant 0.1$.

Although the 1.1 mm and 350 $\mu$m images and contours given in figures of Bally et al. may give an impression that the CMZ is covered by giant molecular clouds, only nine BGPS points have column densities higher than $N_{40} = 1 \times 10^{23}$ cm$^{-2}$. They are #227 ($1.9 \times 10^{24}$ cm$^{-2}$), #223 ($4.6 \times 10^{23}$ cm$^{-2}$), and #170 ($1.2 \times 10^{23}$ cm$^{-2}$) near Sgr B; #1411 ($1.6 \times 10^{23}$ cm$^{-2}$) near Sgr A; #1388 ($1.4 \times 10^{23}$ cm$^{-2}$) and #1391 ($1.1 \times 10^{23}$ cm$^{-2}$) near star $\epsilon-$; #96 ($1.1 \times 10^{23}$ cm$^{-2}$) and #99 ($1.0 \times 10^{23}$ cm$^{-2}$) near star $\theta$; and #1314 ($1.0 \times 10^{23}$ cm$^{-2}$) near star $\delta$. If $H_2$ column densities $N_{40} \geqslant 1 \times 10^{23}$ cm$^{-2}$ define giant molecular clouds, their areal filling factor in the CMZ is 1–2%.

## ORCID iDs

T. R. Geballe https://orcid.org/0000-0003-2824-3875
Tomonori Usuda https://orcid.org/0000-0001-9855-0163
Benjamin, J. McCall https://orcid.org/0000-0003-1022-7295
Nick Indriolo https://orcid.org/0000-0001-8533-6440

## References

Afflerbach, A., Churchwell, E., & Werner, M. W. 1997, ApJ, 478, 190
Aguado, A., Barragan, P., Prosmiti, R., et al. 2010, JChPh, 133, 024306
Aitken, D. K., Jones, B., & Penman, J. M. 1974, MNRAS, 169, 35
Aldovandi, S. M. V., & Péquignot, D. 1973, A&A, 25, 137
Allmendinger, P., Deiglmayr, J., Schullian, O., et al. 2016, ChemPhysChem, 17, 3596
Amo-Baladrón, M. A., Martín-Pintado, J., & Martín, S. 2011, A&A, 526, A54
Anicich, V. G., & Huntress, T. R., Jr 1986, ApJS, 62, 553
Ao, Y., Henkel, C., Menten, K. M., et al. 2013, A&A, 550, A135
Arimoto, N., Sofue, Y., & Tsujimoto, T. 1996, PASJ, 48, 275
Armijos-Abendaño, J., Martín-Pitado, J., Requena-Torres, M. A., Martín, S., & Rodriguez-Franco, A. 2015, MNRAS, 446, 3842
Avery, L. W., Broten, N. W., MacLeod, J. M., Oka, T., & Kroto, H. W. 1976, ApJL, 205, L173
Badnell, N. R. 2006, ApJS, 167, 334
Bally, J., Aguirre, J, Battersby, C., et al. 2010, ApJ, 721, 137
Bally, J., Stark, A. A., Wilson, R. W., & Henkel, C. 1988, ApJ, 324, 223
Bania, T. M. 1977, ApJ, 216, 381
Becker, J. K., Black, J. H., Safarzadeh, M., & Shuppan, F. 2011, ApJL, 739, L43
Becklin, E. E., & Neugebauer, G. 1968, ApJ, 151, 145
Becklin, E. E., & Neugebauer, G. 1969, ApJL, 157, L31
Becklin, E. E., & Neugebauer, G. 1975, ApJL, 200, L71
Belmont, R., & Tagger, M. 2006, A&A, 452, 15
Belmont, R., Tagger, M., Muno, M., Morris, M., & Cowley, S. 2005, ApJL, 631, L53
Bohlin, R. C., Savage, B. D., & Drake, J. F. 1978, ApJ, 224, 132
Boldyrev, S., & Yusef-Zadeh, F. 2006, ApJL, 637, L101
Bolton, J. G., Gardner, F. F., McGee, R. X., & Robinson, B. J. 1964a, Natur, 204, 30
Bolton, J. G., van Damme, K. J., Gardner, F. F., & Robinson, B. J. 1964b, Natur, 201, 279
Bowyer, S., Byram, E. T., Chubb, T. A., & Friedman, H. 1965, Sci, 147, 394
Boyce, P. J., & Cohen, R. J. 1994, A&AS, 107, 563
Brittain, S. D., Simon, T., Kulesa, C., & Rettig, T. W. 2004, ApJ, 606, 911
Ceccarelli, C., Baluteau, J.-P., Walmsley, M., et al. 2002, A&A, 383, 603
Cernicharo, J., Goicoechea, J. R., & Pardo, J. R. 2006, ApJ, 642, 940
Cheung, A. C., Rank, D. M., Townes, C. H., Knowles, S. H., & Sullivan, W. T., III 1969, ApJL, 157, L13
Cheung, A. C., Rank, D. M., Townes, C. H., Thornton, D. D., & Welch, W. J. 1968, PhRvL, 21, 1701

Chiappini, C., Matteucci, F., & Romano, D. 2001, ApJ, 554, 1044
Chuss, D. T., Novak, G., Davidson, J. A., et al. 2003, AN, 324, 173
Clark, G. W., Garmire, G. P., & Kraushaar, W. L. 1968, ApJL, 153, L203
Cohen, R. J., & Few, R. W. 1976, MNRAS, 176, 495
Cohen, R. J., & Few, R. W. 1981, MNRAS, 194, 711
Corby, J. F., McGuire, B. A., Herbst, E., & Remijan, A. J. 2018, A&A,
    610, A10
Cotera, A. S., Simpson, J. P., Erickson, E. F., et al. 2000, ApJS, 129, 123
Dahmen, G., Hüttemeister, S., Wilson, T. L., & Mauersberger, R. 1998, A&A,
    331, 959
Dalgarno, A. 2006, PNAS, 103, 12269
de Ruette, N., Miller, K. A., O'Connor, A. P., et al. 2016, ApJ, 816, 31
Ebisawa, K., Maeda, Y., Kaneda, H., & Yamauchi, S. 2001, Sci, 293, 1633
Ebisawa, K., Tsujimoto, M., Paizis, A., et al. 2005, ApJ, 635, 214
Espinoza, P., Selman, F. J., & Melnick, J. 2009, A&A, 501, 563
Esteban, C., García-Rojas, J., Peimbert, M., et al. 2005, ApJL, 618, L95
Felli, M., Testi, L., Schuller, F., & Omont, A. 2002, A&A, 392, 971
Fonseca dos Santos, S., Kokoouline, V., & Greene, C. H. 2007, JChPh, 127,
    124309
Fritz, T. K., Gillessen, S., Dodds-Eden, K., et al. 2011, ApJ, 737, 73
Fukui, Y., Iguchi, T., Kaifu, N., et al. 1977, PASJ, 29, 643
Gatley, I., Jones, T. J., Hyland, A. R., Beattie, D. H., & Lee, T. J. 1984,
    MNRAS, 210, 565
Geballe, T. R., Baas, F., & Wade, R. 1989, A&A, 208, 255
Geballe, T. R., Goto, M., Usuda, T., Oka, T., & McCall, B. J. 2006, ApJ,
    644, 907
Geballe, T. R., Lambrides, E., Schlegelmilch, B., et al. 2019, ApJ, 872, 103
Geballe, T. R., Mason, R. E., & Oka, T. 2015, ApJ, 812, 56
Geballe, T. R., McCall, B. J., Hinkle, K. H., & Oka, T. 1999, ApJ, 510, 251
Geballe, T. R., & Oka, T. 1989, ApJ, 342, 855
Geballe, T. R., & Oka, T. 1996, Natur, 384, 334
Geballe, T. R., & Oka, T. 2010, ApJL, 709, L70
Giannetti, A., Leurini, S., König, C., et al. 2017, A&A, 606, L12
Gibb, E. L., Brittain, S. D., Rettig, T. W., et al. 2010, ApJ, 715, 757
Ginsburg, A, Henkel, C., Ao, Y., et al. 2016, A&A, 586, A50
Glassgold, A. E., & Langer, W. D. 1974, ApJ, 193, 73
Glover, S., & Savin, D. W. 2006, RSPTA, 364, 3107
Glover, S. C. O., & Savin, D. W. 2009, MNRAS, 393, 911
Godard, B., Falgarone, E., Gerin, M., et al. 2012, A&A, 540, A87
Goicoechea, J. R., Etxaluze, M., Cernicharo, J., et al. 2013, ApJL, 769, L13
Goldreich, P., & Kwan, J. 1974, ApJ, 189, 441
Goldstein, S. J., Gundermann, E. J., Penzias, A. A., & Lilley, A. E. 1964,
    Natur, 203, 65
Gómez-Carrasco, S., González-Sánchez, L., Aguado, A., et al. 2012, JChPh,
    237, 094303
Goto, M., Geballe, T. R., Indriolo, N., et al. 2014, ApJ, 786, 96
Goto, M., Indriolo, N., Geballe, T. R., & Usuda, T. 2013, JPCA, 117, 9919
Goto, M., McCall, B. J., Geballe, T. R., et al. 2002, PASJ, 54, 951
Goto, M., Usuda, T., Geballe, T. R., et al. 2011, PASJ, 63, L13
Goto, M., Usuda, T., Nagata, T., et al. 2008, ApJ, 688, 306
Güsten, R., Walmsley, C. M., & Pauls, T. 1981, A&A, 103, 197
Habibi, M., Stolte, A., Brandner, W., Hußmann, B., & Motohara, K. 2013,
    A&A, 556, A26
Heiligman, G. M. 1987, ApJ, 314, 747
Herbst, E., & Klemperer, W. 1973, ApJ, 185, 505
Hildebrand, R. H., Whitcomb, S. E., Winston, R., et al. 1978, ApJL, 219, L101
Hoffmann, W. E., & Frederick, C. L. 1969, ApJL, 155, L9
Hollenbach, D., & McKee, C. F. 1989, ApJ, 342, 306
Hüttemeister, S., Dahmen, G., Mauersberger, R., et al. 1998, A&A, 334, 646
Hüttemeister, S., Wilson, T. L., Bania, T. M., & Martín-Pintado, J. 1993, A&A,
    280, 255
Hüttemeister, S., Wilson, T. L., Mauersberger, R., et al. 1995, A&A, 294, 667
Indriolo, N., Geballe, T. R., Oka, T., & McCall, B. J. 2007, ApJ, 671, 1736
Indriolo, N., & McCall, B. J. 2012, ApJ, 745, 91
Indriolo, N., Neufeld, D. A., Gerin, M., et al. 2015, ApJ, 800, 40
Jackson, J. M., Heyer, M. H., Paglione, T. A. J., & Bolatio, A. D. 1996, ApJL,
    456, L91
Jones, P. A., Burton, M. G., Cunningham, M. R., et al. 2012, MNRAS,
    419, 2961
Jones, P. A., Burton, M. G., Cunningham, M. R., Tothill1, N. F. H., &
    Walsh, A. J. 2013, MNRAS, 433, 221
Kaifu, N., Kato, T., & Iguchi, T. 1972, Natur, 238, 105
Kaneda, H., Yasuda, A., Onaka, T., et al. 2012, A&A, 543, A79
Karpas, Z., Anicich, V., & Huntress, W. T., Jr. 1979, JChPh, 70, 2877
Kellogg, E., Gursky, H., Murray, S., Tananbaum, H., & Giacconi, R. 1971,
    ApJL, 169, L99

Koyama, K., Awaki, H., Kunieda, H., et al. 1989, Natur, 339, 603
Koyama, K., Makishima, K., Tanaka, Y., & Tsunemi, H. 1986, PASJ, 38, 121
Kreckel, H., Petrignani, A., Novotny, O., et al. 2012, RSPTA, 370, 5088
Krieger, N., Ott, J., Beuther, H., et al. 2017, ApJ, 850, 77
Kruijssen, J. M. D., Dale, J. E., Longmore, S. N., et al. 2019, MNRAS,
    484, 5734
Kulesa, C. A. 2003, in Chemistry as a Diagnostic of Star Formation, ed.
    C. L. Curry & M. Fich (Ottawa: NRC Research Press)
Landau, L. D., & Lifshitz, E. M. 1977, Quantum Mechanics (Non-relativistic
    Theory) (3rd ed.; New York: Pergamon)
Lang, C. C., Goss, W., & Morris, M. 2002, AJ, 124, 2677
Langer, W. D., Goldsmith, P. F., Pineda, J. L., et al. 2015, A&A, 576, A1
LaRosa, T. N., Brogan, C. L., Shore, S. N., et al. 2005, ApJL, 626, L23
LaRosa, T. N., Kassim, N. E., Lazio, T. J. W., & Hyman, S. D. 2000, AJ,
    119, 207
Last, I., Gilbert, M., & Baer, M. 1997, JChPh, 107, 1451
Launhardt, R., Zylka, R., & Mezger, P. G. 2002, A&A, 384, 112
Lazio, T. J. W., & Cordes, J. M. 1998, ApJ, 505, 715
Le Petit, F., Nehmé, C., Le Bourlot, J., & Roueff, E. 2006, ApJS, 164, 506
Le Petit, F., Ruaud, M., Bron, E., et al. 2016, A&A, 585, A105
Lee, C. W. 1996, ApJS, 105, 129
Liermann, A., Hamann, W.-R., Oskinova, L. M., Todt, H., & Butler, K. 2010,
    A&A, 524, A82
Lindsay, C. M., & McCall, B. J. 2001, JMoSp, 210, 60
Lis, D. C., Schilke, P., Bergin, E. A., et al. 2014, ApJ, 785, 135
Lis, D. C., Serabyn, E., Zylka, R., & Li, Y. 2001, ApJ, 550, 761
Liszt, H. 1992, ApJS, 82, 495
Liszt, H., & Lucas, R. 1995, A&A, 299, 847
Liszt, H., Lucas, R., & Pety, J. 2006, A&A, 448, 253
Liszt, H. S., & Burton, W. B. 1978, ApJ, 226, 790
Liu, D.-J., & Oka, T. 1985, PhRvL, 54, 1787
Low, F. J., Kleinmann, D. E., Forbes, F. F., & Aumann, H. H. 1969, ApJL,
    157, L97
Magnani, L., Zelenik, S., Dame, T. M., & Engebreth, B. 2006, AJ, 636, 267
Martin, C. L., Walsh, W. M., Xiao, K., et al. 2004, ApJS, 150, 239
Martin, D. W., McDaniel, E. W., & Meeks, M. L. 1961, ApJ, 134, 1013
Mauersberger, R., Henkel, C., Wilson, T. L., & Walmsley, C. M. 1986, A&A,
    162, 199
McCall, B. J., Geballe, T. R., Hinkle, K. H., & Oka, T. 1998a, Sci, 279, 1910
McCall, B. J., Geballe, T. R., Hinkle, K. H., & Oka, T. 1999, ApJ, 522, 338
McCall, B. J., Hinkle, K. H., Geballe, T. R., & Oka, T. 1998b, FaDi, 109, 267
McCall, B. J., Hinkle, K. H., Geballe, T. R., et al. 2002, ApJ, 567, 391
McCall, B. J., Huneycutt, A. J., Saykally, R. J., et al. 2003, Natur, 422, 500
McCall, B. J., Huneycutt, A. J., Saykally, R. J., et al. 2004, PhRvA, 70, 052716
McGee, R. X. 1970, AuJPh, 23, 541
Menon, T. K., & Ciotti, J. E. 1970, Natur, 227, 579
Menzel, D. H. 1937, ApJ, 85, 330
Miller, S., Achilleos, N., Ballester, G. E., et al. 2000, RSPTA, 358, 2485
Miller, S., Stallard, T., Melin, H., & Tennyson, J. 2010, FaDi, 147, 283
Miller, S., Stallard, T., Tennyson, T., & Melin, H. 2013, JPCA, 117, 9770
Mills, E. A. C., Ginsburg, A., Immer, K., et al. 2018, ApJ, 868, 7
Mills, E. A. C., & Morris, M. R. 2013, A&A, 772, 105
Molinari, S., Bally, J., Noriega-Crespo, A., et al. 2011, ApJL, 735, L33
Morris, M. 2006, J. Phys. Conf. Ser., 54, 1
Morris, M., Polish, N., Zuckerman, B., & Kaifu, N. 1983, ApJ, 88, 1228
Morris, M., & Serabyn, E. 1996, ARA&A, 34, 645
Morris, M., & Yusef-Zadeh, F. 1989, ApJ, 343, 703
Moultaka, J., Eckart, A., Tikare, K., & Bajat, A. 2019, A&A, 626, A44
Muenter, J. S. 1975, JMoSp, 55, 490
Muno, M. P., Baganoff, F. K., Bautz, M. W., et al. 2003, ApJ, 589, 225
Muno, M. P., Baganoff, F. K., Bautz, M. W., et al. 2004, ApJ, 613, 326
Nagata, T., Hyland, A. R., Straw, S. M., Sato, S., & Kawara, K. 1993, ApJ,
    406, 501
Nagata, T., Woodword, C. E., Shure, M., Pipher, J. L., & Okuda, H. 1990, ApJ,
    351, 83
Nagayama, T., Omodaka, T., Handa, T., et al. 2007, PASJ, 59, 869
Neale, L., Miller, S., & Tennyson, J. 1996, ApJ, 464, 516
Nobukawa, M., Uchiyama, H., Nobukawa, K. K., Yamauchi, S., &
    Koyama, K. 2016, ApJ, 833, 268
O'Connor, A. P., Urbain, X., Stützel, J., et al. 2015, ApJS, 219, 6
Odenwald, S. F., & Favio, G. G. 1984, ApJ, 283, 601
Oka, T. 1968, JChPh, 49, 3135
Oka, T. 1973, AdAMP, 9, 127
Oka, T. 1980, PhRvL, 45, 531
Oka, T. 1981, RSPTA, 303, 543
Oka, T. 2004, JMoSp, 228, 635

30

Oka, T. 2013, ChRv, 113, 8738
Oka, T. 2019, RSPTA, 377, 20180402
Oka, T., & Epp, E. 2004, ApJ, 613, 349
Oka, T., Geballe, T. R., Goto, M., Usuda, T., & McCall, B. J. 2005, ApJ,
    632, 882
Oka, T., Hasegawa, T., Hayashi, M., Handa, T., & Sakamoto, S. 1998a, ApJ,
    493, 730
Oka, T., Hasegawa, T., Sato, F., Tsuboi, M., & Miyazaki, A. 1998b, ApJS,
    118, 455
Oka, T., Shimizu, F. O., Shimizu, T., & Watson, J. K. G. 1971, ApJL, 165, L15
Okuda, H., Shibai, H., Nakagawa, T., et al. 1990, ApJ, 351, 89
Oort, J. H. 1977, ARA&A, 15, 295
Pak, S, Jaffe, D. T., & Keller, L. D. 1996, ApJL, 457, L43
Pan, F.-S., & Oka, T. 1986, ApJ, 305, 518
Papadopoulos, P. P. 2010, ApJ, 720, 226
Park, K., & Light, J. C. 2007a, JChPh, 126, 044305
Park, K., & Light, J. C. 2007b, JChPh, 127, 224101
Pavlinsky, M. N., Grebenev, S. A., & Sunyaev, R. A. 1992, SvAL, 18, 116
Penzias, A. A., Jefferts, K. B., & Wilson, R. W. 1971, ApJ, 165, 229
Petrignani, A., Altevogt, S., Berg, M. H., et al. 2011, PhRvA, 83, 032711
Piddington, J. H., & Minnett, H. C. 1951, AuSRA, 4, 459
Predehl, P., & Schmitt, J. H. M. M. 1995, A&A, 293, 889
Quack, M. 1977, MolPh, 34, 477
Rachford, B. L., Snow, T. P., Tumlinson, J., et al. 2002, ApJ, 577, 221
Ramírez, S. V., Arendt, R. G., Sellgren, K., et al. 2008, ApJS, 175, 147
Reber, G. 1944, ApJ, 100, 279
Requena-Torres, M. A., Martín-Pintado, J., Rodriquez-Franco, A., et al. 2006,
    A&A, 455, 971
Requena-Torres, M. A., Martín-Pitado, J., Martín, S., & Morris, M. R. 2008,
    ApJ, 672, 352
Revnivtsev, M., Sazanov, S., Churazov, E., et al. 2009, Natur, 458, 1142
Revnivtsev, M., Sazanov, S., Gilfanov, M., Churazov, E., & Sunyaev, R. 2006,
    A&A, 452, 169
Ridgway, S. T., Carbon, D. F., Hall, D. N. B., & Jewell, J. 1984, ApJS, 54, 177
Rieke, G. H., & Lebofsky, M. J. 1985, ApJ, 288, 618
Riquelme, D., Bronfman, L., Mauersberger, R., May, J., & Wilson, T. L. 2010,
    A&A, 523, A45
Robinson, B. J., & McGee 1970, AuJPh, 23, 405
Rodríguez-Fernández, N. J., Martín-Pintado, J., Fuente, A., et al. 2001, A&A,
    365, 174
Rolleston, W. R. J., Smartt, S. J., Dufton, P. L., & Ryans, R. S. I. 2000, A&A,
    363, 537
Rougoor, G. W., & Oort, J. H. 1960, PNAS, 46, 1
Rudd, M. E., Kim, Y.-K., Madison, D. H., & Gallagher, J. W. 1985, RvMP,
    57, 965
Rudolph, A. L., Simpson, J. P., Haas, R. M., Erickson, E. M., & Fitch, M.
    1997, ApJ, 489, 94
Sawada, T., Hasegawa, T., Handa, T., et al. 2001, ApJS, 136, 189
Schilke, P., Neufeld, D. A., Müller, H. S. P., et al. 2014, A&A, 566, A29
Schneider, R. R. N., Izzard, R. G., de Mink, S. E., et al. 2014, ApJ, 780, 117
Schultheis, M., Sellgren, K., Ramírez, S., et al. 2009, A&A, 5, 157
Scoville, N. Z. 1972, ApJL, 175, L127
Scoville, N. Z., Solomon, P. M., & Thaddeus, P. 1972, ApJ, 172, 335
Seaton, M. J. 1959, MNRAS, 119, 81
Simpson, J. P., Colgan, S. W. J., Rubin, R. H., Erickson, R. F., & Haas, M. R.
    1995, ApJ, 444, 721
Skrutskie, M. F., Cutri, R. M., Stiening, R., et al. 2006, AJ, 131, 1163
Smith, J. A., Hamzeloui, S., Fink, D. J., & Myers, E. G. 2018, PhRvL, 120,
    143002
Snow, T. P., & McCall, B. J. 2006, ARA&A, 44, 367
Sodroski, T. J., Odegard, N., Dwek, E., et al. 1995, ApJ, 452, 262
Sofia, U. J., Lauroesch, J. T., Meyer, D. M., & Cartledge, S. I. B. 2004, ApJ,
    605, 272
Sofue, Y. 1995, PASJ, 47, 527
Sofue, Y. 2006, PASJ, 58, 335
Sofue, Y., Reich, W., Inoue, M., & Seiradakis, J. H. 1987, PASJ, 39, 95
Sonnentrucker, P., Neufeld, D. A., Gerin, M., et al. 2013, ApJL, 763, L19
Sormani, M. C., Treß, R. G., Ridley, M., et al. 2018, MNRAS, 475, 2383
Spitzer, L., Jr. 1948, ApJ, 107, 6
Spitzer, L., Jr., & Tomasko, M. G. 1968, ApJ, 152, 972
Sunyaev, R. A., Markevitch, M., & Pavlinsky, M. 1993, ApJ, 407, 606
Thomson, J. J. 1911, PMag, 21, 225
Townes, C. H., & Schawlow, A. L. 1955, Microwave Spectroscopy (New
    York: McGraw-Hill)
Tsuboi, M, Handa, T., & Ukita, N. 1999, ApJS, 120, 1
Uchida, Y., Shibata, K., & Sofue, Y. 1985, Natur, 317, 699
Uy, D., Cordonnier, M., & Oka, T. 1997, PhRvL, 78, 3844
Vallée, J. P. 2014, MNRAS, 442, 2998
Vallée, J. P. 2016, AJ, 151, 55
Viehmann, T., Eckart, A., Schödel, R., et al. 2005, A&A, 433, 117
Wang, Q. D., Gotthelf, E. V., & Lang, C. C. 2002, Natur, 415, 148
Warwick, R. S. 2014, MNRAS, 445, 66
Warwick, R. S., Byckling, K., & Pérez-Ramírez, D. 2014, MNRAS, 438, 2967
Watson, W. D. 1973, ApJL, 183, L17
Webber, W. R. 1998, ApJ, 506, 329
Whiteoak, J. B., & Gardener, F. F. 1979, MNRAS, 188, 445
Whittet, D. C. B., Boogert, A. C. A., Gerakines, P. A., et al. 1997, ApJ,
    490, 729
Wilson, T. L., Henkel1, C., & Hüttemeister, S. 2006, A&A, 460, 533
Yamauchi, S., Nobukawa, K. K., Nobukawa, M., Uchiyama, H., &
    Koyama, K. 2016, PASJ, 68, 59
Yoast-Hull, T. M., Gallagher, J. S., III, & Zweibel, E. G. 2016, MNRAS,
    457, L29
Yusef-Zadeh, F., Hewitt, J. W., Wardle, M., et al. 2013, ApJ, 762, 33
Yusef-Zadeh, F., & Morris, M. 1987, AJ, 94, 1178
Yusef-Zadeh, F., Morris, M., & Chance, D. 1984, Natur, 310, 557
Yusef-Zadeh, F., Muno, M., Wardle, M., & Lis, D. C. 2007, ApJ, 656, 847
Zeng, S., Jiménez-Serra, I., Rivilla, V. M., et al. 2018, MNRAS, 478, 2962
Zou, Q., & Varanasi, P. 2002, JQSRT, 75, 63
Zylka, R., Güsten, R., Henkel, C., & Batrla, W. 1992, A&AS, 96, 525